

doc. numbers:  
DESY, FERMILAB, IFIC, IRFU  
JLAB, KEK, PNNL, SLAC,  
and more ...

March 8, 2021

# **The International Linear Collider: Report to Snowmass 2022**

THE ILC INTERNATIONAL DEVELOPMENT TEAM AND THE ILC COMMUNITY

## ABSTRACT

The International Linear Collider (ILC) is on the table now as a new global energy-frontier accelerator laboratory taking data in the 2030's. The ILC addresses key questions for our current understanding of particle physics. It is based on a proven accelerator technology. Its experiments will challenge the Standard Model of particle physics and will provide a new window to look beyond it. This document brings the story of the ILC up to date, emphasizing its strong physics motivation, its readiness for construction, and the opportunity it presents to the US and the global particle physics community.



# Contents

<b>1</b>	<b>Introduction</b>	<b>9</b>
1.1	Context for the ILC . . . . .	9
1.2	Outline . . . . .	11
<b>2</b>	<b>Outline of the ILC Physics Case</b>	<b>13</b>
<b>3</b>	<b>Route to the ILC</b>	<b>17</b>
3.1	International Design Team . . . . .	17
3.2	ILC Pre-Lab . . . . .	17
3.3	ILC Laboratory . . . . .	17
3.4	Timeline for ILC Detectors . . . . .	17
<b>4</b>	<b>ILC Accelerator</b>	<b>19</b>
4.1	ILC Accelerator Design . . . . .	19
4.1.1	Design evolution since the TDR . . . . .	22
4.1.2	Superconducting RF Technology . . . . .	23
4.1.3	Accelerator design . . . . .	36
4.1.4	Upgrade options . . . . .	48
4.1.5	Civil engineering and site . . . . .	50
4.1.6	Cost and schedule . . . . .	50
4.2	ILC Staging up to 1 TeV . . . . .	54
4.3	ILC Scope Beyond 1 TeV . . . . .	54
4.3.1	Gradient status for the ILC baseline 250 GeV . . . . .	54

4.3.2	High Gradient (45 MV/m) SRF for Upgrade Paths to 1 TeV . . . . .	57
4.3.3	Toward 60 MV/m - Advanced Shape Cavities . . . . .	57
4.3.4	Nb <sub>3</sub> Sn . . . . .	61
4.4	Issues for ILC Accelerator R&D . . . . .	64
4.5	Opportunities for US contributions . . . . .	64
4.5.1	Superconducting Linac . . . . .	64
4.5.2	Electron and Positron Sources . . . . .	66
4.5.3	Damping Ring, Beam Delivery System, and Beam Dump . . . . .	66
4.5.4	Summary . . . . .	67
<b>5</b>	<b>General Aspects of the ILC Physics Environment</b>	<b>69</b>
5.1	Key Standard Model Processes . . . . .	69
5.2	Energy and Luminosity . . . . .	69
5.3	Beam Polarization . . . . .	69
<b>6</b>	<b>ILC Detectors</b>	<b>71</b>
6.1	Detector Requirements for the Physics Program . . . . .	71
6.2	The ILD Detector . . . . .	71
6.2.1	Detector description and capabilities . . . . .	71
6.2.2	R&D issues for the ILD design . . . . .	71
6.3	The SiD Detector . . . . .	71
6.3.1	Detector description and capabilities . . . . .	71
6.3.2	R&D issues for the SiD design . . . . .	79
6.4	New Technologies for ILC Detectors . . . . .	79
6.4.1	Tracking . . . . .	80
6.4.2	Calorimetry . . . . .	80
6.4.3	Vertex Detector . . . . .	80
6.4.4	Forward Detectors . . . . .	80
6.4.5	Muon System . . . . .	80
6.4.6	Timing Elements . . . . .	80



<i>CONTENTS</i>	5
<b>7 ILC Detector Simulation</b>	<b>81</b>
7.1 ILC Fast Simulation Frameworks . . . . .	81
7.2 ILCSOFT Framework . . . . .	81
7.3 ILC SM Background Samples . . . . .	81
<b>8 ILC Physics Measurements at 250 GeV</b>	<b>83</b>
8.1 Higgs – Conventional Decays . . . . .	83
8.1.1 Hadronic decays . . . . .	83
8.1.2 Leptonic decays . . . . .	83
8.1.3 EW-bosonic decays . . . . .	83
8.2 Higgs – Exotic Decays . . . . .	84
8.3 $W$ Boson . . . . .	84
8.4 4-Fermion Processes . . . . .	84
8.5 Precision QCD . . . . .	85
8.6 Dark Sector . . . . .	85
<b>9 ILC Precision Electroweak Measurements</b>	<b>87</b>
9.1 Radiative Return to the $Z$ . . . . .	87
9.2 $Z$ Pole Program . . . . .	87
9.3 $W$ and $Z$ Boson Masses . . . . .	87
<b>10 ILC Physics Measurements at 350, 500, and 1000 GeV</b>	<b>89</b>
10.1 Top Quark . . . . .	89
10.1.1 Top Quark Mass . . . . .	89
10.1.2 Current state of the art and (HL-) LHC prospects . . . . .	90
10.1.3 Top Quark Electroweak Couplings . . . . .	90
10.2 Higgs . . . . .	90
10.2.1 $WW$ fusion . . . . .	90
10.2.2 Higgs Self-Coupling . . . . .	90
10.2.3 Top Quark Yukawa Coupling . . . . .	90

10.3	<i>W</i> Boson . . . . .	91
10.4	4-Fermion Processes . . . . .	91
10.5	New Particle Searches – TeV Scale . . . . .	91
10.6	New Particle Searches – Dark Sector . . . . .	91
<b>11</b>	<b>ILC Fixed-Target Program</b>	<b>93</b>
11.1	ILC Facilities for Fixed-Target Experiments . . . . .	93
11.2	Beam-Dump Experiments . . . . .	94
11.3	Dedicated Secondary-Beam Experiments . . . . .	94
11.4	Nuclear and Hadron Physics with Electron and Positron Beams . . . . .	94
11.5	ILC as an Accelerator Test-Bed . . . . .	94
<b>12</b>	<b>Precision Tests of the Standard Model</b>	<b>95</b>
12.1	Precision Standard Model Theory for ILC . . . . .	95
12.2	Frameworks for Effective Field Theory . . . . .	96
12.3	Expectations from a Unified SMEFT Analysis . . . . .	96
12.4	Expectations for CP-Violating Operators . . . . .	96
12.5	Expectations for Heavy-Quark Operators . . . . .	96
<b>13</b>	<b>Big Physics Questions Addressed by ILC</b>	<b>97</b>
13.1	Can the Standard Model be exact to very high energies? . . . . .	98
13.2	Why is there more matter than antimatter? . . . . .	98
13.3	What is the dark matter of the universe? . . . . .	99
13.4	What is the energy scale of new physics? . . . . .	99
13.5	Why is electroweak symmetry broken? . . . . .	100
<b>14</b>	<b>ILC Probes of the Big Questions</b>	<b>103</b>
14.1	Higgs boson: tests for violation of the Standard Model . . . . .	103
14.2	Higgs boson: the Higgs Inverse Problem . . . . .	103
14.3	Electroweak sector . . . . .	103
14.4	Top Quark . . . . .	103

<b>15 Long-Term Future of the ILC Laboratory</b>	<b>105</b>
15.1 Future Accelerators in the ILC Tunnel . . . . .	105
15.1.1 Very High Gradient Superconducting RF . . . . .	105
15.1.2 Very High Gradient Copper Accelerators . . . . .	105
15.1.3 Plasma, Laser, and Structure Wakefield Accelerators . . . . .	105
15.2 Physics Opportunities at Multi-TeV . . . . .	107
15.3 Physics Opportunities at Multi-10 TeV . . . . .	107
<b>16 Conclusions</b>	<b>109</b>



# Chapter 1

## Introduction

[ 3 pages; corresponding editor: Hitoshi Murayama (hitoshi@berkeley.edu)]

The ILC is a proposed next-generation  $e^+e^-$  collider. It starts with  $\sqrt{s} = 250$  GeV as the Higgs factory, which provides typically an order of magnitude improvement in precision Higgs measurements beyond the HL-LHC. Such precision measurements will provide guidance to the next energy scale for future facilities. At the same time, it provides numerous searches for new physics with monophoton or invisible and exotic Higgs decays, for example into a light dark sector. It can host ancillary experiments with beam dump and/or near IP detectors to search for long-lived and invisible particles. It is technologically mature with a well-understood cost that is about the same as the LHC. The linear design allows for extensions to upgrade energies. The next steps would likely be the  $t\bar{t}$  threshold and open  $t\bar{t}$  as well as  $t\bar{t}H$  production at 500–550 GeV. The site was specifically chosen to allow for an upgrade up to 1 TeV with the same technology, for the Higgs self-coupling measurement and many new physics searches. Superconducting RF cavity technology has an ample room for improvements, allowing for even a 3–4 TeV collider in the same tunnel. Future technologies such as plasma wakefield or dielectric laser accelerators may go into the tens of TeV energy range.

Below we describe the context for the ILC as it has evolved over half a century of development in particle physics.

### 1.1 Context for the ILC

The ILC stands at the end of a long history. The need for a linear collider was recognized already in 1960's given the energy loss due to unavoidable synchrotron radiation from beams in circular colliders. To achieve power-efficient acceleration, the development of superconducting radio frequency (SCRF) cavities started in earnest in the 1980's. Over four decades, intensive research and development achieved much higher acceleration gradients and reduced the costs of SCRF by more than an order of magnitude. SCRF provides better tolerances compared to room-temperature klystron-based designs, and was chosen as the ILC technology in 2005 by the International Tech-

nology Recommendation Panel chaired by Barry Barish (2017 Nobel Laureate in Physics). The International Committee for Future Accelerators, a body created by the International Union of Pure and Applied Physics in 1976 to facilitate international collaboration in the construction and use of accelerators for high energy physics, recommended the launch of the Global Design Effort (GDE) to produce a Technical Design Report (TDR) for the ILC as an international project. The GDE successfully produced the TDR in 2013 with a purposely site-independent design [1, 2, 3, 4, 5].

There is also a long history of discussions on the scientific merit for the ILC. The energy scale of the weak interaction, which makes the Sun burn and allows the synthesis of the chemical elements, was pointed out to be around 250 GeV in 1933 by Enrico Fermi. The need to reach this energy scale has been obvious since then, though the precise target energy was not clear. Early discussions for linear colliders called for 1000 GeV as a safe choice for guaranteed science output. The GDE focused on 500 GeV for the study of the Higgs boson based on the precision electroweak data of early 2000's. It was only in 2012 that the Higgs boson was discovered at the Large Hadron Collider (LHC) at CERN. This provided a clear target energy for the ILC at 250 GeV. In the same year, the Japanese Association of High-Energy Physicists (JAHEP) issued a report expressing interest in hosting the ILC in Japan with 250 GeV center-of-momentum energy as its first phase. The European Strategy for Particle Physics updated in 2013 highlighted “*the ILC, based on superconducting technology, will provide a unique scientific opportunity at the precision frontier.*” This was followed by the report of the US Prioritization Panel for Particle Physics Projects (P5) that listed “*Use the Higgs boson as a new tool for discovery*” as the first among the science drivers for particle physics and stated “*As the physics case is extremely strong, all (funding) Scenarios include ILC support*”.

Intense discussions ensued worldwide how to realize the ILC. Japanese government instituted a multitude of committees looking into the scientific and societal merit of hosting the ILC in Japan as well as its technological feasibility and costs. The US government encouraged Japan to host the ILC, with letters from the Secretary of Energy and the Deputy Secretary of State to Japanese Ministers. The 2020 update of the European Strategy for Particle Physics stated “*An electron-positron Higgs factory is the highest-priority next collider*” and added “*The timely realisation of the electron-positron International Linear Collider (ILC) in Japan would be compatible with this strategy and, in that case, the European particle physics community would wish to collaborate.*” Following this update, ICFA created the International Development Team (IDT) in August 2020 to prepare for the creation of prelab towards the realization of the ILC. The IDT is hosted by KEK, the national laboratory for high-energy accelerators in Japan.

Since its launch, IDT has collected information, worked with ICFA, interacted with the community, consulted the funding agencies, to formulate what is required of the ILC Pre-Lab. The Pre-Lab is envisioned to be a four-year process, finalizing the Engineering Design Report for the ILC in a site-specific fashion for the Kitakami mountain range in northern Japan, forging agreements among international partners, and recommending specific experiments for the ILC.

## 1.2 Outline

This report will update the documents prepared by ILC for the European Strategy for Particle Physics. These include a comprehensive review of the ILC up to 2019 [6] and a review of the ILC capabilities for precision measurement [7]. A comprehensive bibliography for the ILC, up to mid-2020, can be found in [8].

The outline of this report is the following: Chapter 2 will present the most important points of the physics case for the ILC. In Chapter 3, we will present the current plan and timeline for the realization of the ILC in Japan.

Chapter 4 will present the current state of the ILC accelerator design, including details of the various ILC energy stages up to a CM energy of 1 TeV. This chapter will also discuss the prospects for extension of the ILC to even higher energies and other issues for ILC accelerator R&D. It will conclude with a discussion of the opportunities and tentative plans for US contributions to the ILC accelerator.

Chapter 5 will review the basic aspects of the physics environment of the ILC—the major physics processes, the plan for stage-by-stage improvement in the energy and luminosity, and the key role played in the experimental program by electron and positron beam polarization.

Chapter 6 will describe the ILC detectors. We will begin with descriptions of the two current proposed detectors ILD and SiD, including the expected measurement capabilities and issues for which further R&D is needed. The chapter will conclude with a survey of new technologies that offer the promise of further improvements in the detector capabilities. Chapter 7 will describe the simulation framework used in studying the detector capabilities and projecting the measurement accuracy of physical observables.

Chapter 8 will describe the planned physics measurements at a CM energy of 250 GeV. These include measurements on the Higgs boson and the  $W$  boson, measurements of 2-fermion production, the ILC program in precision QCD, and descriptions of a number of relevant new particle searches.

Chapter 9 will describe the ILC program in precision electroweak measurements. This includes improvements of the precision electroweak parameters of the  $Z$  boson, both at 250 GeV through the radiative return reaction  $e^+e^- \rightarrow \gamma Z$  and through a dedicated program of running at the  $Z$  resonance. It also includes high-precision measurements of the  $W$  boson mass and width and improved measurements of these properties for the  $Z$  boson.

Chapter 10 will describe the planned physics measurements at CM energies of 350 GeV and above, up to 1 TeV. The topics here include the ILC program of precision measurements of the top quark, the completion of the measurement of the Higgs boson profile, including the measurements of the Higgs self-coupling and the top quark Yukawa coupling, and the ultimate capabilities of the ILC in triple gauge boson couplings and new particle searches.

Chapter 11 will describe the fixed-target program that the intense, high-energy electron and positron beams of the ILC will make available.

Chapters 12-14 will address the interpretation of the ILC measurements. Chapter 12 will begin

with a review of the status of precision SM theory for ILC processes. It will then discuss the network of tests of the SM available at the ILC. This chapter will present a unified description of these tests using Standard Model Effective Field Theory (SMEFT), reviewing the conceptual basis of this approach and demonstrating its power in providing a unified interpretation of the full set of ILC experimental measurements. Chapter 13 will present a theoretical context for the expectation that the ILC will discover deviations from the SM predictions and the relation of such deviations to the most important question now being asked in particle physics. Chapter 14 will bring these two lines of analysis together, quantifying the ability of the ILC to overturn the SM and to provide evidence of the more correct underlying model for particle physics.

Finally, Chapter 15 will lay out some possible futures for the ILC laboratory with accelerators at still higher energies offering multi-TeV and multi-10-TeV electron, positron, and photon collisions.



## Chapter 2

# Outline of the ILC Physics Case

[4 pages; corresponding editor: Michael Peskin (mpeskin@slac.stanford.edu)]

The physics motivation for constructing the ILC is very strong. The flagship program of the ILC is the study of the Higgs boson at a much higher level of precision than has been possible at the LHC. The ILC will also carry out precision measurements of the other heavy and still-mysterious particle in the Standard Model, the top quark. It will carry out a program of specific searches for postulated new particles in regions that are very difficult for the LHC to access. Beyond these specific targets, the ILC will greatly improve the level of our understanding of the full set of electroweak processes in the region up to its final CM energy. In the context of Standard Model Effective Field Theory (SMEFT), these measurements will work together to strongly challenge the Standard Model. In this chapter, we will introduce each of these points and prepare the ground for a more detailed discussion later in this report.

We begin with the 125 GeV Higgs boson. This particle is the centerpiece of the SM, yet still we know little about it. From the LHC experiments, we now know that the couplings of the Higgs boson agree with those predicted in the SM, at the level of 20% accuracy for the major decay modes. However, this is not nearly sufficient to distinguish the minimal SM description of the Higgs boson from those of competing models. According to SMEFT, the deviations of Higgs couplings from SM predictions are parametrically of the order of  $m_h^2/M^2$ , where  $M$  is the mass scale of additional new particles. Given the constraints from particle searches at the LHC, these deviations are expected to be at most of order 5-10%, and, to claim discovery of new physics, the deviations must be measured with high significance. This calls for a dedicated program to measure the full suite of couplings of the Higgs boson, and to push the precision of those measurements to the 1% level and below. This requires an  $e^+e^-$  collider such as the ILC.

The ILC is well-positioned to carry out this program of measuring the complete profile of the Higgs boson couplings. At 250 GeV, the ILC accesses the reaction  $e^+e^- \rightarrow Zh$ , producing about half a million Higgs bosons, each tagged by a recoil  $Z$  boson at the lab energy of 110 GeV. Looking in the opposite hemisphere, we will measure all of the branching ratios of the Higgs boson down to values of order  $10^{-4}$ . These include 10 different modes of Higgs decay predicted in the SM, and also, possibly, invisible, partially-invisible, flavor changing, and other exotic modes of Higgs

decay. By counting recoil  $Z$  bosons, we will obtain an absolute measurement of the cross section for  $e^+e^- \rightarrow Zh$ , which can then be translated into absolute normalizations of the various partial widths.

At the second stage of the ILC at 500 GeV, the  $W$  fusion reaction  $e^+e^- \rightarrow \nu\bar{\nu}h$  opens up. This reaction offers an event sample of about 1 million Higgs boson events in which the only visible signals in the event are from Higgs decay. This will not only allow new measurements to complement the 250 GeV data but also improved characterization of such issues as  $h \rightarrow b\bar{b}/gg/c\bar{c}$  separation, angular distributions in  $h \rightarrow WW^*$ , and CP violation tests in  $h \rightarrow \tau^+\tau^-$ . The combination of the 250 and 500 GeV programs will give high confidence in any deviations from the SM detected in the Higgs boson data.

Running at 500 GeV and above also gives access to two important Higgs couplings that cannot be probed directly in Higgs decays, the Higgs coupling to  $t\bar{t}$  and the Higgs self-coupling. Our studies of the ILC capabilities at 1 TeV predict truly archival measurements of these quantities, with errors below 2% and 10%, respectively.

Different models of new physics beyond the SM affect the various Higgs couplings differently. Since the ILC program can determine each Higgs coupling of the large set available, individually and without ambiguity, it will provide a pattern of deviations from the predictions of the SM that can distinguish different hypotheses about the underlying model.

The ILC program of experimental measurements on the Higgs boson will be described in Chapter 8 and 10 of this report, and the interpretation of these measurements will be discussed in some detail in Chapters 12 and 14.

The 500 GeV ILC will also give an excellent setting for the measurement of the mass and properties of the top quark. The mass of the top quark will be determined from the position of the sharp threshold in  $e^+e^- \rightarrow t\bar{t}$ . The threshold shape is determined by the short-distance top quark mass, so that the mass defined in this way, which is needed for high-precision predictions in and beyond the SM, is determined from the data without ambiguity. At  $e^+e^-$  colliders, the electroweak form factors of the top quark, which contain crucial information about the role of the top quark in electroweak symmetry breaking, determine the primary top quark pair production cross section. Thus, very high precision measurements of these form factors are possible. The ILC program of measurements on the top quark will be discussed in Chapter 10 of this report.

Beyond these SM particles, the ILC has the potential to access new particles predicted in models beyond the SM. The LHC experiments have given powerful access to proposed new particles with couplings to QCD, but their capability to discover particles with only electroweak couplings is limited. All LHC searches come with footnotes concerning the sizes of electroweak cross sections, the expected decay patterns, the amount of missing energy, and other features. Searches at the ILC will allow these footnotes to be eliminated, giving access to systems with large missing energy and other challenging features, in particular, to supersymmetry partners of the Higgs boson and to dark matter in models with compressed spectra. These issues will be described in Sections 8 and 10 of this report.

The ILC will dramatically improve the precision of our understanding of electroweak reactions.

The reaction  $e^+e^- \rightarrow W^+W^-$ , with strong dependence on both initial- and final-state polarizations, will allow us to dissect the structure of the triple-gauge-boson coupling. The reactions  $e^+e^- \rightarrow f\bar{f}$  allow searches for additional electroweak resonances that access the 10-TeV mass range and are flavor- and helicity-specific. The study of radiative-return events ( $e^+e^- \rightarrow \gamma Z$ ) at 250 GeV will already improve our precision knowledge of  $Z$ -fermion couplings beyond that obtained at LEP. A dedicated ILC “Giga- $Z$ ” run at the  $Z$  resonance ( $5 \times 10^9 Z$ s) will improve the precision of most electroweak observables by more than an order of magnitude. These measurements and others are described in Chapters 8, 9, and 10.

The simplicity of hadronic final states in  $e^+e^-$  annihilation also allows not only higher precision tests of QCD but also new observables that give insight into features such as jet substructure that have come to light at the LHC. This new program of QCD measurements will be described in Chapter 8.

The ILC will also make available the most intense and highest-energy electron and positron beams for beam dump and dedicated fixed-target experiments targeting light weakly-interacting particles. This program will be described in Chapter 11.

These measurements are very powerful already when they are considered separately, but they take on increased power when they are combined to stress-test the SM in coherent way. This becomes particularly clear when the full set of SM tests is analyzed using SMEFT. In this approach, corrections to the SM are described by contributions to an effective Lagrangian from operators of dimension 6 and higher invariant under the well-tested SM gauge symmetries. There is only one Lagrangian; its higher-dimension operators generally contribute to many electroweak reactions and so receive an array of experimental constraints. We will describe this method in detail and give examples of its powerful use in Chapter 12.

There is one more important point that we should make concerning the program of measurements of the ILC. The goal of testing the SM is not simply to improve the error bars. It is widely appreciated that the Standard Model of particle physics (SM), though it is very successful in describing the results of experiments, is not adequate as a complete theory of elementary particles. Thus, the goal of the ILC experiments must be to *prove that the SM is incomplete*, and to show the path to a better understanding of nature.

One way to prove the inadequacy of the SM is to discover a new resonance that the SM does not account for. This was the primary goal of the LHC experiments. So far, no such resonance has appeared. There is still considerable room to discover a new resonance at the HL-LHC, but that window is closing. It is important to open a new, complementary window, and this is what the ILC’s capability for precision tests of the SM will make available.

It is not straightforward, though, to demonstrate a deviation from the SM through precision measurements. First, of all, the deviation must be observed with high statistical significance. Second, the possible systematic errors that could mimic the deviation must be under complete control. This calls for multiple cross-checks on the sources of error and, if possible, measurements with different sources of systematic errors that can be compared. Finally, the view provided by precision measurements cannot be one-dimensional; rather, it should be part of a collective program that has the power to show a pattern of discrepancies. In the best case, a pattern of well-established

deviations from the SM can point to a common origin and thus indicate the nature of the true underlying theory.

The experimental program of the ILC is well-equipped to address these points. The general simplicity and cleanliness of  $e^+e^-$  annihilation provides an excellent starting point in the quest for precision. This environment allows the construction of detectors with high segmentation and very low material budget, allowing collider event measurements of unprecedented quality. In the energy region of the ILC, electroweak cross sections have a large and well-understood dependence on beam polarization. With both electron and positron beam polarization, the ILC will provide four distinct event samples at each energy to use in understanding measurements and backgrounds. As we have noted above for the Higgs boson program, changes in the center of mass energy can also bring in new physics processes that access and cross-check the variables targetted in precision measurements. The enabling features of the ILC experimental environment will be discussed in Chapter 5. The capabilities of detectors for the ILC and strategies for further improvement will be discussed in Chapter 6. Throughout the succeeding chapters, you will see these elements at work to insure the high quality of the ILC measurements.

The ILC thus offers a new approach to the discovery of physics beyond the SM, one of great capability and robustness. These experiments must be carried out. They have the power to lead us to a new stage in our understanding of fundamental physics.

## Chapter 3

# Route to the ILC

[8 pages; corresponding editor: Tatsuya Nakada, Hitoshi Murayama (hitoshi@berkeley.edu)]

(The organization, schedule, and prospects for the ILC will be explained in this chapter. These will be clearer after the ILC Pre-Lab is set up, a development expected in 2022. The current state of the ILC organization was presented by Tatsuya Nakada and others in the Monday plenary session of the LCWS 2021 workshop, <https://indico.cern.ch/event/995633/> .)

### 3.1 International Design Team

### 3.2 ILC Pre-Lab

### 3.3 ILC Laboratory

### 3.4 Timeline for ILC Detectors



# Chapter 4

## ILC Accelerator

[general corresponding editor: Shinichiro Michizono (shinichiro.michizono@kek.jp)]

### 4.1 ILC Accelerator Design

[10 pages; corresponding editor: Benno List (benno.list@desy.de)]

FIRST VERSION: Verbatim Copy from European Strategy Document

The International Linear Collider (ILC) is a 250 GeV (extendable up to 1 TeV) linear  $e^+e^-$  collider, based on 1.3 GHz superconducting radio-frequency (SCRF) cavities. It is designed to achieve a luminosity of  $1.35 \cdot 10^{34} \text{ cm}^{-1}\text{s}^{-1}$  and provide an integrated luminosity of  $400 \text{ fb}^{-1}$  in the first four years of running. The electron beam will be polarised to 80 %, and positrons with 30 % polarization will be provided if the undulator based positron source concept is employed.

Its parameters have been set by physics requirements first outlined in 2003, updated in 2006, and thoroughly discussed over many years with the physics user community. After the discovery of the Higgs boson it was decided that an initial energy of 250 GeV provides the opportunity for a precision Standard Model and Higgs physics programme at a reduced initial cost [9]. Some relevant parameters are given in Tab. 4.1. This design evolved from two decades of R&D, described in Sec. 1, an international effort coordinated first by the GDE under ICFA mandate and since 2013 by the LCC.

The fundamental goal of the design of the ILC accelerator is a high energy-efficiency. The ILC design limits the overall power consumption of the accelerator complex during operation to 129 MW at 250 GeV and 300 MW at 1 TeV, which is comparable to the power consumption of CERN. This is achieved by the use of SCRF technology for the main accelerator, which offers a high RF-to-beam efficiency through the use of superconducting cavities, operating at 1.3 GHz, where high-efficiency klystrons are commercially available. At accelerating gradients of 31.5 to 35 MV/m this technology offers high overall efficiency and reasonable investment costs, even considering the cryogenic infrastructure needed for the operation at 2 K.

Quantity	Symbol	Unit	Initial	$\mathcal{L}$ Upgrade	TDR	Up
Centre of mass energy	$\sqrt{s}$	GeV	250	250	250	500
Luminosity	$\mathcal{L}$	$10^{34}\text{cm}^{-2}\text{s}^{-1}$	1.35	2.7	0.82	1.8/3.6
Polarisation for $e^- (e^+)$	$P_- (P_+)$		80 % (30 %)	80 % (30 %)	80 % (30 %)	80 % (30 %)
Repetition frequency	$f_{\text{rep}}$	Hz	5	5	5	5
Bunches per pulse	$n_{\text{bunch}}$	1	1312	2625	1312	1312/2625
Bunch population	$N_e$	$10^{10}$	2	2	2	2
Linac bunch interval	$\Delta t_b$	ns	554	366	554	554/366
Beam current in pulse	$I_{\text{pulse}}$	mA	5.8	5.8	8.8	5.8
Beam pulse duration	$t_{\text{pulse}}$	$\mu\text{s}$	727	961	727	727/961
Average beam power	$P_{\text{ave}}$	MW	5.3	10.5	10.5	10.5/21
Norm. hor. emitt. at IP	$\gamma\epsilon_x$	$\mu\text{m}$	5	5	10	10
Norm. vert. emitt. at IP	$\gamma\epsilon_y$	nm	35	35	35	35
RMS hor. beam size at IP	$\sigma_x^*$	nm	516	516	729	474
RMS vert. beam size at IP	$\sigma_y^*$	nm	7.7	7.7	7.7	5.9
Luminosity in top 1 %	$\mathcal{L}_{0.01}/\mathcal{L}$		73 %	73 %	87.1 %	58.3 %
Energy loss from beamstrahlung	$\delta_{\text{BS}}$		2.6 %	2.6 %	0.97 %	4.5 %
Site AC power	$P_{\text{site}}$	MW	129		122	163
Site length	$L_{\text{site}}$	km	20.5	20.5	31	31

Table 4.1: Summary table of the ILC accelerator parameters in the initial 250 GeV staged configuration (with TDR parameters at 250 GeV given for comparison) and possible upgrades. A 500 GeV machine could also be operated at 250 GeV with 10 Hz repetition rate, bringing the maximum luminosity to  $5.4 \cdot 10^{34} \text{cm}^{-2}\text{s}^{-1}$  [10].



The underlying TESLA technology is mature, with a broad industrial base throughout the world, and is in use at a number of free electron laser facilities that are in operation (E-XFEL at DESY, Hamburg), under construction (LCLS-II at SLAC, Stanford) or in preparation (SCLF in Shanghai) in the three regions Asia, Americas, and Europe that contribute to the ILC project. In preparation for the ILC, Japan and the U.S. have founded a collaboration for further cost optimisation of the TESLA technology. In recent years, new surface treatment technologies utilising nitrogen during the cavity preparation process, such as the so-called nitrogen infusion technique, have been developed at Fermilab, with the prospect of achieving higher gradients and lower loss rates with a less expensive surface preparation scheme than assumed in the TDR (see Sec. 4.1.2).

When the Higgs boson was discovered in 2012, the Japan Association of High Energy Physicists (JAHEP) made a proposal to host the ILC in Japan [11, 12]. Subsequently, the Japanese ILC Strategy Council conducted a survey of possible sites for the ILC in Japan, looking for suitable geological conditions for a tunnel up to 50 km in length (as required for a 1 TeV machine), and the possibility to establish a laboratory where several thousand international scientists can work and live. As a result, the candidate site in the Kitakami region in northern Japan, close to the larger cities of Sendai and Morioka, was found to be the best option. The site offers a large, uniform granite formation with no currently active faults and a geology that is well suited for tunnelling. Even in the great Tohoku earthquake in 2011, underground installations in this rock formation were essentially unaffected [13], which underlines the suitability of this candidate site.

This section starts with a short overview over the changes of the ILC design between the publication of the TDR in 2013 and today, followed by a description of the SCRF technology, and an description of the overall accelerator design and its subsystems. Thereafter, possible upgrade options are laid out, the Japanese candidate site in the Kitakami region is presented, and costs and schedule of the accelerator construction project are shown.

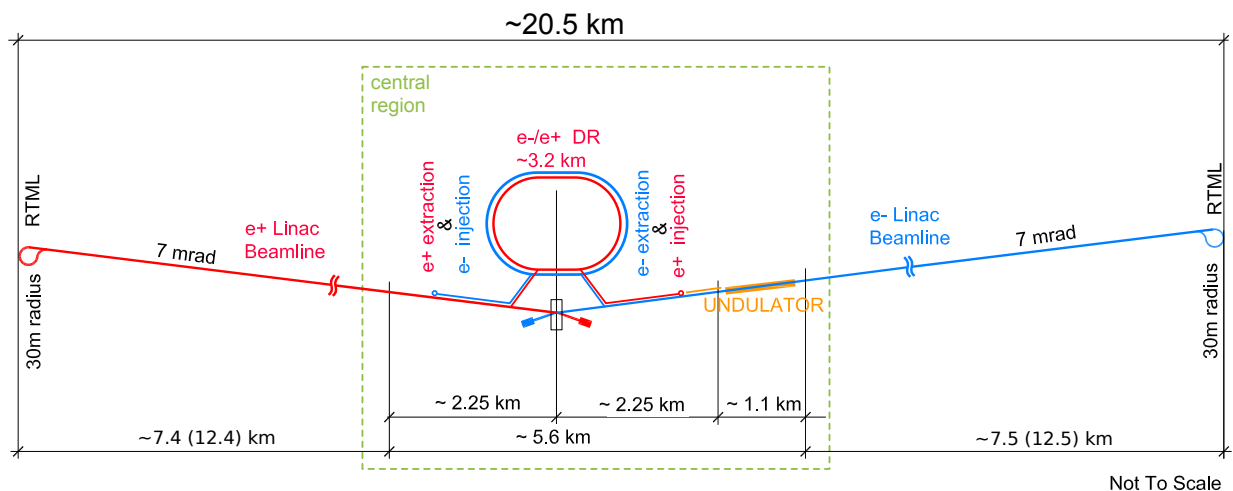


Figure 4.1: Schematic layout of the ILC in the 250 GeV staged configuration.

### 4.1.1 Design evolution since the TDR

Soon after the discovery of the Higgs boson, the Technical Design Report (TDR) for the ILC accelerator was published in 2013 [3, 4] after 8 years of work by the Global Design Effort (GDE). The TDR design was based on the requirements set forth by the ICFA mandated parameters committee [14]:

- a centre-of-mass energy of up to 500 GeV,
- tunability of the centre-of-mass energy between  $\sqrt{s} = 200$  GeV and 500 GeV,
- a luminosity sufficient to collect  $500 \text{ fb}^{-1}$  within four years of operation, taking into account a three-year ramp up. This corresponds to a final luminosity of  $250 \text{ fb}^{-1}$  per year and an instantaneous luminosity of  $\mathcal{L} = 2 \cdot 10^{34} \text{ cm}^{-2} \text{ s}^{-1}$ ,
- an electron polarisation of at least 80 %,
- the option for a later upgrade to energies up to 1 TeV.

The accelerator design presented in the TDR met these requirements (see Tab. 4.1), at an estimated construction cost of 7,982 MILCU for a Japanese site, plus 22.9 Mh (million hours) of labour in participating institutes [4, Sec. 15.8.4]. Costs were expressed in ILC Currency Units ILCU, where 1 ILCU corresponds to 1 US\$ at 2012 prices.

In the wake of the Higgs discovery, and the proposal by the Japan Association of High Energy Physicists (JAHEP) to host the ILC in Japan [11] with its recommendation to start with a 250 GeV machine [12], plans were made for a less expensive machine configuration with a centre-of-mass energy of  $\sqrt{s} = 250$  GeV, around the maximum of the  $Zh$  production cross section, half the TDR value. Various options were studied in the TDR [4, Sect. 12.5] and later [15]. This resulted in a revised proposal [9] for an accelerator with an energy of 250 GeV and a luminosity of  $\mathcal{L} = 1.35 \cdot 10^{34} \text{ cm}^{-2} \text{ s}^{-1}$ , capable of delivering about  $200 \text{ fb}^{-1}$  per year, or  $400 \text{ fb}^{-1}$  within the first four years of operation, taking into account the ramp-up.

Several other changes of the accelerator design have been approved by the ILC Change Management Board since 2013, in particular:

- The free space between the interaction point and the edge of the final focus quadrupoles ( $L^*$ ) was unified between the ILD and SiD detectors [16], facilitating a machine layout with the best possible luminosity for both detectors.
- A vertical access shaft to the experimental cavern was foreseen [17], allowing a CMS-style assembly concept for the detectors, where large detector parts are built in an above-ground hall while the underground cavern is still being prepared.
- The shield wall thickness in the Main Linac tunnel was reduced from 3.5 to 1.5 m [18], leading to a significant cost reduction. This was made possible by dropping the requirement for personnel access during beam operation of the main linac.

- Power ratings for the main beam dumps, and intermediate beam dumps for beam aborts and machine tuning, were reduced to save costs [19].
- A revision of the expected horizontal beam emittance at the interaction point at 125 GeV beam energy, based on improved performance expectations for the damping rings and a more thorough scrutiny of beam transport effects at lower beam energies, lead to an increase of the luminosity expectation from 0.82 to  $1.35 \cdot 10^{34} \text{ cm}^{-2} \text{ s}^{-1}$  [20].
- The active length of the positron source undulator has been increased from 147 to 231 m to provide sufficient intensity at 125 GeV beam energy [21].

These changes contributed to an overall cost reduction, risk mitigation, and improved performance expectation.

Several possibilities were evaluated for the length of the initial tunnel. Options that include building tunnels with the length required for a machine with  $\sqrt{s} = 350 \text{ GeV}$  or  $500 \text{ GeV}$ , were considered. In these scenarios, an energy upgrade would require the installation of additional cryomodules (with RF and cryogenic supplies), but little or no civil engineering activities. In order to be as cost effective as possible, the final proposal (see Figure 1), endorsed by ICFA [22], does not include these empty tunnel options.

While the length of the main linac tunnel was reduced, the beam delivery system and the main dumps are still designed to allow for an energy upgrade up to  $\sqrt{s} = 1 \text{ TeV}$ .

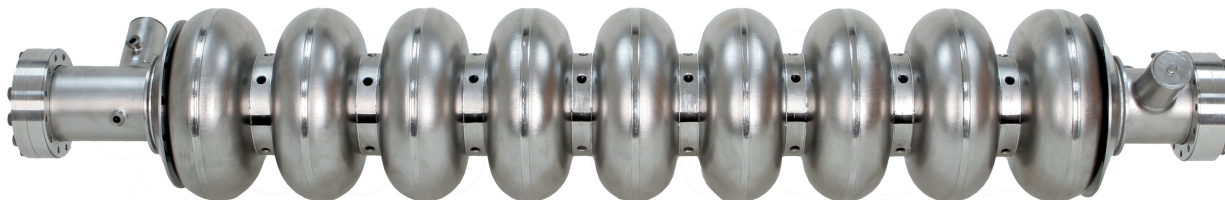


Figure 4.2: A 1.3 GHz superconducting niobium nine-cell cavity.

#### 4.1.2 Superconducting RF Technology

The heart of the ILC accelerator consists of the two superconducting Main Linacs that accelerate both beams from 5 to 125 GeV. These linacs are based on the TESLA technology: beams are accelerated in 1.3 GHz nine-cell superconducting cavities made of niobium and operated at 2 K (Fig. 4.2). These are assembled into cryomodules comprising nine cavities or eight cavities

plus a quadrupole/corrector/beam position monitor unit, and all necessary cryogenic supply lines (Fig. 4.3). Pulsed klystrons supply the necessary radio frequency power (High-Level RF HLRF) to the cavities by means of a waveguide power distribution system and one input coupler per cavity.

This technology was primarily developed at DESY for the TESLA accelerator project that was proposed in 2001. Since then, the TESLA technology collaboration [23] has been improving this technology, which is now being used in several accelerators in operation (FLASH at DESY [24, 25], E-XFEL in Hamburg [26]), under construction (LCLS-II at SLAC, Stanford, CA [27]) or planned (SHINE in Shanghai [28]).

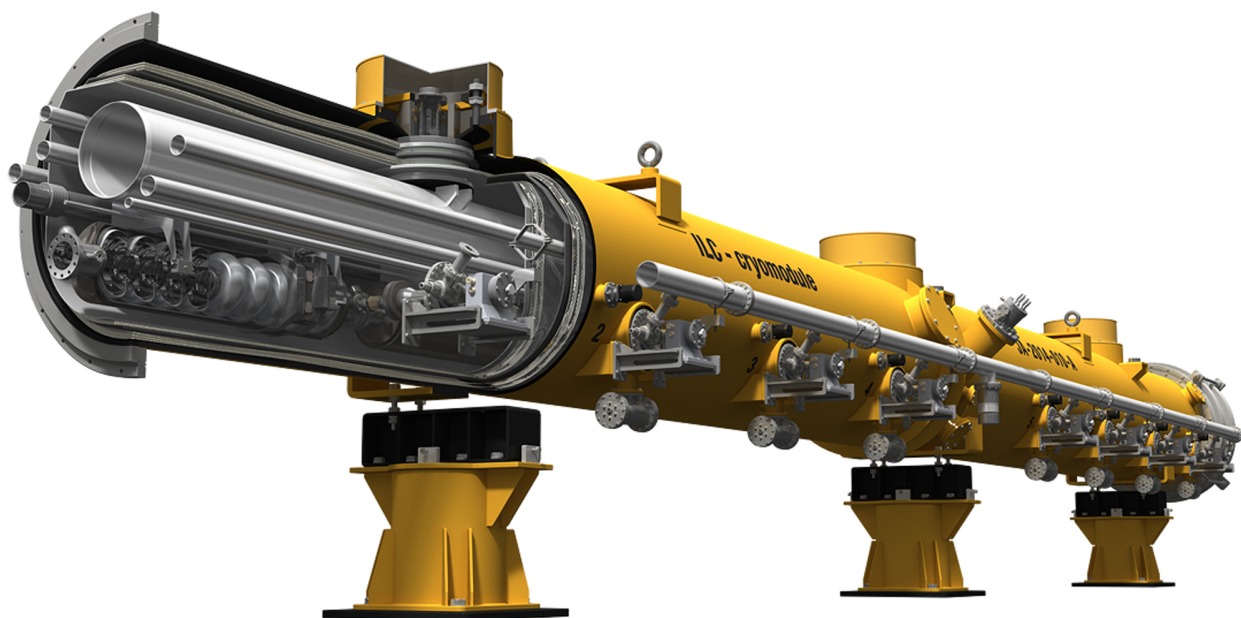


Figure 4.3: An ILC type cryomodule. ©Rey.Hori/KEK.

### The quest for high gradients

The single most important parameter for the cost and performance of the ILC is the accelerating gradient  $g$ . The TDR baseline value is an average gradient  $g = 31.5$  MV/m for beam operation, with a  $\pm 20\%$  gradient spread between individual cavities. Recent progress in R&D for high gradient cavities raises the hope to increase the gradient by 10% to  $g = 35$  MV/m, which would reduce the total cost of the 250 GeV accelerator by about 6%. To achieve the desired gradient in beam operation, the gradient achieved in the low-power vertical test (mass production acceptance test) is specified 10% higher to allow for operational gradient overhead for low-level RF (LLRF) controls, as well as some degradation during cryomodule assembly (few MV/m). Figure 4.4 shows how the

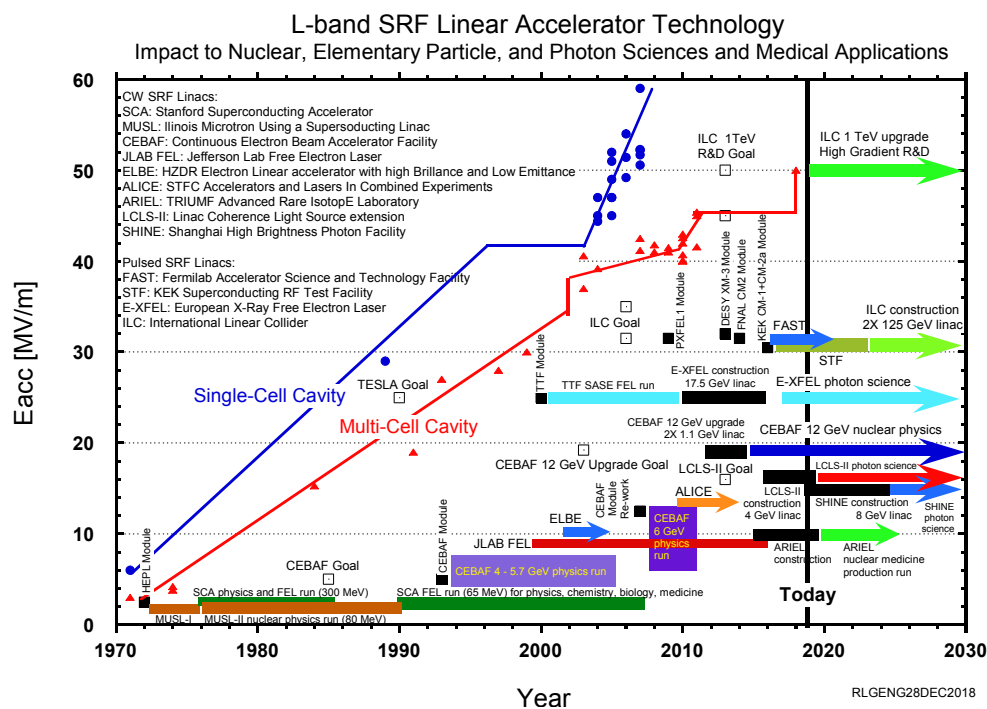


Figure 4.4: Development of the gradient of SRF cavities since 1970 [29, updated].

achievable gradients have evolved over the past 50 years [29].

**Gradient impact on costs:** To the extent that the cost of cavities, cryomodules and tunnel infrastructure is independent of the achievable gradient, the investment cost per GeV of beam energy is inversely proportional to the average gradient achieved. This is the reason for the enormous cost saving potential from higher gradients. This effect is partially offset by two factors: the energy stored in the electromagnetic field of the cavity, and the dynamic heat load to the cavity from the electromagnetic field. These grow quadratically with the gradient for one cavity, and therefore linearly for a given beam energy. The electromagnetic energy stored in the cavity must be replenished by the RF source during the filling time that precedes the time when the RF is used to accelerate the beam passing through the cavity; this energy is lost after each pulse and thus reduces the overall efficiency and requires more or more powerful modulators and klystrons. The overall cryogenic load is dominated by the dynamic heat load from the cavities, and thus operation at higher gradient requires larger cryogenic capacity. Cost models that parametrise these effects indicate that the minimum of the investment cost per GeV beam energy lies at 50 or more GeV, depending on the relative costs of tunnel, SCRF infrastructure and cryo plants, and depending on the achievable  $Q_0$  [30]. Thus, the optimal gradient is significantly higher than the value of approximately 35 MV/m that is currently realistic; this emphasises the relevance of achieving higher gradients.

It should be noted that in contrast to the initial investment, the operating costs rise when the

gradient is increased, and this must be factored into the cost model.

**Gradient limitations:** Fundamentally, the achievable gradient of a SC cavity is limited when the magnetic field at the cavity walls surpasses the critical field  $H_{\text{crit,RF}}$  of the superconductor. This gradient depends on the material, operating temperature, and the cavity geometry. For the TESLA type cavities employed at the ILC, this limit is about 48 MV/m at 2 K. The best E-XFEL production cavity reached 44.6 MV/m (Fig. 4.5). The record for single cell cavities operating at 1.3 GHz is 59 MV/m [31].

Niobium is a type-II superconductor, and so it has two distinct superconducting phases, the Meissner state, with complete magnetic flux expulsion, which exists up to a field strength  $H_{c1} \approx 180 \text{ mT}/\mu_0$  ( $\mu_0 = 4\pi 10^{-7} \text{ T m/A}$  being the vacuum permeability), and a mixed state in which flux vortices penetrate the material, up to a higher field strength  $H_{c1}$ , at which superconductivity breaks down completely. In time-dependent fields, the penetrating vortices move due to the changing fields and thus dissipate energy, causing a thermal breakdown. However, for RF fields, the Meissner state may persist metastably up to the superheating field strength  $H_{\text{sh}} \approx 240 \text{ mT}/\mu_0$ , which is expected to be the critical RF field critical field  $H_{\text{crit,RF}}$  [32]. Experimentally, niobium RF cavities have been operated at field strengths as high as  $H = 206 \text{ mT}/\mu_0$  [31], and the best E-XFEL production cavities reach about 190 mT. Recently, even 210 mT has been achieved at FNAL [33]. In recent years, theoretical understanding of the nature of this metastable state and the mechanisms at the surface that prevent flux penetration has significantly improved [34, 35]. It appears that a thin layer of “dirty” niobium, *i.e.*, with interstitial impurities, on top of a clean bulk with good thermal conductivity, is favourable for high field operation.

The gradient at which a SC cavity can be operated in practice is limited by three factors in addition to those just listed [32]:

- the thermal breakdown of superconductivity, when local power dissipation causes a local quench of the superconductor,
- the decrease of the quality factor  $Q_0$  at high gradients that leads to increased power dissipation,
- the onset of field emission that causes the breakdown of the field in the cavity.

The onset of these adverse effects is mostly caused by micro-metre sized surface defects of various kinds. Producing a sufficiently defect-free surface in an economic way is thus the central challenge in cavity production.

More than 20 years of industrial production of TESLA type cavities have resulted in a good understanding which production steps and quality controls are necessary to produce cavities with high-quality, nearly defect-free surfaces that are capable of achieving the desired high field strengths at a reasonable production yield.

**Results from E-XFEL cavity production:** The production and testing of 831 cavities for the E-XFEL [36, 37] provides the biggest sample of cavity production data so far. Cavities were acquired

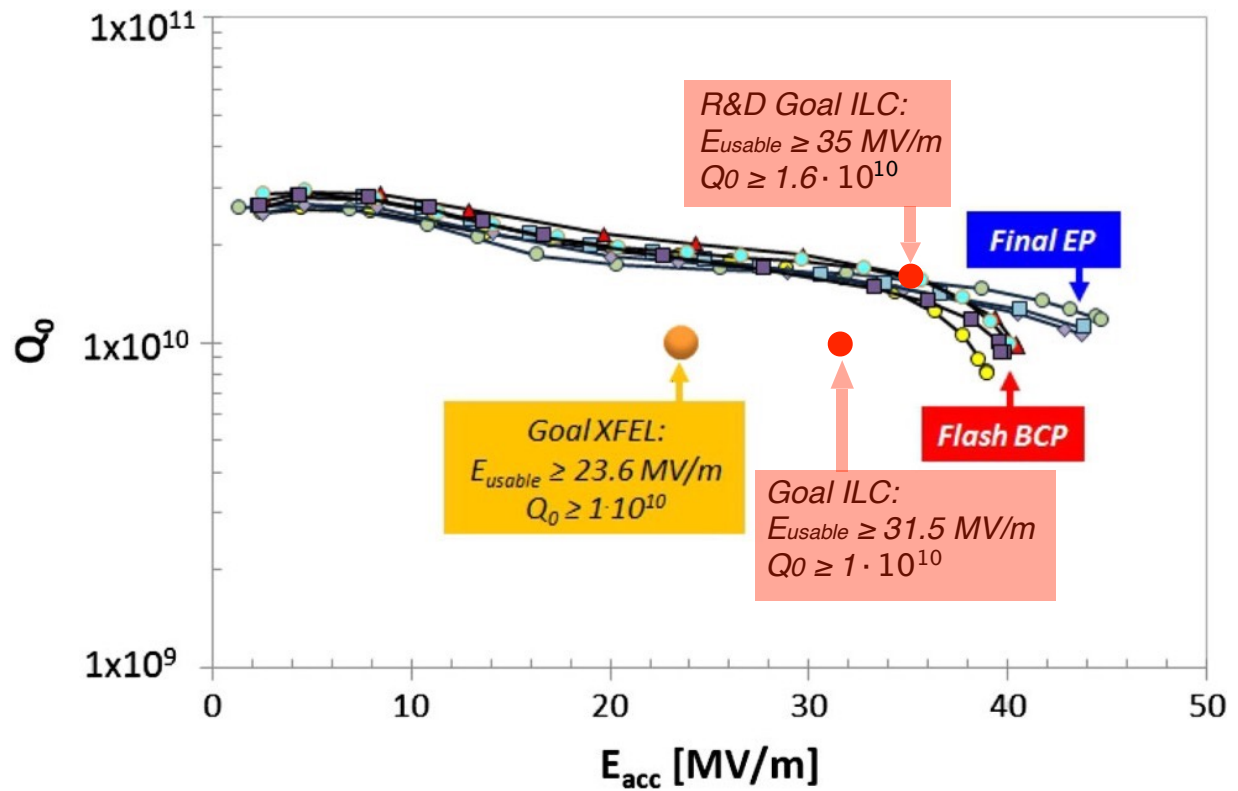


Figure 4.5: Examples of the  $Q_0(E_{acc})$  curves of some of the best cavities, either treated at RI using “EP final”, or at EZ using “BCP flash.” [36, Fig. 19]. Vendor “RI” employs a production process that closely follows the ILC specifications, with a final electropolishing step. The ILC gradient /  $Q_0$  goals are overlaid.



from two different vendors, RI and EZ. Vendor RI employed a production process with a final surface treatment closely following the ILC specifications, including a final electropolishing (EP) step, while the second vendor EZ used buffered chemical polishing (BCP). The E-XFEL specifications asked for a usable gradient of 23.6 MV/m with a  $Q_0 \geq 1 \cdot 10^{10}$  for operation in the cryomodule; with a 10% margin this corresponds to a target value of 26 MV/m for the performance in the vertical test stand for single cavities. Figure 4.5 shows the  $Q_0$  data versus accelerating gradient of the best cavities received, with several cavities reaching more than 40 MV/m, significantly beyond the ILC goal, already with  $Q_0$  values that approach the target value  $1.6 \cdot 10^{10}$  that is the goal of future high-gradient R&D.

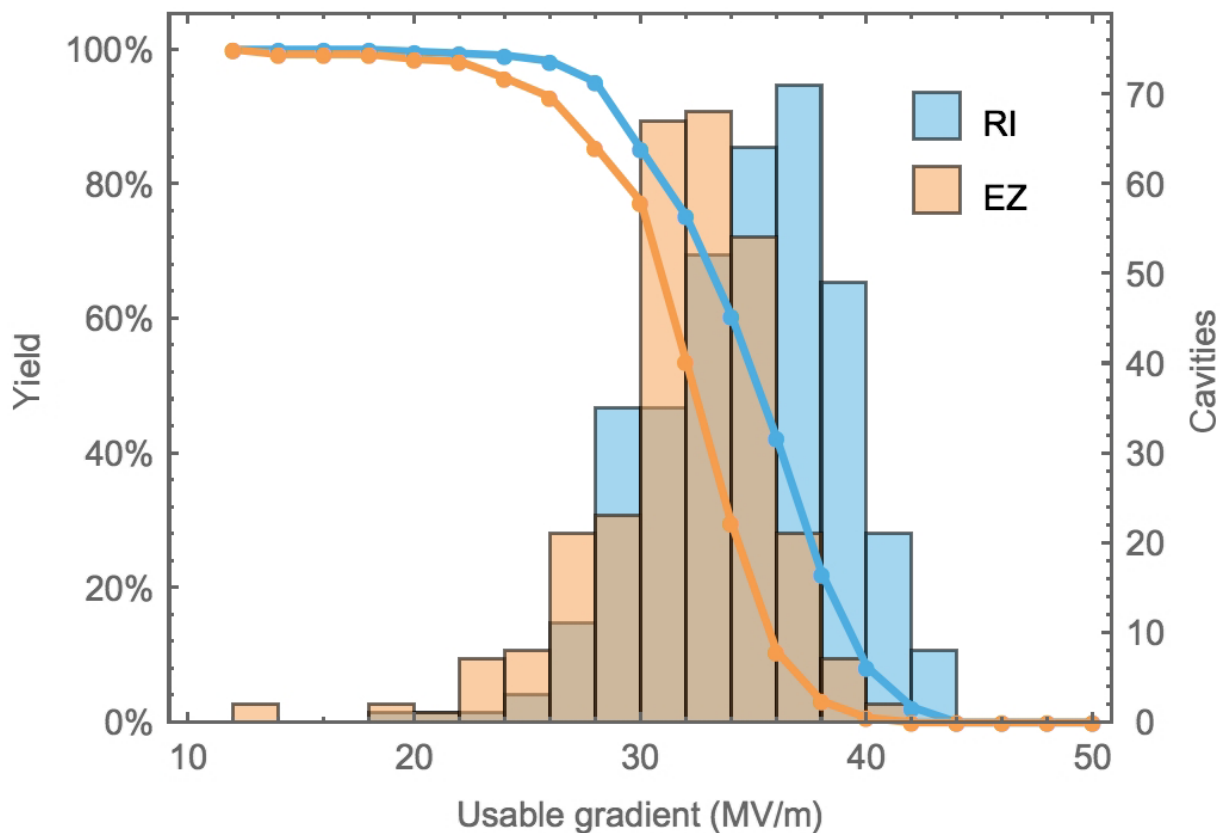


Figure 4.6: Distribution and yield of the “as received” maximum gradient of cavities produced for the E-XFEL, separated by vendor [37, Fig. 33]. Vendor RI employs a production process that closely follows the ILC specifications, with a final electro polishing step.

E-XFEL production data, in particular from vendor RI, provide excellent statistics for the cavity performance as received from the vendors, as shown in Fig. 4.6. For vendor RI, the yield for cavities with a maximum gradient above 28 MV/m is 85%, with an average of 35.2 MV/m for the cavities that pass the cut.

Since the E-XFEL performance goal was substantially lower than the ILC specifications, cavities



with gradient below 28 MV/m, which would not meet ILC specifications, were not generally re-treated for higher gradients, limiting our knowledge of the effectiveness of re-treatment for large gradients. Still, with some extrapolation it is possible to extract yield numbers applicable to the ILC specifications [38].

The E-XFEL data indicate that after re-treating cavities with gradients outside the ILC specification of  $35 \text{ MV/m} \pm 20\%$ , *i.e.*, below 28 MV/m, a yield of 94% for a maximum gradient above 28 MV/m can be achieved, with an average value of 35 MV/m, meeting the ILC specification. Taking into account limitations from  $Q_0$  and the onset of field emission, the usable gradient is lower. This gives a 82 (91)% yield and an average usable gradient of 33.4 MV/m after up to one (two) re-treatments. The re-treatment and testing rate is significantly higher than assumed in the TDR, but the E-XFEL experience shows that re-treatment can mostly be limited to a simple high-pressure rinse (HPR) rather than an expensive electropolishing step.

Overall, the E-XFEL cavity production data prove that it is possible to mass-produce cavities meeting the ILC specifications as laid out in the TDR with the required performance and yield.

### Basic parameters

The choice of operating frequency is a balance between the higher cost of larger, lower-frequency cavities and the increased cost at higher frequency associated with the lower sustainable gradient from the increased surface resistivity. The optimum frequency is in the region of 1.5 GHz, but during the early R&D on the technology, 1.3 GHz was chosen due to the commercial availability of high-power klystrons at that frequency.

### Cavities

The superconducting accelerating cavities for the ILC are nine-cell structures made out of high-purity niobium (Fig. 4.2), with an overall length of 1.25 m. Cavity production starts from niobium ingots which are forged and rolled into 2.8 mm thick niobium sheets that are individually checked for defects by an eddy current scan and optical inspection [3]. Cavity cells are produced by deep-drawing the sheets into half cells, 18 of which are joined by electron beam welding with two end groups to form the whole structure. This welding process is one of the most critical and cost-intensive steps of the cavity manufacturing procedure. Utmost care must be taken to avoid irregularities, impurities and inclusions in the weld itself, and deposition of molten material at the inner surface of the cavity that can lead to field emission.

After welding, the inner surface of the cavity must be prepared. The process is designed to remove material damage incurred by chemical procedures during the fabrication process, chemical residues from earlier production steps, hydrogen in the bulk niobium from earlier chemical processing, and contamination from particles. In a last step, the cavity is closed to form a hermetically sealed structure ready for transport. The treatment steps involve a series of rinses with ethanol or high pressure water, annealing in a high purity vacuum furnace at 800°C and 120°C, and electropolishing or buffered chemical polishing. The recipe for the surface preparation has been

developed over a long time. Still, it remains subject to optimisation, since it is a major cost driver for the cavity production and largely determines the overall performance and yield of the cavities. In particular the electropolishing steps are complicated and costly, as they require complex infrastructure and highly toxic chemicals. One advantage of nitrogen infusion (see Sec. 4.1.2) is that the final electropolishing step is omitted.

Careful quality control during the production process is of high importance. At the E-XFEL, several quality controls were conducted by the manufacturer during production, with nonconformities reported to the institute responsible for the procurement, where a decision was made whether to accept or reject a part [36]. With this “build to print” approach, in which the manufacturer guarantees that a precise production process will be followed but does not guarantee a specific performance, procurement costs are reduced, because the manufacturer does not carry, and does not charge for, the performance risk.

Upon reception from the manufacturer, cavities are tested in a vertical cryostat (“vertical test”), where  $Q_0$  is measured as a function of the gradient. Cavities that fall below the specified gradient goal are re-treated by an additional (expensive) electropolishing step or a comparatively simple high-pressure rinse. After retreatment, the vertical test is repeated.

Re-treatment and tests constitute a major cost driver in cavity production. For the ILC TDR, it was assumed that 25 % of the cavities would fall below the 28 MV/m gradient threshold and undergo re-treatment and a second vertical test. E-XFEL data from the vendor “RI” that followed the ILC production recipe indicate that 15 % to 37 % of the cavities fall below 28 MV/m, depending on whether the maximum or the “usable” achieved gradient is considered [38]. However, E-XFEL experience also shows that, in most of the cases, a high-pressure rinse is sufficient as re-treatment to remove surface defects, which is a cost saving compared to the electropolishing assumed in the TDR.

After successful testing, prior to installation in the cryomodule, cavities are equipped with a magnetic shield and the frequency tuner, which exerts mechanical force on the cavity to adjust the resonant frequency to the frequency of the external RF field [4, Sect. 3.3].

## Power coupler

The power coupler transfers the radio frequency (RF) power from the waveguide system to the cavity. In the ILC, a coupler with a variable coupling is employed; this is realised using a movable antenna. Another role of the coupler is to separate the cavity vacuum from the atmospheric pressure in the waveguide, and to insulate the cavity at 2 K from the surrounding room temperature. Thus, the coupler has to fulfill a number of demanding requirements: transmission of high RF power with minimal losses and no sparking, vacuum tightness and robustness against window breaking, and minimal heat conductivity. As a consequence, the coupler design is highly complex, with a large number of components and several critical high-tech manufacturing steps.

The baseline coupler design was originally developed in the 1990s for the TESLA Test Facility (TTF, now FLASH) at DESY, and has since been modified by a collaboration of LAL and DESY for use in the E-XFEL. About 840 of these couplers (depicted in Fig. 4.7) were fabricated by three

different companies for the E-XFEL [39], where 800 are now in operation. A lot of experience has been gained from this production [40].

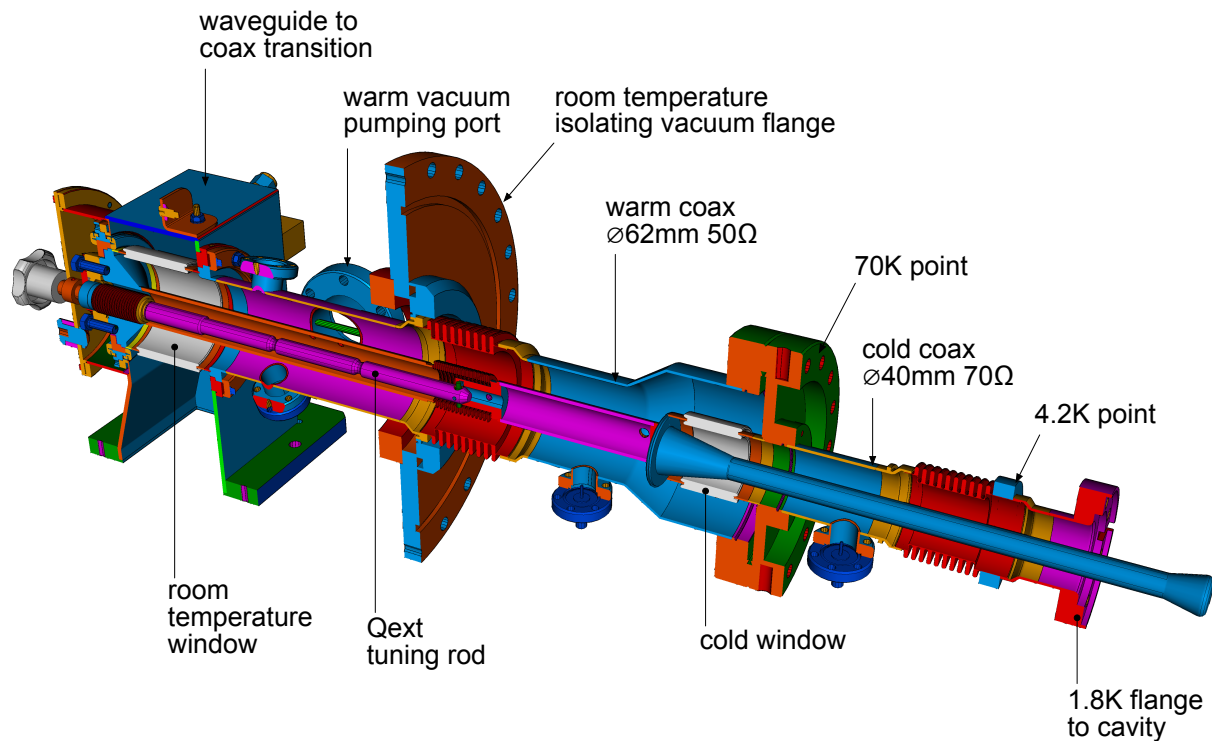


Figure 4.7: An E-XFEL type coupler.

## Cryomodules

To facilitate transportation, installation and operation, 8 or 9 cavities are integrated into a 12.6 m long cryomodule (Fig. 4.3), which houses the cavities, thermal insulation, and all necessary supply tubes for liquid and gaseous helium at 2 – 80 K temperature.

Nine of these cryomodules are connected in the tunnel to form a cryostrapping with a common liquid helium supply. RF for one such string is provided by two klystrons. No separate helium transfer line is necessary, as all helium transport lines are integrated within the modules. A quadrupole / beam position monitor / corrector magnet unit is mounted instead of the 9th cavity in every third module. Figure 4.8 shows installed cryomodules in the tunnel of the E-XFEL [41].

Cryomodule assembly requires a dedicated facility with large clean rooms, especially trained, experienced personnel, and thorough quality control [42]. The cryomodules are certified for liquid helium pressure of up to 2 bar. Thus they must conform to the applicable pressure vessel codes, which brings with it very stringent documentation requirements for all pressure bearing parts [43].

For the E-XFEL project, 103 cryomodules were assembled in a facility built and operated by

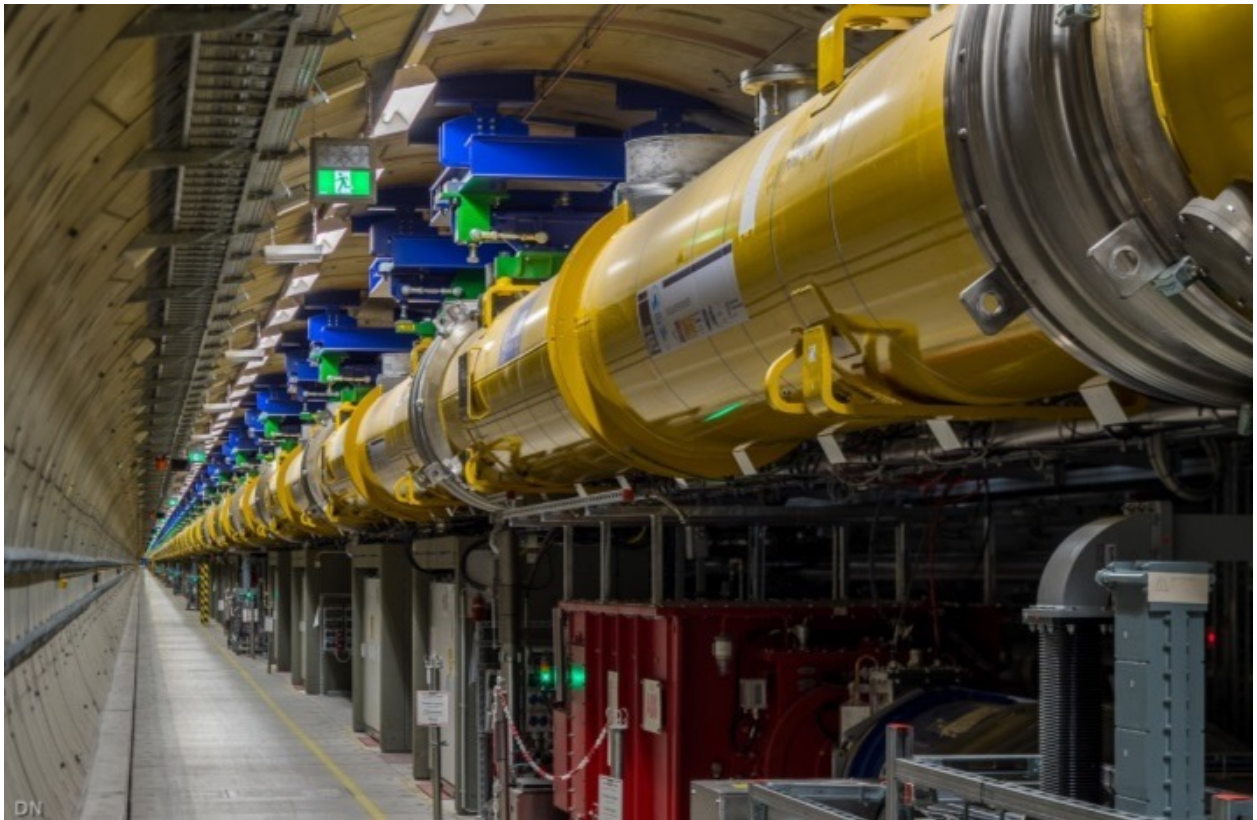


Figure 4.8: View of installed cryomodules in the tunnel of the E-XFEL [41].

CEA [44, 42] and industrial partners, demonstrating the successful industrialization of the assembly process, with a final throughput of one cryomodule every four working days. This production rate is close to the rate envisaged for a possible European contribution of 300 cryomodules to a 250 GeV ILC in Japan.

While the design gradient for E-XFEL accelerator modules of 23.6 MV/m is significantly lower than the aim of 31.5 – 35 MV/m for the ILC, a number of cryomodules have been built around the world that come close or reach the ILC TDR specification of 31.5 MV/m: An E-XFEL prototype module at DESY reached 30 MV/m [45], Fermilab has demonstrated cryomodule operation at the ILC specification of 31.5 MV/m [46], and KEK has reported stable pulsed operation of a cryomodule at 36 MV/m [47].

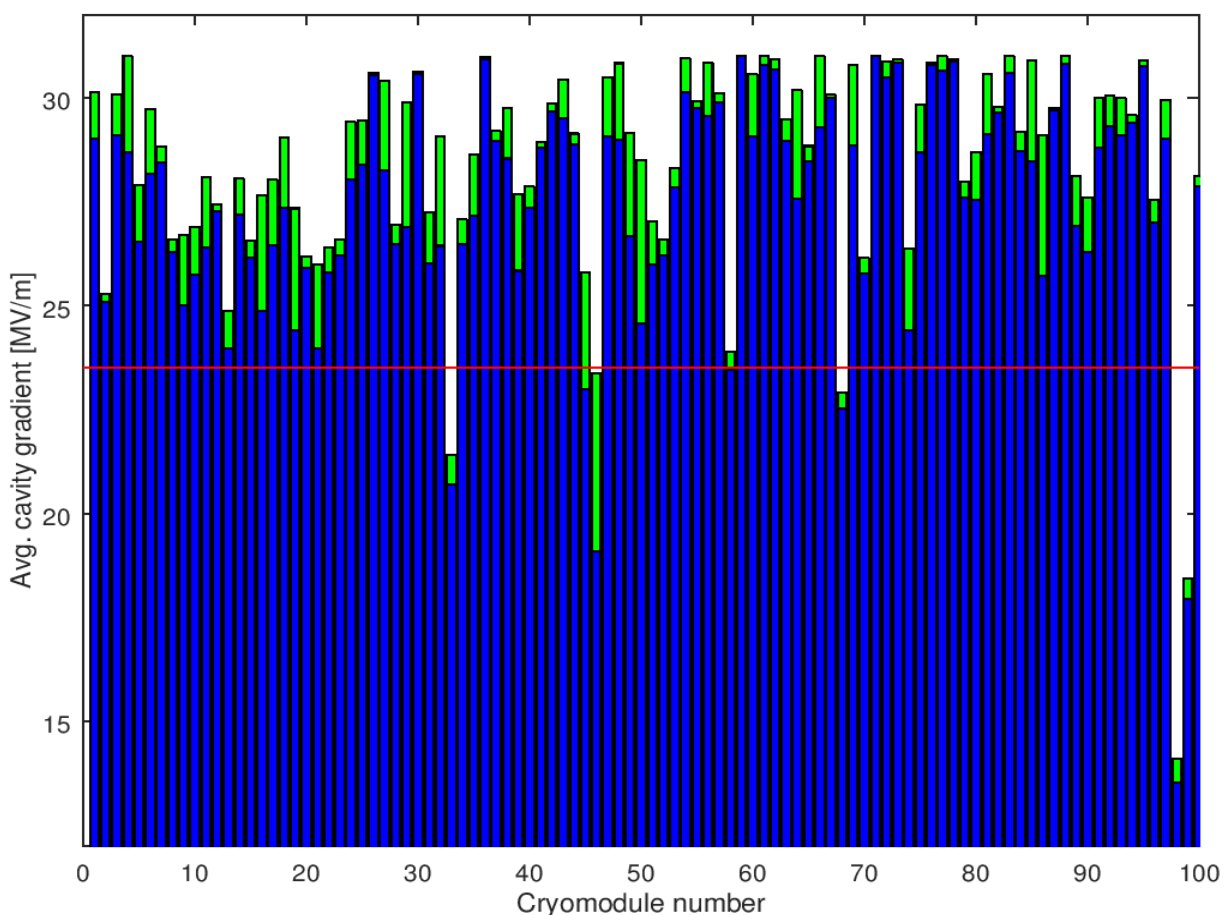


Figure 4.9: Average of the operating (blue) and maximum (green) gradient for cavities in each E-XFEL serial-production cryomodule. The specification of 23.6 MV/m is marked by a red line [48]. Modules 98 and 99 were assembled from the lowest-performing cavities.

Figure 4.9 shows the average cavity gradients per cryomodule for the E-XFEL serial-production cryomodules [48]. In the tests, the gradients were limited administratively to 31 MV/m; the true

maxima might be higher. For almost all of the modules, the cavity gradients are significantly above the E-XFEL specification of 23.6 MV/m.

### Plug-compatible design

In order to allow various designs of sub-components from different countries and vendors to work together in the same cryomodule, a set of interface definitions has been internationally agreed upon. This “plug-compatible” design ensures that components are interchangeable between modules from different regions and thus reduces the cost risk. Corresponding interface definitions exist for the cavity, the fundamental-mode power coupler, the mechanical tuner and the helium tank. The “S1Global” project [49] has successfully built a single cryomodule from several cavities equipped with different couplers and tuners, demonstrating the viability of this concept.

### High-level radio-frequency

The high-level radio-frequency (HLRF) system provides the RF power that drives the accelerating cavities. The system comprises modulators, pulsed klystrons, and a waveguide power distribution system.

**Modulators:** The modulators provide the short, high-power electrical pulses required by the pulsed klystrons from a continuous supply of electricity. The ILC design foresees the use of novel, solid state Marx modulators. These modulators are based on a solid-state switched capacitor network, where capacitors are charged in parallel over the long time between pulses, and discharged in series during the short pulse duration, transforming continuous low-current, low voltage electricity into short high-power pulses of the required high voltage of 120 kV at a current of 140 A, over 1.65 ms. Such Marx modulators have been developed at SLAC [50] and successfully tested at KEK [51]. However, long-term data about the required large mean time between failures (MTFB) are not yet available.

**Klystrons:** The RF power to drive the accelerating cavities is provided by 10 MW L-band multi-beam klystrons. Devices meeting the ILC specifications were initially developed for the TESLA project, and later for the E-XFEL. They are now commercially available from two vendors (Thales and Toshiba), both of which provided klystrons for the E-XFEL. The ILC specifications ask for a 65% efficiency (drive beam to output RF power), which are met by the existing devices.

Recently, the High Efficiency International Klystron Activity (HEIKA) collaboration [52, 53] has been formed that investigates novel techniques for high-efficiency klystrons. Taking advantage of modern beam dynamic tools, methods such as the Bunching, Alignment and Collecting (BAC) method [54] and the Core Oscillation Method (COM) [55] (Fig. 4.10) have been developed that promise increased efficiencies up to 90% [56]. One advantage of these methods is that it is possible to increase the efficiency of existing klystrons by equipping them with a new electron optics, as was



demonstrated retrofitting an existing tube from VDBT, Moscow. This increased the output power by almost 50 % and its efficiency from 42 % to 66 % [57].

To operate the ILC at an increased gradient of 35 MV/m would require that the maximum klystron output power is increased from 10 to 11 MW. It is assumed that this will be possible by applying the results from this R&D effort to high-efficiency klystrons.

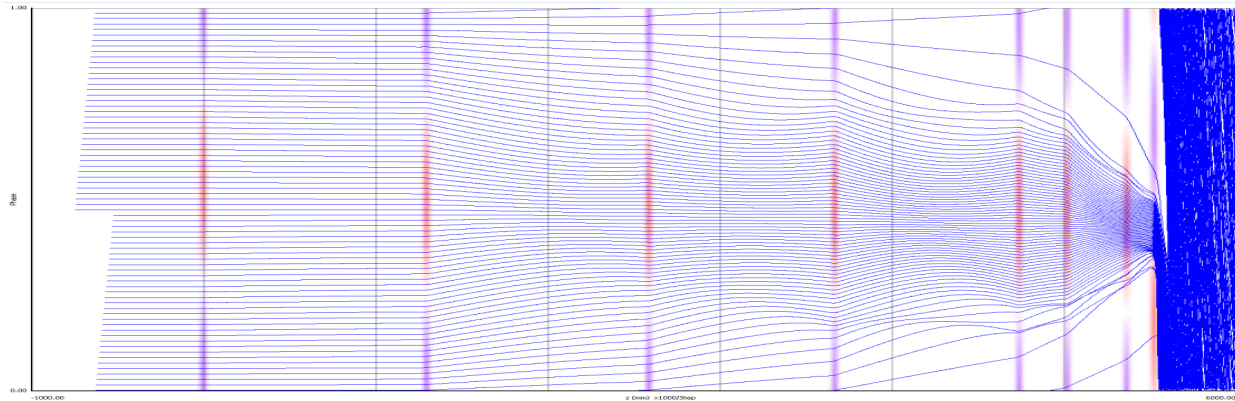


Figure 4.10: Electron phase profile of an 800 MHz klystron employing the Core Oscillation Method (COM) [55].

**Local Power–Distribution System (LPDS):** In the baseline design, a single RF station with one modulator and klystron supplies RF to 39 cavities, which corresponds to 4.5 cryomodules [4, Sec. 3.6.4]. Then 2 klystrons drive a 9 cryomodule cryo-string unit. The power is distributed by the LPDS, a system of waveguides, power dividers and loads. All cavities from a 9-cavity module and half of a 8-cavity module are connected in one LPDS, and three such LPDS units are connected to one klystron. This arrangement allows an easy refurbishment such that a third klystron can be added to a cryo-string, increasing the available power per cavity by 50 % for a luminosity upgrade (cf. Sec. 4.1.4).

The LPDS design must provide a cost-effective solution for the distribution of the RF power with minimal losses, and at the same time provide the flexibility to adjust the power delivered to each cavity by at least  $\pm 20\%$  to allow for the specified spread in maximum gradient. The LPDS design therefore contains remotely controlled, motor-driven Variable Power Dividers (VPD), phase shifters, and H-hybrids that can distribute the power with the required flexibility. This design allows one to optimise the power distribution during operation, based on the cavity performance in the installed cryomodule, and thus to get the optimum performance out of the system. It does not require a measurement of the individual cavity gradients after the module assembly, and is thus compatible with the ILC production scheme, where only a fraction of the cryomodules are tested. This is a notable difference from the scheme employed at the E-XFEL, where 100 % of the modules were tested, and the the power distribution for each module was tailored to the measured cavity gradients, saving investment costs for the LPDS but making the system less flexible.

## Cryogenics

The operation of the large number of superconducting cryomodules for the main linacs and the linacs associated with the sources requires a large-scale supply of liquid helium. The cryomodules operate at 2 K and are cooled with superfluid helium, which at 2 K has a vapour pressure of about 32 mbar.

The accelerator is supplied with liquid helium by several cryogenic plants [4, Sec. 3.5] of a size similar to those in operation at CERN for the LHC, at Fermilab, and DESY, with a cooling capacity equivalent to about 19 kW at 4.5 K. The 2 K and 4.5 K helium refrigerators are located in an underground access hall [58] that is connected to the surface, where the helium compressors, gas tanks and further cryogenic infrastructure are located. The total helium inventory is approximately 310000 liquid litres or about 41 metric tonnes, about one third of the LHC's helium inventory. A factor 2 more helium is needed for 500 GeV operation.

## Series production and industrialisation

Due to the construction of the E-XFEL, the industrial basis for the key SCRF components is broad and mature. In all three regions (Europe, America, Asia), several vendors for cavities have been qualified for ILC type cavities, and provided cost estimates in the past. RF couplers have also been successfully produced by European and American vendors for the E-XFEL and LCLS-II projects.

ILC/TESLA type cryomodules have been built in laboratories around the world (DESY, CEA in Europe, FNAL and JLAB in America, KEK in Asia). Series production has been established in America at Fermilab and JLAB for LCLS-II. The largest series production was conducted by CEA in France, again for the E-XFEL, with the assembly of 103 cryomodules in total by an industrial partner under the supervision of CEA personnel, with a final throughput of one cryomodule produced every four working days.

ILC type, pulsed 10 MW klystrons are commercially available from two vendors in Japan and Europe.

### 4.1.3 Accelerator design

#### Electron and positron sources

The electron and positron sources are designed to produce 5 GeV beam pulses with a bunch charge that is 50% higher than the design bunch charge of 3.2 nC ( $2 \cdot 10^{10}$  e), in order to have sufficient reserve to compensate any unforeseen inefficiencies in the beam transport. In the baseline design, both sources produce polarized beams with the same time structure as the main beam, *i.e.*, 1312 bunches in a 727  $\mu$ s long pulse.

The electron source design [4] is based on the SLC polarized electron source, which has demonstrated that the bunch charge, polarisation and cathode lifetime parameters are feasible. The long bunch trains of the ILC do require a newly developed laser system and powerful preaccelerator



structures, for which preliminary designs are available. The design calls for a Ti:sapphire laser impinging on a photocathode based on a strained GaAs/GaAsP superlattice structure, which will produce electron bunches with an expected polarisation of 85 %, sufficient for 80 % beam polarisation at the interaction point, as demonstrated at SLAC [59].

The positron source poses a larger challenge.

In the baseline design, hard gamma rays are produced in a helical undulator driven by the main electron beam, which are converted to positrons in a rotating target. Positrons are captured in a flux concentrator or a quarter wave transformer, accelerated to 400 MeV in two normal conducting preaccelerators followed by a superconducting accelerator very similar to the main linac, before they are injected into the damping rings at 5 GeV. The helical undulators produce photons with circular polarisation, which is transferred to the positrons produced in the target, which are longitudinally polarised as a result. The positron polarisation thus achieved is 30 %. The E-166 experiment at SLAC has successfully demonstrated this concept [60], albeit at intensities much lower than foreseen for the ILC. Technological challenges of the undulator source concept are the target heat load, the radiation load in the flux concentrator device, and the dumping of the high intensity photon beam remnant.

As an alternative, an electron-driven positron source concept has been developed. In the electron-driven scheme, a 3 GeV electron beam from a dedicated normal conducting linac produces positrons in a rotating target. The electron drive beam, being independent from the main linac, has a completely different time structure. Positrons are produced in 20 pulses at 300 Hz with 66 bunches each. With this scheme, it takes about 67 ms to produce the positrons needed for a single Main Linac pulse with its 1312 bunches, compared to 0.8 ms for the undulator source. This different time structure spreads the heat load on the target over a longer time, allowing a target rotation speed of only 5 m/s rather than 100 m/s, which reduces the engineering complexity of the target design, in particular the vacuum seals of the rotating parts. Although not free from its own engineering challenges, such as the high beam loading in the normal conducting cavities, the electron driven design is currently considered to be a low risk design that is sure to work.

Aside from the low technical risk, the main advantage of the electron driven design is the independence of positron production and electron main linac operation, which is an advantage for accelerator commissioning and operation in general. In particular, electron beam energies below 120 GeV for operation at the  $Z$  resonance or the  $WW$  threshold would be no problem. The undulator source, on the other hand, offers the possibility to provide beams at the maximum repetition rate of 10 Hz given by the damping time in the damping rings of 100 ms, whereas the electron driven scheme is limited to 6 Hz due to the additional 66 ms for positron production. The main difference between the concepts is the positron polarisation offered by the undulator source, which adds significantly to the physics capabilities of the machine. The physics implications of positron polarization is discussed later in the report, in Sec. 5.3.

Both concepts have been reviewed recently [21] inside the ILC community, with the result that both source concepts appear viable, with no known show stoppers, but they require some more engineering work. The decision on the choice will be taken once the project has been approved, based on the physics requirements, operational aspects, and technological maturity and risks.

**Beam polarisation and spin reversal** At the ILC, the electron beam and potentially the positron beam are longitudinally polarised at the source, *i.e.*, the polarisation vector is oriented parallel or antiparallel to the beam direction. Whenever a longitudinally polarised beam of energy  $E_{\text{beam}}$  is deflected by an angle  $\theta_{\text{bend}}$ , the polarisation vector undergoes a precession through an angle  $\theta_{\text{pol}} = \gamma a \theta_{\text{bend}}$  [61], with the Lorentz factor  $\gamma = E_{\text{beam}}/m_e$  and the electron's anomalous magnetic moment  $a = (g - 2)/2$ . To preserve the longitudinal beam polarisation during the long transport from the source through the damping rings to the start of the main linac, which involves many horizontal bends, the beam polarisation vector is rotated into the transverse plane, perpendicular to the damping ring plane, before the beam is transferred to the damping rings, and rotated back to a longitudinal direction by a set of spin rotators at the end of the RTML (see Sec. 4.1.3). Through the use of two rotators, it is possible to bring the polarisation vector into any desired direction, and compensate any remaining net precession between these spin rotators and the interaction point, so that any desired longitudinal or transverse polarisation at the IP can be provided.

To control systematic effects, fast helicity reversal is required. This is helicity reversal of each beam independently, on a pulse to pulse basis, which must be achieved without a change of the magnetic fields of the spin rotator magnets. For the electron beam, a fast helicity reversal is possible through a flip of the cathode laser polarisation. For the undulator-based positron source, the photon polarisation is given by the undulator field. Two parallel sets of spin rotators in front of the damping rings are used that rotate the polarisation vector either to the  $+y$  or  $-y$  direction. With this scheme, fast kickers can select a path through either of the two spin rotators and thus provide a fast spin reversal capability [61, 62].

## Damping rings

The ILC includes two oval damping rings of 3.2 km circumference, sharing a common tunnel in the central accelerator complex. The damping rings reduce the horizontal and vertical emittance of the beams by almost six orders of magnitude<sup>1</sup> within a time span of only 100 ms, to provide the low emittance beams required at the interaction point. Both damping rings operate at an energy of 5 GeV.

The damping rings' main objectives are

- to accept electron and positron beams at large emittance and produce the low-emittance beams required for high-luminosity production.
- to dampen the incoming beam jitter to provide highly stable beams.
- to delay bunches from the source and allow feed-forward systems to compensate for pulse-to-pulse variations in parameters such as the bunch charge.

Compared to today's fourth generation light sources, the target value for the normalized beam emittance ( $4 \mu\text{m}/20 \text{ nm}$  for the normalised horizontal / vertical beam emittance) is low, but not a record value, and it is thus considered to be a realistic goal.

---

<sup>1</sup>The vertical emittance of the positrons is reduced from  $\epsilon_y \approx 0.8 \mu\text{m}$  to 2 pm.

The main challenges for the damping ring design are to provide

- a sufficient dynamic aperture to cope with the large injected emittance of the positrons.
- a low equilibrium emittance in the horizontal plane.
- a very low emittance in the vertical plane.
- a small damping time constant.
- damping of instabilities from electron clouds (for the positron DR) and fast ions (for the electron DR).
- a small (3.2 – 6.4 ns) bunch spacing, requiring very fast kickers for injection and ejection.

Careful optimization has resulted in a TME (Theoretical Minimum Emittance) style lattice for the arcs that balances a low horizontal emittance with the required large dynamic aperture [4, Chap. 6]. Recently, the horizontal emittance has been reduced further by lowering the dispersion in the arcs through the use of longer dipoles [20]. The emittance in the vertical plane is minimised by careful alignment of the magnets and tuning of the closed orbit to compensate for misalignments and field errors, as demonstrated at the CESR-TA facility [63].

The required small damping time constant requires large synchrotron radiation damping, which is provided by the insertion of 54 wigglers in each ring. This results in an energy loss of up to 7.7 MV per turn and up to 3.3 MW RF power to store the positron beam at the design current of 390 mA. This actually exceeds the average beam power of the accelerated positron beam, 2.6 MW at a 250 GeV.

Electron cloud (EC) and fast ion (FI) instabilities limit the overall current in the damping rings to about 400 – 800 mA, where the EC limit that affects the positrons is assumed to be more stringent. These instabilities arise from electrons and ions being attracted by the circulating beam towards the beam axis. A low base vacuum pressure of  $10^{-7}$  Pa is required to limit these effects to the required level. In addition, gaps between bunch trains of around 50 bunches are required in the DR filling pattern, which permits the use of clearing electrodes to mitigate EC formation. These techniques have been developed and tested at the CESR-TA facility [64]

In the damping rings, the bunch separation is only 6.4 ns (3.2 ns for a luminosity upgrade to 2625 bunches). Extracting individual bunches without affecting their emittance requires kickers with rise/fall times of 3 ns or less. Such systems have been tested at ATF [65].

The damping ring RF system will employ superconducting cavities operating at half the Main Linac frequency (650 MHz). Klystrons and accelerator modules can be scaled from existing 500 MHz units in operation at CESR and KEK [4, Sec. 6.6].

### **Low emittance beam transport: ring to Main Linac (RTML)**

The Ring to Main Linac (RTML) system [4, Chap. 7] is responsible for transporting and matching the beam from the Damping Ring to the entrance of the Main Linac. Its main objectives are

- transport of the beams from the Damping Rings at the center of the accelerator complex to the upstream ends of the Main Linacs,
- collimation of the beam halo generated in the Damping Rings,
- rotation of the spin polarisation vector from the vertical to the desired angle at the IP (typically, in longitudinal direction).

The RTML consists of two arms for the positrons and the electrons. Each arm comprises a damping ring extraction line transferring the beams from the damping ring extraction into the main linac tunnel, a long low emittance transfer line (LTL), the turnaround section at the upstream end of each accelerator arm, and a spin rotation and diagnostics section.

The long transport line is the largest, most costly part of the RTML. The main challenge is to transport the low emittance beam at 5 GeV with minimal emittance increase, and in a cost-effective manner, considering that its total length is about 14 km for the 250 GeV machine.

In order to preserve the polarisation of the particles generated in the sources, their spins are rotated into a vertical direction (perpendicular to the Damping Ring plane) before injection into the Damping Rings. A set of two rotators [66] employing superconducting solenoids allows to rotate the spin into any direction required.

At the end of the RTML, after the spin rotation section and before injection into the bunch compressors (which are considered part of the Main Linac, not the RTML [67]), a diagnostics section allows measurement of the emittance and the coupling between the horizontal and vertical plane. A skew quadrupole system is included to correct for any such coupling.

A number of circular fixed-aperture and rectangular variable-aperture collimators in the RTML provide betatron collimation at the beginning of the LTL, in the turn around and before the bunch compressors.

### **Bunch compressors and Main Linac**

The heart of the ILC are the two Main Linacs, which accelerate the beams from 5 to 125 GeV. The linac tunnel, as depicted in Figs. 4.11 and 4.12, has two parts, separated by a shield wall. One side (on the right in Fig. 4.11) houses the beamline with the accelerating cryomodules as well as the RTML beamline hanging on the ceiling. The other side contains power supplies, control electronics, and the modulators and klystrons of the High-Level RF system. The concrete shield wall (indicated as a dark-grey strip in in Fig. 4.11) has a thickness of 1.5 m [18]. The shield wall allows access to the electronics, klystrons and modulators during operation of the klystrons with cold cryomodules, protecting personnel from X-ray radiation emanating from the cavities caused by dark currents. Access during beam operation, which would require a wall thickness of 3.5 m, is not possible.

The first part of the Main Linac is a two-stage bunch compressor system [4, Sec. 7.3.3.5], each consisting of an accelerating section followed by a wiggler. The first stage operates at 5 GeV, with



Figure 4.11: Artist's rendition of the ILC Main Linac tunnel. The shield wall in the middle has been removed. ©Rey.Hori/KEK.

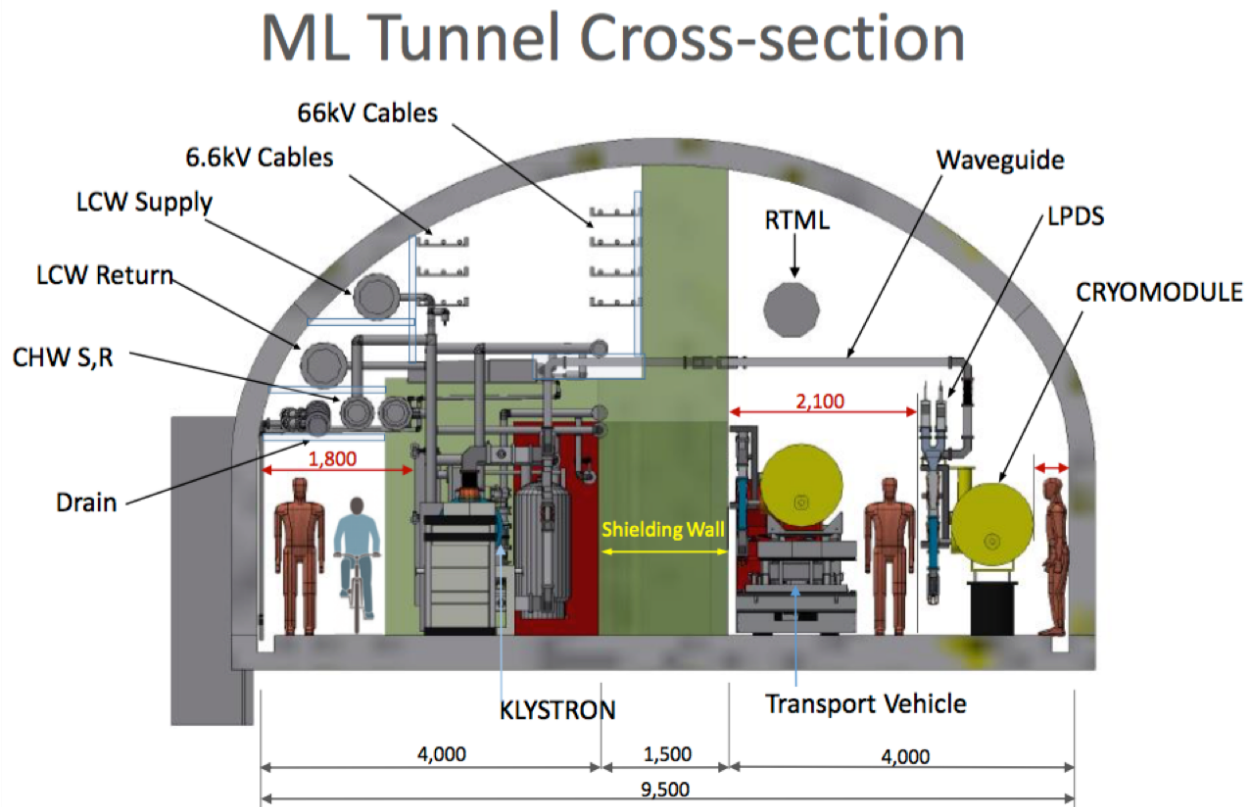


Figure 4.12: Cross section through the Main Linac tunnel.



no net acceleration, the second stage accelerates the beam to 15 GeV. The bunch compressors reduce the bunch length from 6 to 0.3 mm.

After the bunch compressors, the Main Linac continues for about 6 km with a long section consisting entirely of cryomodules, bringing the beam to 125 GeV.

**RF distribution:** Each cryomodule contains 9 cavities, or for every third module, 8 cavities and a package with a superconducting quadrupole, corrector magnets, and beam position monitor. Nine such modules, with a total of 117 cavities, are powered by 2 klystrons and provide 3.83(4.29) GeV at a gradient of 31.5(35) MV/m. Table 4.2 gives an overview over the units that form the linacs. The waveguide distribution system allows an easy refurbishment to connect a third klystron for a luminosity upgrade. The 50 % RF power increase would allow 50 % higher current through smaller bunch separation, and longer beam pulses because of a reduced filling time, so that the number of bunches per pulse and hence the luminosity can be doubled, while the RF pulse duration of 1.65 ms stays constant.

**Cryogenic supply:** A 9 module unit forms a cryo string, which is connected to the helium supply line with a Joule-Thomson valve. All helium lines are part of the cryomodule, obviating the need for a separate helium transfer line. Up to 21 strings with 189 modules and 2.4 km total length can be connected to a single plant; this is limited by practical plant sizes and the gas–return header pressure drop.

Unit	Comprises	Length	Voltage
Cavity	1.038 m active length	1.25 m	32.6/36.2 MV
Cryomodule	$8^{2/3}$ cavities	12.65 m	282/314 MV
RF Unit	4.5 cryomodules	58.2 m	1.27/1.41 GV
Cryostring	2 RF units	116.4 m	2.54/2.82 GV
Cryounit	up to 21 cryostrings	2454 m	53.4/39.3 GV

Table 4.2: Units that make up the main linacs. The voltage takes into account that the beam is  $5^\circ$  shifted in phase (“off crest”) for longitudinal stability, and is given for an average gradient of 31.5/35 MV/m. A RF unit is powered by one klystron, each cryostring is connected by a valve box to the liquid helium supply, and a cryounit is supplied by one cryogenic plant. Total lengths include additional space between components.

**Cost reduction from larger gradients:** Figure 4.13 shows the layout of the cryogenic supply system for the 250 GeV machine. At the top, the situation is depicted for the gradient of 31.5 MV/m with a quality factor of  $Q_0 = 1.0 \cdot 10^{10}$ , as assumed in the TDR [4]. In this case, the access points PM±10 would house two cryogenic plants, each supplying up to 189 cryomodules or an equivalent cryogenic load. In this configuration 6 large plants in the access halls plus 2 smaller plants in the central region would be needed. The bottom picture shows the situation for a gradient of 35 MV/m with  $Q_0 = 1.6 \cdot 10^{10}$ , as could be expected from successful R&D. The increased gradient would allow reduction of the total number of cryomodules by roughly 10 % from 987 to 906. The

increased quality factor would reduce the dynamic losses such that 4 cryo plants would provide sufficient helium.

In general, the accelerator is designed to make good use of any anticipated performance gain from continued high gradient R&D, in the case that raising the gradient is seen to be beneficial from an economical point of view, without incurring unwanted technology risk.

### Beam delivery system and machine detector interface

The Beam Delivery System (BDS) transports the  $e^+/e^-$  beams from the end of the main linacs, focuses them to the required small beam spot at the Interaction Point (IP), brings them into collision, and transports the spent beams to the main dumps [4, Chap. 8]. The main functions of the BDS are

- measuring the main linac beam parameters and matching it into the final focus.
- protecting beamline and detector from mis-steered beams <sup>2</sup>.
- removing large amplitude (beam-halo) and off-momentum particles from the beam to minimize background in the detector.
- accurately measuring the key parameters energy and polarisation before and after the collisions.

The BDS must provide sufficient diagnostic and feedback systems to achieve these goals.

The BDS is designed such that it can be upgraded to a maximum beam energy of 500 GeV; components such as the beam dumps, that are not cost drivers for the overall project but would be cumbersome to replace later, are dimensioned for the maximum beam energy from the beginning. In other places, such as the energy collimation dogleg, those components necessary for 125 GeV beam operation are installed and space for a later upgrade is reserved.

Overall, the BDS is 2254 m long from the end of the main linac (or the undulator and target bypass insert of the positron source on the electron side, respectively) to the IP.

**Diagnostics and collimation section:** The BDS starts with a diagnostics section, where emittance, energy and polarisation are measured and any coupling between the vertical and horizontal planes is corrected by a set of skew quadrupoles. The energy measurement is incorporated into the machine protection system and can, *e.g.*, extract off-momentum bunches caused by a klystron failure in the main linac that would otherwise damage the machine or detector. An emergency dump [19] is dimensioned such that it can absorb a full beam pulse at 500 GeV, sufficient for 1 TeV operation.

---

<sup>2</sup>On the electron side, the protective fast beam abort system is actually located upstream of the positron source undulator.



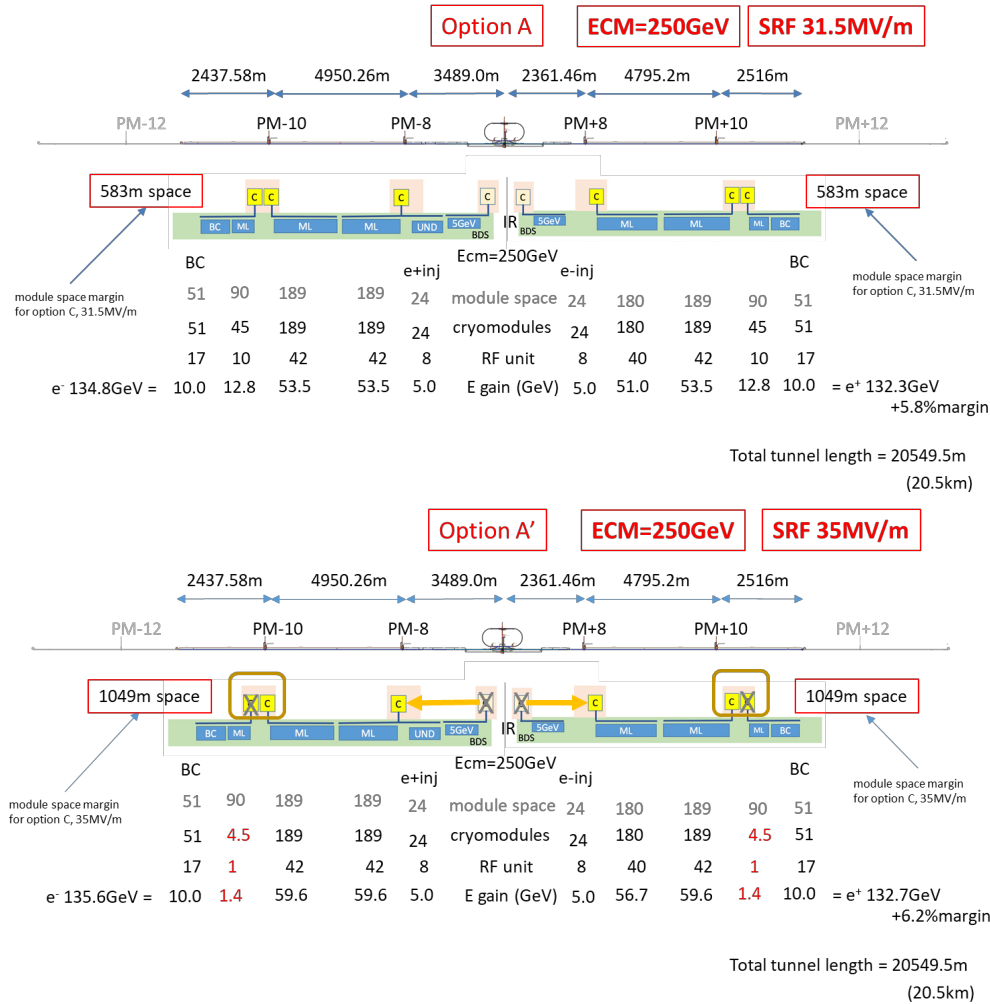


Figure 4.13: Cryogenic layout for a gradient of 31.5 MV/m (top) and 35 MV/m (bottom) [9]. “Module space” indicates how many cryomodules can be physically installed, “cryomodules” and “RF unit” indicates the number of actually installed modules and klystrons (one klystron per 4.5 cryomodules). “E gain” indicates the energy gain in GeV. “BC”, “ML”, “e+ inj”, “e- inj” and “UND” refer to the sections with need for liquid helium: bunch compressor, main linac, 5GeV boosters in the positron and electron source, and the positron source undulator section, respectively. PM±8, 10, 12 refer to access hall locations, “C” to cryo plants; meter numbers on top indicate the length of the corresponding section.

The diagnostics section is followed by a collimation system, which first removes beam halo particles (betatron collimation). Then, off-momentum particles are removed. In this energy collimation section, sufficient dispersion must be generated by bending the beam in a dogleg, while avoiding excessive synchrotron radiation generation in dispersive regions that leads to an increase of the horizontal emittance. This emittance dilution effect grows as  $E_{\text{beam}}^6$  at constant bending radius for the normalised emittance, and determines the overall length of the energy collimation section for a maximum 500 GeV beam energy to about 400 m.

**Final focus with feedback system and crab cavities:** The final focus system demagnifies the beam to the required spot size of  $516 \times 7.7 \text{ nm}^2$  by means of a final quadrupole doublet. Even the relatively small energy spread of  $\approx 0.1\%$  leads to a significant spread of the focal length of the doublet and requires a correction to achieve the desired beam size, which is realised by a local chromaticity correction scheme [68].

To bring the beams to collision with the necessary nanometre accuracy requires a continuous compensation of drift and vibration effects. Along the ILC, the pulse length and bunch separation ( $727 \mu\text{s}$  and  $554 \text{ ns}$ , respectively) are large enough to allow corrections between pulses as well as within a bunch train (intratrain feedback). Beam-beam offsets of a fraction of the beam size lead to a measurable deflection of the outgoing beams, and these measurements are used to feed fast stripline kickers that stabilize the beam. Finally, the 3.9 GHz crab cavities close to the interaction point are incorporated that rotate the bunches to compensate for the 14 mrad beam crossing angle [4, Sect. 8.9].

**Test results from ATF2:** The Accelerator Test Facility 2 (ATF2) was built at KEK in 2008 as a test bench for the ILC final focus scheme [3, Sec. 3.6]. Its primary goals were to achieve a 37 nm vertical beam size at the interaction point (IP), and to demonstrate beam stabilisation at the nanometre level [69, 70]. After scaling for the different beam energies (ATF2 operates at  $E_{\text{beam}} = 1.3 \text{ GeV}$ ), the 37 nm beam size corresponds to the TDR design value of  $\sigma_y^* = 5.7 \text{ nm}$  at 250 GeV beam energy. As Fig. 4.14 shows, this goal has been reached within 10% [71] by the successive application of various correction and stabilisation techniques, validating the final focus design, in particular the local chromaticity correction [72].

The fifth generation FONT5 feedback system [73] for the ILC and CLIC has also been tested at the ATF2, where a beam stabilisation to 41 nm has been demonstrated [74].

Since November 2016, intensity-dependence effects on the ATF2 beam size have been studied extensively. They show a degradation of the beam size with increasing intensity that is compatible with the effect of wakefields. Simulations and experiments in ATF2 show that the effect is not important when scaled to ILC. Also, it could be mitigated by including a dedicated “wakefield knob” in the routine tuning procedure.

**Machine detector interface (MDI):** The ILC is configured to have two detectors that share one interaction point, with one detector in data taking position at any time, in a so-called “push–pull” operation [3, Sec. 8.4]. Both detectors are mounted on movable platforms that allow an

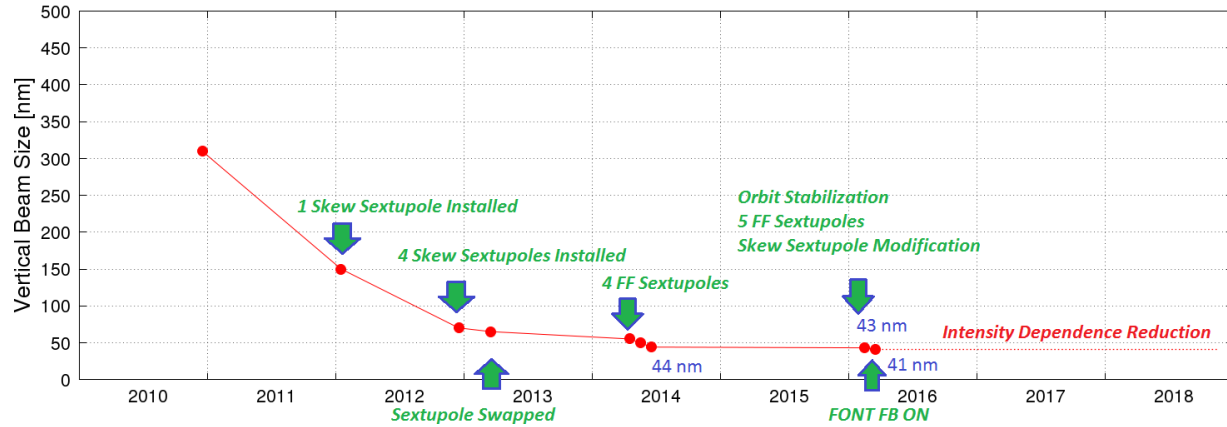


Figure 4.14: Beamsizes achieved at the Accelerator Test Facility 2 (ATF2) as a function of time [75]. The latest result (41 nm [71]) is within 10% of the goal beam size of 37 nm.

exchange of the detectors within approximately 24 hours.

In the push–pull scheme, the innermost final focus quadrupole “QD0”, a slim, superconducting magnet package combined with a sextupole for local chromaticity correction, is installed within the detectors. The other part of the final focus doublet (“QF1”) is located outside the detector on a bridge, and does not move with the detector. Since the TDR, the free space  $L^*$  between interaction point and the QD0 edge has been harmonised to a common value of  $L^* = 3.5$  m [16], which facilitates the design of a final focus optics that delivers optimal and equal performance to both detectors.

The detectors are located in an underground cavern. In contrast to the TDR design, it is foreseen to have a large vertical access shaft [17], which permits a CMS–style detector installation concept, in which the detectors are assembled in large modules in a surface hall and lowered into the hall by means of a gantry crane capable of lowering pieces up to 4000 t. As the CMS experience shows, this concept significantly reduces the schedule risk associated with the experimental hall, since the cavern needs to be available for detector installation only one or two years prior to commissioning.

**Main dump:** The main beam dumps [4, Sect. 8.8] are rated for a maximum beam power of 17 MW [19], enough for a 1 TeV upgrade of the accelerator. The main dump design is based on the successful SLAC 2.2 MW beam dump [76]. It utilises water at 10 bar pressure (to prevent boiling) as absorber medium. The main engineering challenges lie in the safe recombination of the produced oxyhydrogen gas and in the safe containment and disposal of radioisotopes, in particular tritium and  $^7\text{Be}$  produced from spallation processes. The entry window is another component that has to be carefully designed.

**Measurement of beam energy, luminosity, and beam polarisation:** Two energy spectrometers, one located 700 m upstream of the IP, the other 55 m downstream, provide independent

and complementary measurements of the beam energy with an accuracy of 100 ppm [77].

The luminosity is measured to  $10^{-3}$  accuracy from low angle Bhabha scattering in the so-called LumiCal (see Sect. 6.3.1) at polar angles from 30 to 90 mrad. Additional calorimeters (BeamCal) in the region 5 to 30 mrad provide a fast signal that is sensitive to the beam sizes and offsets of the colliding beam, and that can thus be used for their tuning, as part of an intra-beam feedback system (see Sec. 4.1.3).

Beam polarisation is measured with 0.25 % accuracy by means of Compton scattering: electrons that scatter off green or infrared light laser photons lose enough energy that they can be detected in a spectrometer; their momentum spectrum is used to fit the beam polarisation [78]. Two such polarimeters are located 1800 m upstream and 150 m downstream of the IP, which allows to interpolate the precise polarisation at the IP and control the systematics, including effects from precession of the polarisation vector by transverse fields and depolarising effects in the interaction, which lead to a sizeable variation of the polarisation within the bunch during the collision (see Sect. ??).

#### 4.1.4 Upgrade options

Given the high initial investment for a facility as large as the ILC, it is mandatory to have an interesting physics programme for several decades, with the possibility to adapt the programme to the needs arising from the knowledge obtained by the LHC, the ILC itself, all other particle physics experiments, and other domains of physics such as cosmology. Several options exist for upgrades of the ILC in terms of energy, luminosity, and beam polarisation.

##### Energy upgrade

The obvious advantage of a linear collider is its upgradeability in energy. Basically, the main linacs can be extended as far as desired, at constant cost per added beam energy, with some added cost for the relocation of the turn arounds and bunch compressors. Additional costs arise when the beam delivery system (BDS), including the beam dumps, has to be extended to handle the increased beam energy. The current ILC BDS is designed to be easily upgradeable for centre of mass energies up to 1 TeV at minimal cost.

Depending on the actual gradient achieved for the construction of the ILC, up to 171 cryomodules could be installed in addition to those needed to reach 250 GeV, which would increase the centre-of-mass energy by about 54 GeV to around 304 GeV, as Fig. 4.13 shows, and possibly require the installation of two additional cryo plants.

A further energy upgrade would require extension of the tunnel. The Kitakami site can accommodate a total accelerator length of at least 50 km, more than enough for a 1 TeV centre-of-mass energy. Any extension of the accelerator would proceed by adding new cryomodules at the low energy (upstream) ends of the accelerator. There is no need to move modules already installed.

An upgrade would likely proceed in two phases: a preparation phase while the accelerator is

still operated and produces data, and a refurbishment phase where the accelerator is shut down.

During the preparation phase, the necessary components—in particular the cryomodules, klystrons, and modulators—would be acquired and built. At the same time, civil engineering would proceed with the excavation of new access tunnels, underground halls, and the main tunnel. Recent studies conducted during road tunnel construction in the Kitakami area, in the same rock formation as foreseen for the ILC, indicate that the level of vibrations caused by tunnelling activities would allow to bring the new tunnels quite close to the existing ones before machine operation would be affected [79], minimising the shutdown time necessary.

During the installation phase, the newly built tunnels would be connected to the existing ones, the beam lines at the turn-around and the wiggler sections of the bunch compressors would be dismantled, and the new cryomodules would be installed as well as the new turn-around and bunch compressors. At the same time, any necessary modifications to the positron source and the final focus can be made. With the cryomodules ready for installation at the beginning of the shut down period, it is estimated that the shutdown could be limited to about a year for an energy upgrade.

### Luminosity upgrade

The luminosity of the ILC can be increased by increasing the luminosity per bunch (or per bunch charge), or increasing the number of bunches per second [80].

Increasing the luminosity per bunch requires a smaller vertical beam spot size, which may be achieved by tighter focusing and/or smaller beam emittance. Studies indicate that with enough operating experience, there is potential for a further luminosity increase. This route to increased luminosity is, however, invariably linked to higher beam disruption, which brings a risk of a luminosity loss due to mis-steering the beam. Thus, a very accurate feedback system is required.

The ILC design also has the potential to increase the number of colliding bunches per second, by doubling the number of bunches per pulse, and possibly by increasing the pulse repetition frequency.

Doubling the number of bunches per pulse to 2625 would require a smaller bunch spacing, requiring the installation of 50 % more klystrons and modulators. Since the RF pulse length of 1.65 ms is unchanged, the cryogenic load is essentially unchanged. Doubling the number of bunches would double the beam current in the damping rings. For the positron damping ring, this may surpass the limitations from electron cloud (EC) instabilities. To mitigate this risk, the damping ring tunnel is large enough to house a third damping ring, so that the positron current could be distributed over two rings.

The pulse repetition rate (5 Hz in the baseline configuration) is limited by the available cryogenic capacity, the damping time in the damping rings, and the target heat load in the positron source target. The damping rings are designed for a 100 ms damping time and thus capable of a repetition rate of up to 10 Hz, twice the nominal rate. Operation at an increased repetition rate would be possible if after an energy upgrade the machine is operated below its maximum energy (e.g., 250 GeV operation of a 500 GeV machine for a larger low-energy data set), or if additional cryogenic capacity is installed.

## Polarisation upgrade

The baseline design foresees at least 80% electron polarisation at the IP, combined with 30% positron polarisation for the undulator positron source. At beam energies above 125 GeV, the undulator photon flux increases rapidly. Photon polarisation is maximal at zero emission angle; it is decreased and even inverted at larger angles. Thus, collimating the surplus photon flux at larger emission angles increases the net polarisation. Studies indicate that 60% positron polarisation at the IP may be possible at 500 GeV centre-of-mass energy with the addition of a photon collimator.

### 4.1.5 Civil engineering and site

In 2014, the ILC Strategy Council announced the result of its candidate site evaluation for the best possible ILC site in Japan [81]. The evaluation was conducted by a number of Japanese experts from universities and industry, and reviewed by an international committee. It considered technical as well as socio-environmental aspects, and concluded that the candidate site in the Kitakami region is best suited for the ILC.

The site (Fig. 4.15) is located in the Japan's northern Tohoku region, not far from Sendai with its international airport, in the prefectures of Iwate and Miyagi. The closest cities are Ichinoseki, Oshu, and Kitakami, which all offer Shinkansen (bullet train) access to Sendai and Tokyo. The closest harbour is in the city of Kesen-Numa. The coastal region in this area was severely hit by the great Tohoku earthquake in 2011. Both prefectures are supportive of the ILC project and view it as an important part of their strategy to recover from the earthquake disaster.

The Kitakami site was largely selected because of its excellent geological condition. The proposed ILC trajectory lies in two large, homogeneous granite formations, the Hitokabe granite in the north and Senmaya granite to the south. The site provides up to 50 km of space, enough for a possible 1 TeV upgrade or more, depending on the achievable accelerating gradient. Extensive geological surveys have been conducted in the area, including boring, seismic measurements, and electrical measurements [83], as shown in Fig. 4.16. The surveys show that the rock is of good quality, with no active seismic faults in the area.

Earthquakes are frequent throughout Japan, and the accelerator and detectors need proper supports that isolate them from vibrations during earthquakes and micro tremors [84]. Proven technologies exist to cope with all seismic events, including magnitude 9 earthquakes such as the great Tohoku earthquake.

Vibration measurements taken during the construction of a road tunnel show that accelerator operation would be possible during the excavation of a tunnel for an energy upgrade [85].

### 4.1.6 Cost and schedule

For the Technical Design Report, the construction cost of the ILC accelerator was carefully evaluated from a detailed, bottom-up, WBS (Work Breakdown Structure)-based cost estimation [4, Sect. 15]. The TDR estimate distinguishes two cost categories: Value accounts for materials and



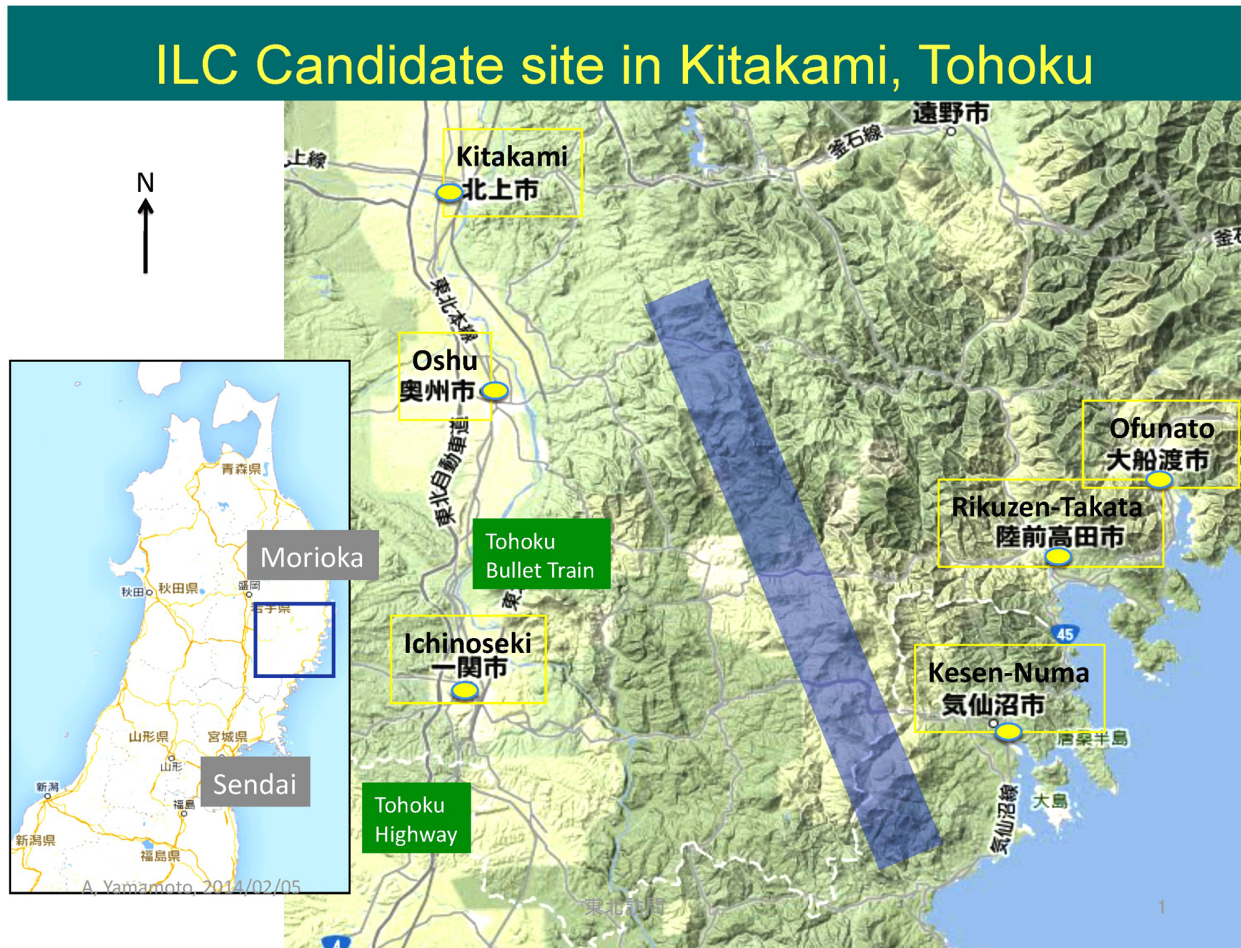


Figure 4.15: The Kitakami candidate site for the ILC [82].

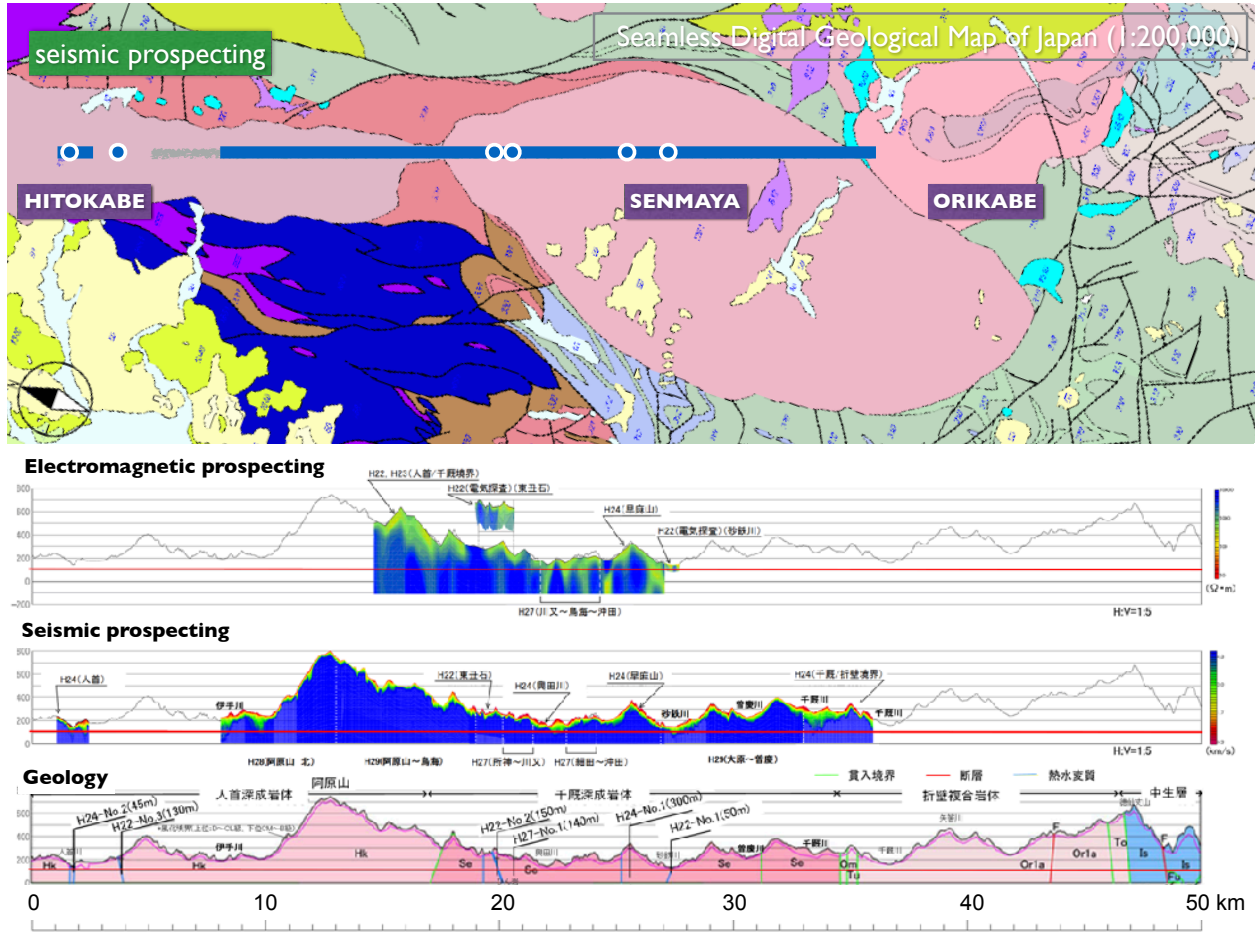


Figure 4.16: Geological situation at the Kitakami site.



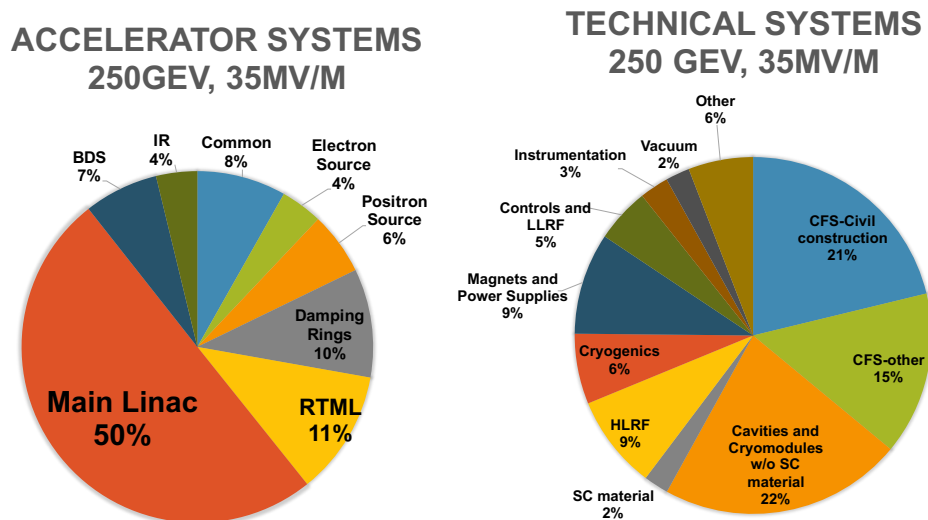


Figure 4.17: Breakdown of Value costs into accelerator systems (left) and technical systems (right) for the 250 GeV ILC accelerator, assuming that cost reduction measures are successful and a gradient of 35 MV/m can be reached.

supplies procured from industry and is given in ILCU (ILC Currency Unit, where 1 ILCU = 1 US\$ in 2012 prices), and Labour accounts for work performed in the participating institutions and is given in person–hours or person–years<sup>3</sup>.

The Value of acquired goods reflects its worth in the local currency of the purchasing institution. Therefore, conversion of Value between currencies is performed based on Purchasing Power Parities (PPP), which are regularly evaluated and published by the OECD [86, 87], rather than currency exchange rates. The PPP values reflect local price levels and thus depend on the type of goods and the country, but fluctuate significantly less than currency exchange rates. Therefore, conversions from ILCU to other currencies cannot not be made on the basis of exchange rates to the U.S. dollar, but on PPP values.

The TDR estimate covers the cost of the accelerator construction, assumed to last 9 years plus one year of commissioning. It includes the cost for the fabrication, procurement, testing, installation, and commissioning of the whole accelerator, its components, and the tunnels, buildings *etc.*, and the operation of a central laboratory at the site over the construction period. It does not, however, cover costs during the preparation phase preceding the start of construction work (“ground breaking”), such as design work, land acquisition, infrastructure (roads, electricity, water) for the site.

Based on the TDR cost estimate, an updated cost estimate was produced for the 250 GeV accelerator. This updated cost estimate includes the cumulative effect of the changes to the design since the TDR (see Sect. 4.1.1), and evaluates the cost for the reduced machine by applying appropriate

<sup>3</sup>One person–year corresponds to 1700 working hours.

scaling factors to the individual cost contributions of the TDR cost estimate.

The resulting Value estimate for the ILC accelerator at 250 GeV is 4,780 – 5,260 MILCU [9] in 2012 prices, where the lower number assumes a cavity gradient of 35 MV/m, while the higher number is based on the TDR number of 31.5 MV/m. In addition, 17,165 kh (thousand person-hours) are required of institutional Labour.

In 2018, the ILC Advisory Panel of the Japanese Ministry of Education, Culture, Sports, Science and Technoloy (MEXT) concluded its review of the ILC [88]. For this review, costs were evaluated in Japanese Yen in 2017 prices, taking into account the local inflation for goods and construction costs. For the purpose of this estimate, also the Labour costs were converted to Yen to yield 119.8 G¥, resulting in a total range of the accelerator construction cost of 635.0 – 702.8 G¥, where the range covers uncertainties in the civil construction costs (18 G¥) and of the gradient (49.8 G¥). For the this estimate, conversion rates of 1 US\$ = 100 JP¥ and 1 € = 1.15 US\$ were assumed.

Operation costs of the accelerator and the central laboratory are estimated to be 36.6 – 39.2 G¥ (about 318 – 341 M€) per year.

## 4.2 ILC Staging up to 1 TeV

[6 pages; corresponding editor: Alex Aryshev (alar@post.kek.jp)]

[ this section should include a table of accelerator parameters at the various stages for easy reference]

## 4.3 ILC Scope Beyond 1 TeV

[5 pages; corresponding editor: Hasan Padamsee (hsp3@cornell.edu)]

The ability to operate the ILC accelerator beyond 1 TeV depends on the possibility of incorporating SCRF cavity with accelerating gradients much higher than the ILC standard 31.5 MeV/m. In this section, we report on the progress toward higher-gradient SCRF and the implications for higher-energy operation of the ILC.

### 4.3.1 Gradient status for the ILC baseline 250 GeV

Figure 4.18 shows the steady progress in single and multicell cavity gradients [89] over the last 3+ decades coming from high purity, high RRR Nb, electropolishing, 800 C furnace treatment for H removal, 100 atm. high pressure water rinsing for removal of field emission particulates, and final baking at 120 C for removal of the high field Q-slope. These procedures establish a standard ILC cavity preparation and treatment recipe from which cavity gradients of 35 MV/m are expected, as observed from the EXFEL production run. More than 40 “best” cavities from the EXFEL production run showed 40–45 MV/m [90], as shown in Fig. 4.19. At DESY, two large grain 9-cell

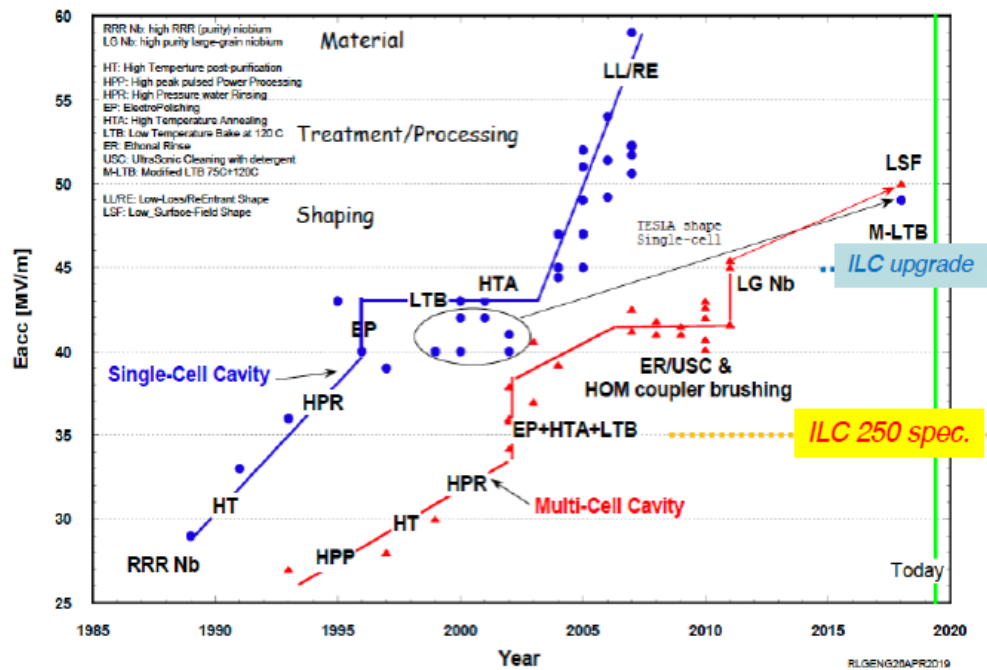


Figure 4.18: Steady progress in single and multi-cell cavity gradients over 3+ decades [89].

cavities reached 45 MV/m [91].

Key areas of further development over the last 5 years have been for higher  $Q$  values at medium gradients (16–22 MV/m) for CW operation with the invention of new techniques of Nitrogen doping [92, 93]. Nitrogen doping for high  $Q$  has already been applied to the construction of a large (4–8 GeV) new accelerator, LCLS-II, and its high energy upgrade LCLS-II-HE. For LCLS-II-HE, ten 1.3 GHz 9-cell N-doped cavities have reached average  $3.5 \times 10^{10}$  at 25.7 MV/m.

Further improvements can be expected from exciting development [94] that show  $Q = 5 \times 10^{10}$  at 30 MV/m by baking at 300 C (mid-T baking) to dissolve the natural oxide (and other surface layers) into the bulk, but not exposing the cavity to air or water before RF measurements. It is interesting to note how the  $Q$  rises with field, as seen for N-doping. After exposure to air, followed by HPR, the  $Q$  dropped to  $2 \times 10^{10}$  at 30 MV/m. Surface analysis of similarly treated samples show a Nitrogen peak at a few nm below the surface, suggesting that N is present at the surface and has diffused into the Nb to give the doping effect. IHEP in China followed up on these encouraging results with several 9-cell TESLA cavities with exciting results [95], as shown in Fig. 4.20(a). After mid-T (300 C) furnace bake, and HPR, all the 9-cell cavities demonstrate high  $Q$  in the range of  $3.5$ – $4.4 \times 10^{10}$  at the gradient between 16–24 MV/m, as shown in Fig. 4.20(b). These cavities have all exceeded the specification of LCLS-II HE ( $2.7 \times 10^{10}$  at 21MV/m). KEK is also pursuing the mid-T baking option. Although in its early stages, the mid-T baking procedure shows the potential of Nb for high gradients with high  $Q$ s.

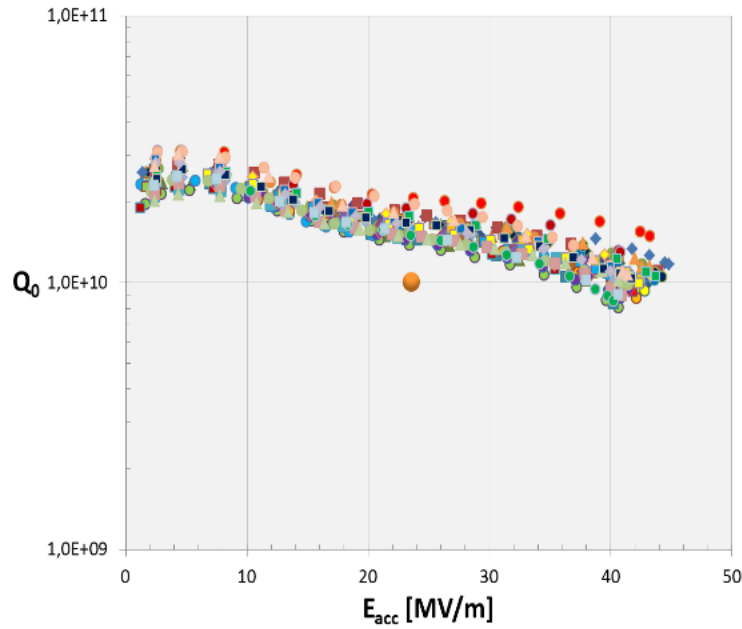


Figure 4.19: 9-cell test results from DESY on  $> 40$  cavities produced and treated by Research Instruments (RI) [90].

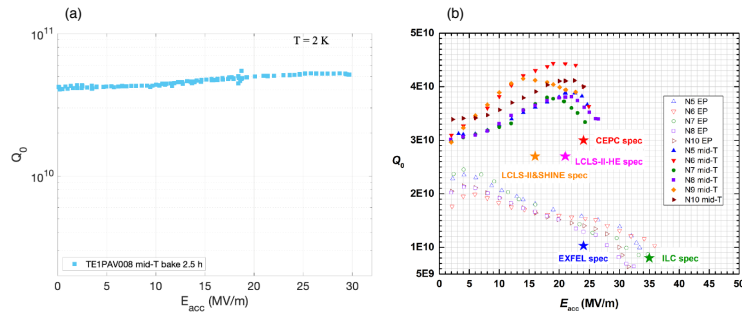


Figure 4.20: (a)  $Q = 5 \times 10^{10}$  at 30 MV/m by baking at 300 C to dissolve the natural oxide (and other surface layers) into the bulk, but not exposing the cavity to air or water before RF measurements. (b) IHEP (China) results on mid-T baking for 9-cell cavities compared to results on the same cavities with the standard ILC treatment [95].

### 4.3.2 High Gradient (45 MV/m) SRF for Upgrade Paths to 1 TeV

Section 4.2 discusses ILC energy upgrade paths from 250 GeV to 380 GeV (Top Factory), 500 GeV and 1000 GeV. For the 1000 GeV upgrade (Scenario B), the 2013 ILC TDR uses a gradient of 45 MV/m with  $Q_0 = 2 \times 10^{10}$  for the additional linac from 500 GeV to 1000 GeV. The SRF parameters are chosen on the forward-looking assumptions of advances in SRF technology derived from R&D which will continue in parallel to both construction and operation of ILC 250 GeV to 1000 GeV. Such extrapolations in SRF performance are reasonably based on expectations from proof-of-principle results already in hand. As discussed further below, single cell cavities with improved treatment reach 49 MV/m, and single cell cavities with improved shapes that reach 52–59 MV/m.

#### Nitrogen Infusion

On the high gradient frontier (with higher Q's), the invention of Nitrogen infusion [96], stemming from Nitrogen-doping, demonstrates gradients of 40–45 MV/m as shown in Fig. 4.21, and compared to the performance of cavities prepared with the standard ILC recipe. JLAB has shown success with infusion [97], but KEK [98] and DESY [99] have found the technique to be sensitive to the quality of the infusion furnace, and difficult to implement.

#### Two-Step Baking and Cold Electropolishing

In another new development, extraordinarily high quench fields for 1.3 GHz niobium TESLA-shaped SRF cavities, some above 50 MV/m have been achieved with the 75/120 C bake surface treatment developed at FNAL, as shown in Figure 5(a). Two-Step baking with Cold Electropolishing [33] show gradients in the range of 40–50 MV/m (average 45 MV/m), as depicted in the histogram Figure 5 (b). Note that 3 cavities that quench below 28 MV/m were found to have physical defects that likely limited the performance.

### 4.3.3 Toward 60 MV/m - Advanced Shape Cavities

Continuing along the gradient frontier, multicell cavities of Re-entrant [100, 101], Low-Los [102] and ICHIRO [103] shapes (Fig. 4.23(b)) have been introduced to lower  $H_{pk}/E_{acc}$  10 - 20% by rounding the equator to expand the surface area of the high magnetic field region, and by allowing  $E_{pk}/E_{acc}$  to rise by about 20%. The Re-entrant shape has an  $\Omega$ -like profile with  $H_{pk}/E_{acc} = 35.4/(\text{MV/m})$ ,  $E_{pk}/E_{acc} = 2.28$  (for 60 mm aperture) as compared to 42.6 Oe/(MV/m) and  $E_{pk}/E_{acc} = 2.0$  for the standard TESLA shape (70 mm aperture). The GR/Q value for the re-entrant shape is about 34% higher than the TESLA shape, which reduces cryogenic losses. The 20% increase in  $E_{pk}$  makes cavities with the new shapes more susceptible to field emission, but we can expect progress in field emission with cleaner surface preparation developments over the coming decades. The motivation in trying the new shape was that quench, governed by  $H_{pk}$ , is a hard limit, whereas field emission, governed by  $E_{pk}$ , can be improved by better engineering. The Low-Loss shape with 60 mm aperture

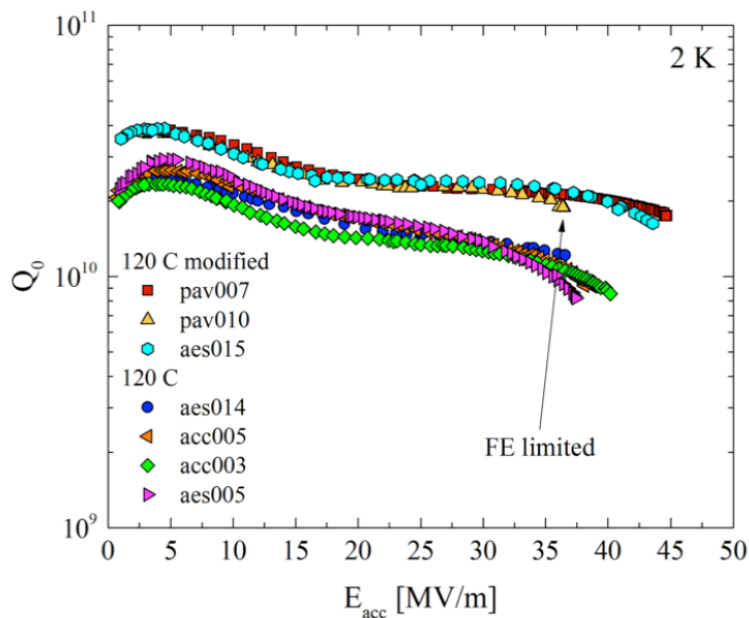


Figure 4.21: Comparison of the performance of several 1-cell cavities from N-infusion with cavities prepared by the standard ILC recipe of EP and 120 C baking.

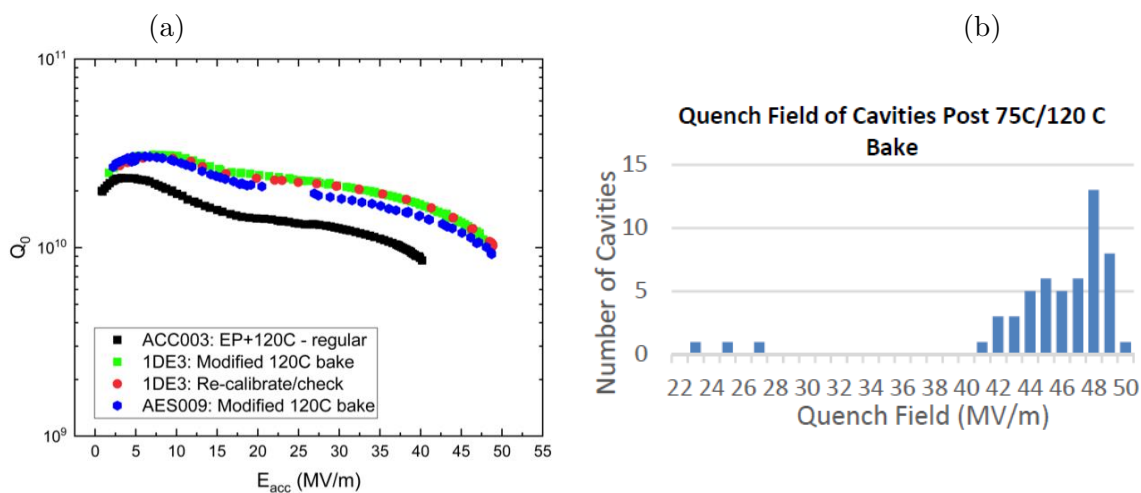


Figure 4.22: (a):  $Q$  vs.  $E$  curve of 1-cell cavity reaching 49 MV/m from Cold EP/optimized baking (75/120 C) compared to the curve of a cavity prepared by the standard ILC recipe. (b) Histogram of gradients of a large number of single cell cavities prepared by Cold EP/optimized baking (75/120 C).

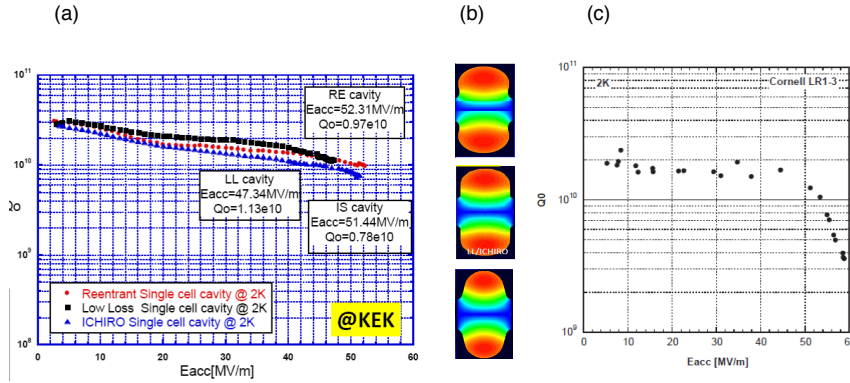


Figure 4.23: (a) Gradients greater than 50 MV/m demonstrated in single cell cavities of various improved shapes. (b) Comparison of Reentrant-top, Low Loss/Ichiro-middle and TESLA-bottom cavity cell shapes, color is magnetic field intensity, red highest, blue lowest. (c) Record gradient near 59 MV/m demonstrated with the re-entrant shape (60 mm aperture).

has  $H_{pk}/E_{acc} = 36.1$  Oe/(MV/m), and  $E_{pk}/E_{acc} = 2.36$ , and a 23% higher GR/Q than the TESLA shape. The ICHIRO shape is a variant of the Low-Loss shape. A relative newcomer to the advanced shape effort is the LSF shape [104] which obtains  $H_{pk}/E_{acc} = 37.1$  Oe/(MV/m) without raising  $E_{pk}/E_{acc}$  ( $= 1.98$ ). It has a small refinement of the Low-Loss shape. Many single cell cavities with the advanced shapes were built, prepared with the standard ILC recipe, and tested to demonstrate gradients of 50 – 54 MV/m with  $Q_0$  values above  $10^{10}$  [105, 31], as shown in Fig. 4.23(a). A record field of 54 MV/m at  $Q$  about  $10^{10}$  was set by a single cell Re-entrant cavity with 60 mm aperture, and 59 MV/m at  $Q$  about  $3 \times 10^9$  (see Fig. 4.23(c) [106]) for the same cavity. However, the best multi-cell cavities of the new shapes have only reached 42 MV/m [107], mostly due to the dominance of field emission. A 5-cell cavity of the LSF shape recently tested at JLAB showed 50 MV/m gradient in three of the five cells [108] by exciting several modes of the fundamental pass-band.

As we have seen earlier, the newly developed, two-step bake procedure has demonstrated a gradient of 49 MV/m in TESLA shape 1-cell cavities. Combining the two-step bake with one of the advanced shape cavities has the potential of improving the gradients toward 60 MV/m. For example, the Low-Loss shape has the potential for 18% improvement from 49 to 58 MV/m. But no laboratory has attempted such combined efforts as yet.

### Cost reduction efforts

The energy upgrades would also benefit from cost saving measures under exploration, such as niobium material cost reduction (15%) for sheet production directly from ingots (with large grains), and/or from seamless cavity manufacturing from tubes using hydroforming, or spinning, instead of the expensive machining and electron beam welding procedures now in practice. Cost-reducing avenues for cryomodules [109] are to connect cryomodules in continuous, long strings similar to



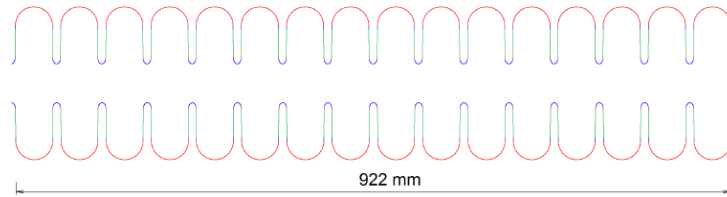


Figure 4.24: A segment of a one-meter TW structure.

cryostats for long strings of superconducting magnets, saving the cost for the expensive ends. The elimination of the external cryogenic transfer line by placing all cryogenic supply and return services in the cryomodule also reduce costs, not only directly for the cryogenic components, but also by reducing tunnel space required. Additional cost reductions and efficiency improvements (not included in the TDR 1 TeV estimate) can be also be expected from improved klystron and modulator technology. In Sec. 4.2, we discuss the ILC upgrade path from 1 TeV to 2 TeV based on gradients/Q of  $55 \text{ MV/m}/2 \times 10^{10}$  obtained by the best new treatments, such as the two-step bake/Cold EP, applied to advanced shape structures, such as the Low-Loss structure, built from Niobium. Section 4.2 provides tables summarizing the main parameters of the 2 TeV ILC upgrade path to be compared to CLIC 1.5 TeV. 70 – 80 MV/m SRF for ILC Upgrade Paths to 3 TeV As discussed in Section 4.3.2 ILC upgrade beyond TDR, we consider the ILC upgrade path from 1 TeV to 3 TeV based on very high gradient SRF opened by R&D underway on two fronts:

1. Optimized travelling wave (TW) superconducting structures [110, 111, 112] with effective gradients up to 70, along with 100% increase in R/Q - which reduces the dynamic heat load by 100%, and
2. 80 MV/m/ $1 \times 10^{10}$  gradient/Q potential for Nb<sub>3</sub>Sn [112] at 4.2 K, based on extrapolations from high power pulsed measurements on single cell Nb<sub>3</sub>Sn cavities.

### TW structures

TW structures offer several main advantages compared to standing wave (SW) structures: substantially lower peak magnetic ( $H_{pk}/E_{acc}$ ), lower peak electric field ( $E_{pk}/E_{acc}$ ) ratios, together with substantially higher R/Q (for lower cryogenic losses). The emphasis for future design is to lower  $H_{pk}/E_{acc}$ , as much as possible, since  $H_{pk}$  presents a hard ultimate limit to the performance of Nb cavities via the critical superheating field. But, as Fig 4.24 shows, the TW structure requires twice the number of cells per meter as for the SW structure in order to provide the proper phase advance (about 105 degrees), as well as a feedback waveguide for redirecting power from the end of the structure back to the front end of accelerating structure, which avoids high peak surface fields in the accelerating cells. The feedback requires careful tuning to compensate reflections along the TW ring to obtain a pure traveling wave regime at the desired frequency.

As discussed in Section 4.3.2, to obtain a luminosity comparable to CLIC 3 TeV, the beam bunch charge for the 3 TeV upgrade can be 3 x lower than the bunch charge for 0.5 TeV. Hence



it is possible to lower the cavity aperture (from 70 mm to 50 mm) without severe penalty in wake-fields to obtain an overall 48% reduction in  $H_{pk}/E_{acc}$ , and factor of 2 gain in R/Q over the TESLA standing wave structure. Accordingly, we examine the impact of 70 MV/m for the 3 TeV ILC upgrade to obtain a luminosity comparable to CLIC 3 TeV. Section 4.2 provides tables summarizing the main parameters of the 70 MV/m ILC upgrade path as compared to CLIC 3 TeV, including capital costs, AC powers, energy spreads and backgrounds at the IP. Modelling and optimization calculations are underway for TW structure optimization [112]. Table 1 shows one set of optimized parameters for optimized cell shape, phase advance, and 50 mm aperture that yield  $H_{pk}/E_{acc} = 28.8$  Oe/(MV/m) with  $E_{pk}/E_{acc} = 1.73$ . Since  $H_{pk}/E_{acc}$  is 42.6 Oe/MV/m and  $E_{pk}/E_{acc} = 2$  for the TESLA structure, the TW structure has reduced the critical parameter  $H_{pk}/E_{acc}$  by 48%! The geometrical parameters for the cell shape are defined in the inset figure accompanying Tab 4.3. If results for the best single cell TESLA shape cavities prepared today ( $E_{acc} = 49$  MV/m,  $H_{pk} = 209$  Oe) can be reached in such a TW structure it will be possible to reach  $E_{acc} = 72.5$  MV/m. The 100% R/Q increase lowers the dynamic heat load and cryogenic power needed for high gradients.

The high group velocity in the TW mode also increases the cell-to-cell coupling from 1.8% for the TESLA structure to 2.3%. Thus TW structures have less sensitivity to cavity detuning errors, making tuning easier, despite the larger number of cells. Studies [112] show that the cell shape can be fine tuned to avoid multipacting, without increasing  $H_{pk}$  more than 1%. HOM damping is under study. Preliminary results show that the first 10 monopole modes up to 7 GHz show no trapping.

Many significant challenges must still be addressed along the TW development path. High circulating power in the feedback waveguide must be demonstrated. Cavity fabrication and surface processing procedures and fixtures must deal with (roughly) double the number of cells per structure.

First structure fabrication and testing efforts have started for TW cavity development [110, 111]. With the relatively easier BCP treatment only, the first single cell TW cavity (Fig. 4.25(a)) with recirculating waveguide achieved 26 MV/m accelerating gradient, limited by the high field Q-slope, as expected for BCP. This result is very encouraging for a first attempt. A 3-cell Nb TW structure with recirculating waveguide (Fig. 4.25(b)) was designed and fabricated but has not yet been tested.

In Sec. 4.2, we consider the ILC upgrade path from 1 TeV to 3 TeV based on 70 MV/m TW Nb cavities to be compared to CLIC 3 TeV. The Section provides tables summarizing the main parameters of the 3 TeV ILC with CLIC 3 TeV.

#### 4.3.4 Nb<sub>3</sub>Sn

A15 compounds are intermetallic and brittle in the bulk form, so SRF structures are produced as a thin layer on the inner surface of an already formed structure. Nb<sub>3</sub>Sn is the most explored compound with the best results [113, 114, 115], but does not as yet give as good performance as with Nb cavities. The A15 phase is in the composition range of 18–25 at% Sn. The superconducting properties  $T_c$ ,  $\Delta$ , and  $H_c$ , depend strongly on the Sn content [116]. Perfect ordering in

Optimization	
Phase advance $\theta$ , deg	
$A$ , mm	
$B$ , mm	
$a$ , mm	
$b$ , mm	
$E_{pk}/E_{acc}$	
$B_{pk}/E_{acc}$ , mT/(MV/m)	
$R_{sh}/Q$ , Ohm/m	
$\alpha$ , degrees	
$l$ , mm	
$R_{eq}$ , mm	
$v_{gr}/c$	
$E_{acc}^*$ , MV/m	
$E_{acc}^* \cdot 2L$ , MV	

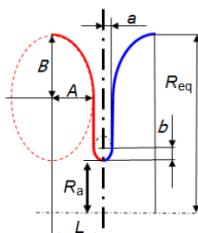


Table 4.3: Parameters of optimized cells with limiting surface fields:  $E_{pk} = 120$  MV/m and  $B_{pk} = 200$  mT, aperture radius  $R_a = 25$  mm.  $E_{acc}$  is the accelerating rate when the limiting surface fields are achieved.  $2L$  is the cell length = 57.55 mm. An 18-cell structure (1.036 m) will have the nearly same active length as the TESLA structure (1.061 m). (from [101], Table 5, column 2).

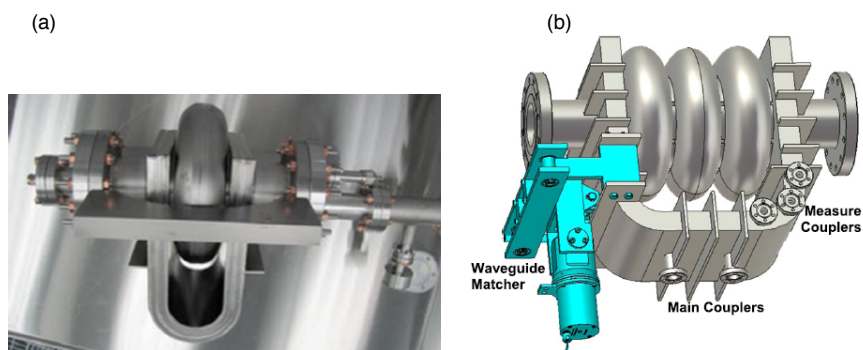


Figure 4.25: (a) 1-cell TW Niobium structure with return waveguide, treated by BCP and tested to reach 26 MV/m. (b) 3-cell TW structure built but not yet tested.

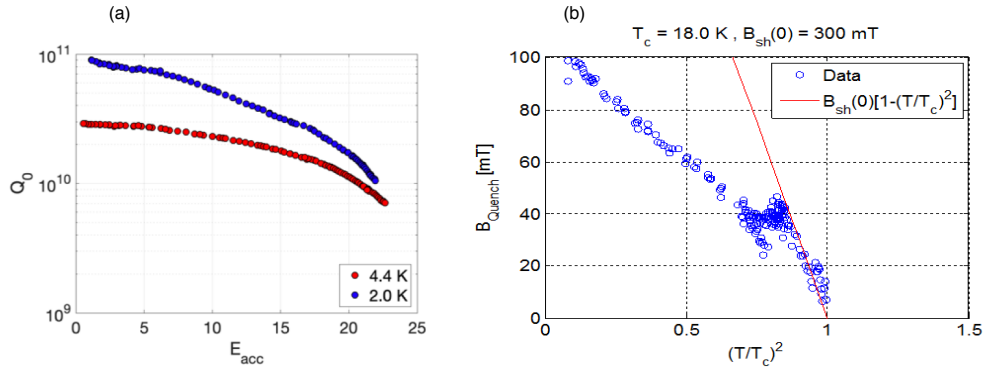


Figure 4.26: (a) Record CW behavior for Nb<sub>3</sub>Sn coated at Fermilab showed  $E_{acc} = 23$  MV/m. (b) Measurements of the critical RF field of Nb<sub>3</sub>Sn using high power pulsed RF. The high temperature results extrapolate to a maximum surface magnetic field of 300 mT, which would translate to  $E_{acc} = 85$  MV/m for a Low-Loss shape cavity.

the stoichiometric phase is achieved close to stoichiometry (at 24.5 at%) where  $H_{sh}$  is 0.42 mT as compared to Nb's  $H_{sh}$  of 0.22 mT at 0 K. Accordingly, we can expect the upper limit of the gradient to be 400 mT or near 95 MV/m.

A few microns thick Nb<sub>3</sub>Sn films can be deposited on the inner surface of Nb cavities exposed to Sn vapor ( $10^{-3}$  mbar) in an UHV furnace at temperatures between 1050 C and 1250 C. In general, the Nb<sub>3</sub>Sn films produced exhibit good material quality with Sn content of about 25%,  $T_c$  from 16 to 18 K,  $\Delta$  from 2.7 to 3.2 meV [117]. Coating results are typically reproducible for the same Nb cavity substrate, but have been seen to vary between different cavities.

Some of the limitations of Nb<sub>3</sub>Sn arise from the sensitivity of the thermodynamic critical field  $H_c$  (and therefore the superheating field) to the exact Sn concentration. For example, a Sn depletion of 3% reduces  $H_c$  by 75%. Other difficulties are the high surface roughness at Nb<sub>3</sub>Sn grain boundaries possibly causing local field enhancement. Somewhat thinner (1  $\mu$ m) layers give smoother surfaces and best results (Fig. 4.26).

Most practitioners of Nb<sub>3</sub>Sn have encountered a Q-slope problem and with gradient limits. Progress has continued. The best case of a flat  $Q$  vs  $E$  curve out to 23 MV/m has been achieved at Fermilab [113, 114, 115] The performance at 4.2 K is also very attractive showing  $Q_0 > 10^{10}$  at gradient of 18 MV/m. Latest films have smaller surface roughness (by a factor of 2), smaller thickness (1  $\mu$ m vs 2-3 $\mu$ m) and smaller grain size (0.7  $\mu$ m vs 1.2  $\mu$ m). Careful material science is yet required to understand and confidently control the Nb<sub>3</sub>Sn crystal growth dynamics so as to produce low-loss surfaces.

High power pulsed RF measurements (Fig. 4.26(b)) at Cornell on a Nb<sub>3</sub>Sn cavity show encouraging trends for very high gradients [113]. At high temperature ( $T \gtrsim 15$  K), the results track the high superheating field, extrapolating to 300 mT ( $E_{acc} \gtrsim 80$  MV/m) at zero temperature. But at lower temperature, thermal limitations take over to limit the highest field to about 100 mT (24MV/m) which is close to the CW result of 22 MV/m.

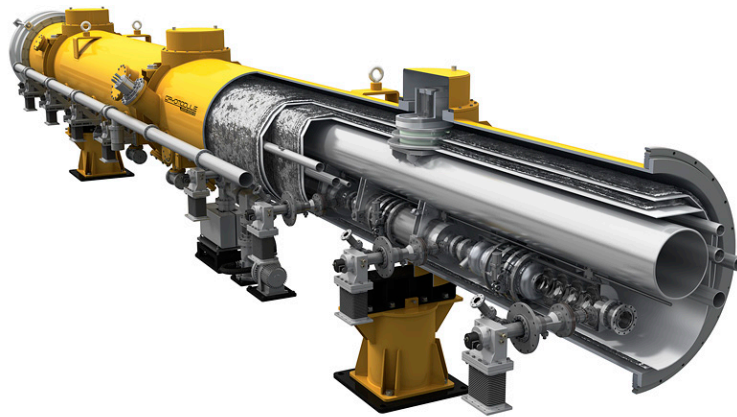


Figure 4.27: Cutaway view of an ILC cryomodule. (Image by Rey Hori [118].)

In Section 4.3.2, ILC upgrade beyond TDR, we consider the ILC upgrade path from 1 TeV to 3 TeV based on Nb<sub>3</sub>Sn cavities with gradients/Q of 80 MV/m/ $1 \times 10^{10}$ . The Section provides Tables summarizing the main parameters of the 3 TeV ILC to be compared to CLIC 3 TeV, and also discusses the potential benefits from 80 MV/m Nb<sub>3</sub>Sn.

## 4.4 Issues for ILC Accelerator R&D

[5 pages; corresponding editor: Shinichiro Michizono (shinichiro.michizono@kek.jp)]

## 4.5 Opportunities for US contributions

[8 pages; corresponding editor: Sam Posen (sposen@fnal.gov)]

US laboratories host world-class infrastructure and expertise in technology that is relevant for particle accelerators. This presents a number of opportunities for the US to make important contributions to the ILC accelerator that leverage existing capabilities. These contributions would help the project to go forward and position the US well for strong participation in ILC-based experiments.

### 4.5.1 Superconducting Linac

The superconducting linear accelerator that drives the ILC requires 1000 cryomodules to reach a center of mass energy of 250 GeV. Each cryomodule (see Fig. 4.27) contains 8  $\sim$ 1 meter long superconducting radiofrequency (SRF) cavities, which generate large amplitude electric fields to accelerate the beam. They also contain liquid-helium-based cryogenics to keep the cavities at 2 K,



Figure 4.28: View of some of the cryomodule assembly facilities at Fermilab (left) and Jefferson Lab (right).

magnets, RF power couplers, frequency tuners, vacuum valves, and instrumentation. US labs have substantial experience with these sophisticated components from US-based accelerator projects including CEBAF, SNS, LCLS-II, and PIP-II. Large scale production facilities exist at Fermilab and at Jefferson Lab for assembling SRF cryomodules (see Fig. 4.28). These facilities include large cleanrooms for making vacuum connections between cavities while minimizing the risk of generating particulates that can cause field emission, large fixtures for connecting cavity strings to cold masses and inserting cold masses into cryomodules, and equipment for welding, RF diagnostics, and coupler assembly. Fermilab and JLab also have existing cryomodule test facilities, which require 2 K refrigerators, dedicated radiation areas, and RF systems. These facilities have very recently been used for the mass production of cryomodules for LCLS-II, for which the cryomodule design was largely based on ILC. As such the production facilities have already been recently tested with a very relevant system, though ILC would require approximately 5 times as many modules to be produced as the entire production of LCLS-II and its high energy upgrade LCLS-II-HE combined. However, the Fermilab and JLab and the teams would take on the larger production with enthusiasm and experience. The vast majority of the infrastructure is already in place, with some modifications required for the higher throughput required to meet the 1 cryomodule per week target for the Americas region at peak production.

In addition to Fermilab and JLab, there are also SRF facilities at Argonne, Cornell, and FRIB, which are less specialized towards production of ILC-like cryomodules, but could be leveraged for example for cavity treatment. SLAC's expertise in high power RF sources could be leveraged for driving the cavities as well as RF distribution. SLAC is also planning a relevant cryomodule test facility that could be used. Berkeley's expertise in low level RF could be leveraged for cavity control, particularly for resonance control at high accelerating gradients.

Fig. 4.28: View of some of the cryomodule assembly facilities at Fermilab (left) and Jefferson Lab (right).

US expertise can also contribute to advanced performance for ILC cryomodules. Since the 2012



TDR, significant progress has been made in SRF R&D, including new procedures developed by researchers from US labs for reaching high gradients. Some of these developments could be implemented in ILC cryomodules to push performance by 10%, either resulting in fewer cryomodules required to reach the design center of mass energy, or else as a safety margin on top of the nominal energy and beginning towards first energy upgrades. The relevant new technologies include cold electropolishing [119] and the two step bake [33].

Advances from US labs can also contribute to some of the auxiliary systems of the cryomodules. The tuner used in LCLS-II was an evolution of previous designs and is well suited to the short beamtubes of the ILC, while maintaining minimal backlash [120]. The quadrupole magnet used in LCLS-II is also an evolution of previous designs, with conduction cooling and a split design to allow it to be assembled outside of the cleanroom [121]. A system and procedure for plasma processing of SRF cavities was developed at ORNL [122] and later adapted to 9-cell cavities by FNAL [123], which may be useful for reducing effects such as field emission in some cases.

US labs are expected to also play a leading role in developing technologies for energy upgrades to the ILC to reach the 380 GeV-1 TeV energy range beyond the baseline ILC and the multi-TeV energy range in the future. This includes SRF R&D, such as development of advanced superconductors including Nb<sub>3</sub>Sn for cavities [124], advanced geometries [111], and a plasma accelerator that leverage the SRF-based ILC baseline system. For more details on these upgrades, see Sec. 15.

### 4.5.2 Electron and Positron Sources

Many US labs have capabilities in sources from their own facilities. The plan for ILC has a polarized positron source, which can be accomplished in different ways. One of these employs superconducting undulators, the other targets, and both subjects have expertise at a number of US labs.

### 4.5.3 Damping Ring, Beam Delivery System, and Beam Dump

US accelerator scientists have extensive experience also in the technologies needed for the damping ring, beam delivery system, and beam dump.

The damping ring is expected to be similar to multiple US facilities, such as the APS upgrade at Argonne, CESR at Cornell, and NSLS-II at Brookhaven.

For beam dynamics and lattice development, researchers at nearly all US labs with accelerators have substantial relevant experience as well as specialized tools and codes such as ACE3P, ELEGANT, and BLAST.

Expertise in superconducting magnets at labs such as FNAL, Berkeley, and BNL can be applied to the magnets needed for the final focus at the interaction point. A similar task is ongoing at US labs for production of magnets for the high luminosity upgrade of the LHC.

For research and development related to plasma-accelerator-based multi-TeV upgrades to ILC, US labs host multiple accelerator facilities that could be used for relevant R&D including AWA at Argonne, FACET at SLAC, ATF at BNL, BELLA at LBL, and FAST at Fermilab.

#### 4.5.4 Summary

The US National Laboratories are anticipating a wide range of contributions to the ILC accelerator. These contributions are synergistic, both from past programs—*i.e.*, they leverage existing infrastructure and expertise in US labs—and for developments for the future—*i.e.*, much of the needed R&D for the US contribution to ILC has application to other accelerator projects that the laboratories are involved in.

By virtue of this, there is a broad interest among all of the US National Laboratories invested in accelerator physics in participating in ILC. In addition to synergies with US labs, there is also synergy with US industry. A substantial part of the US funds for ILC construction will be put towards procurements from US companies for high-tech components that will be used in cryomodules and other accelerator elements.





## Chapter 5

# General Aspects of the ILC Physics Environment

[5 pages; corresponding editors: Daniel Jeans (daniel.jeans@kek.jp), Jenny List (jenny.list@desy.de), Michael Peskin (mpeskin@slac.stanford.edu)]

### 5.1 Key Standard Model Processes

(This section will contain an orientation to the SM processes at the ILC:  $e^+e^-$  annihilation to fermions,  $e^+e^- \rightarrow WW, ZZ$ , multi-particle final state,  $\gamma e$  and  $\gamma\gamma$  reactions. It will give examples of background processes for various interesting reactions, and will emphasize the relative simplicity and well-understood nature of these backgrounds.)

### 5.2 Energy and Luminosity

(This section will describe the energy and luminosity evolution of the ILC, following the plan described in Sec. 4.2.)

### 5.3 Beam Polarization

(This section will give an orientation to the physics of beam polarization at  $e^+e^-$  linear colliders. It will describe the effective polarization in  $e^+e^-$  annihilation and its influence on cross sections and angular distributions. Then it will discuss the use of separate electron and positron polarization to isolate specific physics effects and to control sources of systematic error.)



# Chapter 6

## ILC Detectors

[general corresponding editors: James Brau (jimbrau@uoregon.edu), Jan Strube (jan.strube@pnnl.gov), Maxim Titov (maxim.titov@cea.fr), Andrew White (awhite@uta.edu)]

### 6.1 Detector Requirements for the Physics Program

[4 pages]

### 6.2 The ILD Detector

[8 pages; corresponding editor: Ties Behnke (ties.behnke@desy.de)]

#### 6.2.1 Detector description and capabilities

#### 6.2.2 R&D issues for the ILD design

### 6.3 The SiD Detector

[8 pages; corresponding editor: Andrew White (awhite@uta.edu)]

#### 6.3.1 Detector description and capabilities

The SiD detector concept is a general-purpose experiment designed to perform precision measurements at the ILC. It satisfies the challenging detector requirements resulting from the full range of ILC physics processes. SiD is based on the paradigm of particle flow, an algorithm by which the reconstruction of both charged and neutral particles is accomplished by an optimised combination of

SiDBarrel	Technology	In rad	Out rad	z extent
Vtx detector	Silicon pixels	1.4	6.0	$\pm$ 6.25
Tracker	Silicon strips	21.7	122.1	$\pm$ 152.2
ECAL	Silicon pixels-W	126.5	140.9	$\pm$ 176.5
HCAL	Scint-steel	141.7	249.3	$\pm$ 301.8
Solenoid	5 Tesla SC	259.1	339.2	$\pm$ 298.3
Flux return	Scint-steel	340.2	604.2	$\pm$ 303.3
SiDEndcap	Technology	In z	Out z	Out rad
Vtx detector	Silicon pixels	7.3	83.4	16.6
Tracker	Silicon strips	77.0	164.3	125.5
ECAL	Silicon pixel-W	165.7	180.0	125.0
HCAL	Scint-steel	180.5	302.8	140.2
Flux return	Scint/steel	303.3	567.3	604.2
LumiCal	Silicon-W	155.7	170.0	20.0
BeamCal	Semicond-W	277.5	300.7	13.5

Table 6.1: Key parameters of the baseline SiD design. (All dimension are given in cm).

tracking and calorimetry. The net result is a significantly more precise jet energy measurement than that achieved via conventional methods and which results in a di-jet mass resolution good enough to distinguish between  $W$ s and  $Z$ s. The SiD detector (Fig. 6.1) is a compact detector based on a powerful silicon pixel vertex detector, silicon tracking, silicon-tungsten electromagnetic calorimetry, and highly segmented hadronic calorimetry. SiD also incorporates a high-field solenoid, iron flux return, and a muon identification system. The use of silicon sensors in the vertex, tracking, and calorimetry enables a unique integrated tracking system ideally suited to particle flow.

The choice of silicon detectors for tracking and vertexing ensures that SiD is robust with respect to beam backgrounds or beam loss, provides superior charged particle momentum resolution, and eliminates out-of-time tracks and backgrounds. The main tracking detector and calorimeters are “live” only during a single bunch crossing, so beam-related backgrounds and low-pT backgrounds from  $\gamma\gamma$  processes will be reduced to the minimum possible levels. The SiD calorimetry is optimised for excellent jet energy measurement using the particle flow technique. The complete tracking and calorimeter systems are contained within a superconducting solenoid, which has a 5 T field strength, enabling the overall compact design. The coil is located within a layered iron structure that returns the magnetic flux and is instrumented to allow the identification of muons. All aspects of SiD are the result of intensive and leading-edge research aimed at achieving performance at unprecedented levels. At the same time, the design represents a balance between cost and physics performance. Nevertheless, given advances in technologies it is now appropriate to consider updates to the SiD design as discussed below. First, we describe the baseline SiD design for which the key parameters are listed in Table 6.1.

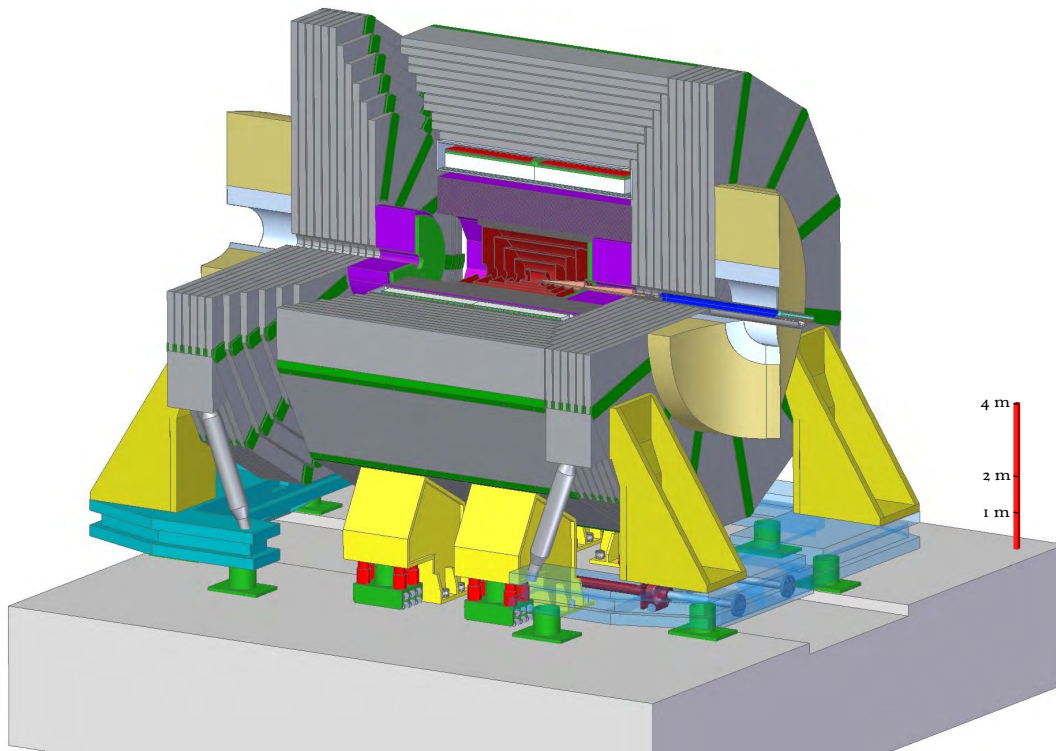


Figure 6.1: The SiD detector concept.

### Silicon-based tracking

The tracking system (Fig. 6.2) is a key element of the SiD detector concept. The particle flow algorithm requires excellent tracking with superb efficiency and two-particle separation. The requirements for precision measurements, in particular in the Higgs sector, place high demands on the momentum resolution at the level of  $\delta(1/p_T) \sim 2 - 5 \times 10^{-5}/\text{GeV}/c$ .

Highly efficient charged particle tracking is achieved using the pixel detector and main tracker to recognise and measure prompt tracks, in conjunction with the ECAL, which can identify short track stubs in its first few layers to catch tracks arising from secondary decays of long-lived particles. With the choice of a 5 T solenoidal magnetic field, in part chosen to control the  $e^+e^-$ -pair background, the design allows for a compact tracker design.

### Vertex detector

To unravel the underlying physics mechanisms of new observed processes, the identification of heavy flavours will play a critical role. One of the main tools for heavy flavour identification is the vertex detector. The physics goals dictate an unprecedented spatial three-dimensional point

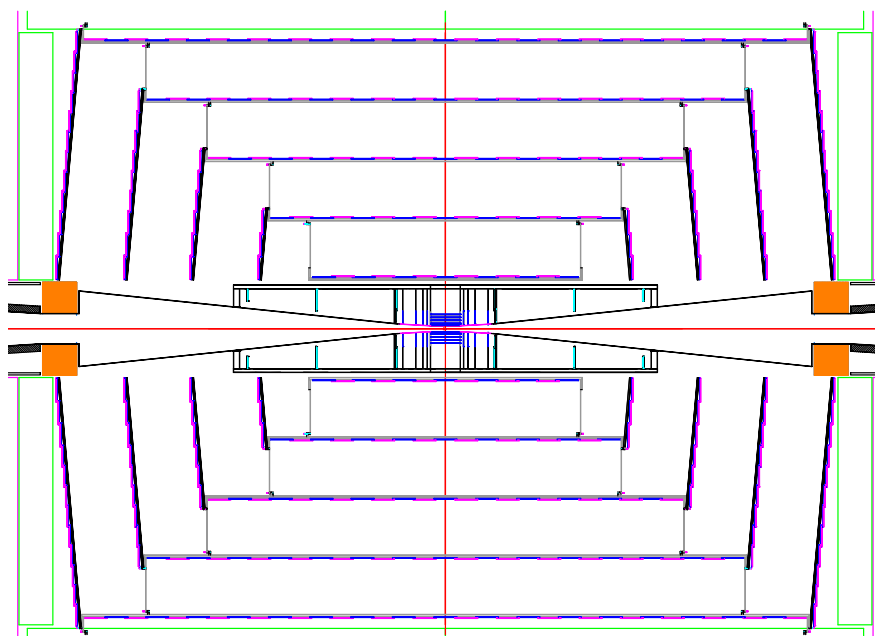


Figure 6.2: r-z view of vertex detector and outer tracker.

resolution and a very low material budget to minimise multiple Coulomb scattering. The running conditions at the ILC impose the readout speed and radiation tolerance. These requirements are normally in tension. High granularity and fast readout compete with each other and tend to increase the power dissipation. Increased power dissipation in turn leads to an increased material budget. The challenges on the vertex detector are considerable and significant R&D is being carried out on both the development of the sensors and the mechanical support. The SiD vertex detector uses a barrel and disk layout. The barrel section consists of five silicon pixel layers with a pixel size of  $20 \times 20 \mu\text{m}^2$ . The forward and backward regions each have four silicon pixel disks. In addition, there are three silicon pixel disks at a larger distance from the interaction point to provide uniform coverage for the transition region between the vertex detector and the outer tracker. This configuration provides for very good hermeticity with uniform coverage and guarantees excellent charged-track pattern recognition capability and impact parameter resolution over the full solid angle. This enhances the capability of the integrated tracking system and, in conjunction with the high magnetic field, makes for a very compact system, thereby minimising the size and costs of the calorimetry.

To provide for a very robust track-finding performance the baseline choice for the vertex detector has a sensor technology that provides time-stamping of each hit with sufficient precision to assign it to a particular bunch crossing. This significantly suppresses backgrounds.

Several vertex detector sensor technologies are being developed. One of these is a monolithic CMOS pixel detector with time-stamping capability (Chronopixel [125]), being developed in collaboration with SRI International. The pixel size is about  $10 \times 10 \mu\text{m}^2$  with a design goal of

99% charged-particle efficiency. The time-stamping feature of the design means each hit is accompanied by a time tag with sufficient precision to assign it to a particular bunch crossing of the ILC – hence the name Chronopixel. This reduces the occupancy to negligible levels, even in the innermost vertex detector layer, yielding a robust vertex detector which operates at background levels significantly in excess of those currently foreseen for the ILC. Chronopixel differs from the similar detectors developed by other groups by its capability to record time stamps for two hits in each pixel while using standard CMOS processing for manufacturing. Following a series of prototypes, the Chronopixel has been proven to be a feasible concept for the ILC. The three prototype versions were fabricated in 2008, in 2012, and in 2014. The main goal of the third prototype was to test possible solutions for a high capacitance problem discovered in prototype 2. The problem was traced to the TSMC 90 nm technology design rules, which led to an unacceptably large value of the sensor diode capacitance. Six different layouts for the prototype 3 sensor diode were tested, and the tests demonstrated that the high capacitance problem was solved.

With prototype 3 proving that a Chronopixel sensor can be successful with all known problems solved, optimal sensor design would be the focus of future tests. The charge collection efficiency for different sensor diode options needs to be measured to determine the option with the best signal-to-noise ratio. Also, sensor efficiency for charged particles with sufficient energy to penetrate the sensor thickness and ceramic package, along with a trigger telescope measurement, needs to be determined. Beyond these fundamental measurements, a prototype of a few  $\text{cm}^2$  with a final readout scheme would test the longer trace readout resistance, capacitance, and crosstalk.

A more challenging approach is the 3D vertical integrated silicon technology, for which a full demonstration is also close.

Minimising the support material is critical to the development of a high-performance vertex detector. An array of low-mass materials such as reticulated foams and silicon-carbide materials are under consideration. An alternative approach that is being pursued very actively is the embedding of thinned, active sensors in ultra low-mass media. This line of R&D explores thinning active silicon devices to such a thickness that the silicon becomes flexible. The devices can then be embedded in, for example, Kapton structures, providing extreme versatility in designing and constructing a vertex detector.

Power delivery must be accomplished without exceeding the material budget and overheating the detector. The vertex detector design relies on power pulsing during bunch trains to minimise heating and uses forced air for cooling.

### **Main tracker**

The main tracker technology of choice is silicon strip sensors arrayed in five nested cylinders in the central region and four disks following a conical surface with an angle of 5 degrees with respect to the normal to the beamline in each of the end regions. The geometry of the endcaps minimises the material budget to enhance forward tracking. The detectors are single-sided silicon sensors, approximately  $10 \times 10 \text{ cm}^2$  with a readout pitch of  $50 \mu\text{m}$ . The endcaps utilise two sensors bonded back-to-back for small angle stereo measurements. With an outer cylinder radius of 1.25 m and a

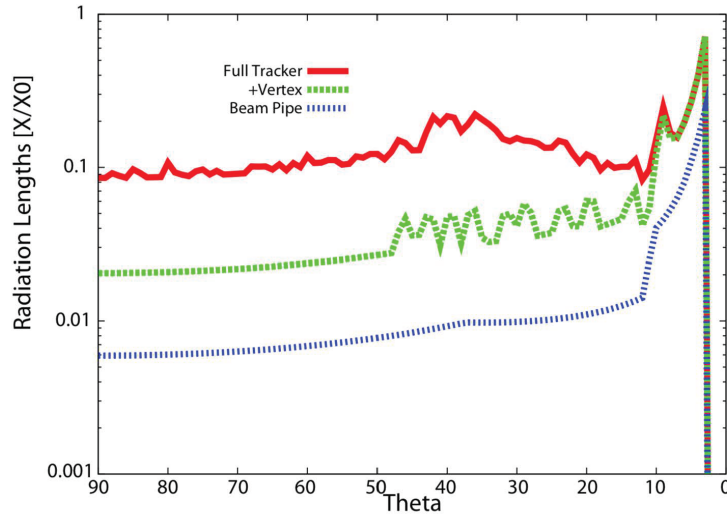


Figure 6.3: Material in the SiD detector, in terms of fractions of a radiation length, as a function of the polar angle.

5 T field, the charged track momentum resolution will be better than  $\delta(1/p_T) = 5 \times 10^{-5}/(\text{GeV}/c)$  for high momentum tracks with coverage down to polar angles of 10 degrees. A plot of the material budget as a function of polar angle is shown in Fig. 6.3.

The all-silicon tracking approach has been extensively tested using full Monte-Carlo simulations including full beam backgrounds. Besides having an excellent momentum resolution it provides robust pattern recognition even in the presence of backgrounds and has a real safety margin, if the machine backgrounds will be worse than expected.

### Main calorimeters

The SiD baseline design incorporates the elements needed to successfully implement the PFA approach. This imposes a number of basic requirements on the calorimetry. The central calorimeter system must be contained within the solenoid in order to reliably associate tracks to energy deposits. The electromagnetic and hadronic sections must have imaging capabilities that allow both efficient track-following and correct assignment of energy clusters to tracks. These requirements imply that the calorimeters must be finely segmented both longitudinally and transversely. In order to ensure that no significant amount of energy can escape detection, the calorimetry must extend down to small angles with respect to the beam pipe and must be sufficiently deep to prevent significant energy leakage. Since the average penetration depth of a hadronic shower grows with its energy, the calorimeter system must be designed for the highest-energy collisions envisaged.

In order to ease detector construction the calorimeter mechanical design consists of a series of modules of manageable size and weight. The boundaries between modules are kept as small as possible to prevent significant non-instrumented regions. The detectors are designed to have



excellent long-term stability and reliability, since access during the data-taking period will be extremely limited, if not impossible.

The combined ECAL and HCAL systems consist of a central barrel part and two endcaps, nested inside the barrel. The entire barrel system is contained within the volume of the cylindrical superconducting solenoid.

SiD's reliance on particle flow calorimetry to obtain a jet energy resolution of  $\sim 3\%$  demands a highly segmented (longitudinally and laterally) electromagnetic calorimeter. It also calls for a minimized lateral electromagnetic shower size, by minimizing the Moliere radius to efficiently separate photons, electrons and charged hadrons [?].

The SiD ECal design employs thirty longitudinal layers, the first twenty each with 2.50 mm tungsten alloy thickness and 1.25 mm readout gaps, and the last ten with 5.00 mm tungsten alloy. The total depth is 26 radiation lengths, providing good containment of electromagnetic showers.

Simulations have shown the energy resolution for electrons or photons to be well described by  $0.17 / \sqrt{E} \oplus 0.009$ , degrading a bit at higher energies due to changes in sampling fraction and a small leakage.

The baseline design employs tiled, large, commercially produced silicon sensors (currently assuming 15 cm wafers). The sensors are segmented into pixels that are individually read out over the full range of charge depositions. The complete electronics for the pixels is contained in a single chip, the KPiX ASIC [126], which is bump bonded to the wafer. The low beam-crossing duty cycle ( $10^{-3}$ ) allows reducing the heat load using power pulsing, thus allowing passive thermal management within the ECal modules.

Bench tests of the KPiX bonded sensor with a cosmic ray telescope trigger yielded a Landau distribution with a peak of the signal at about 4 fC is consistent with our expectation for minimum-ionizing particles (MIP) passing through the fully-depleted 320  $\mu\text{m}$  thick sensors. Crosstalk between channels has been managed and the noise distribution shows an RMS of 0.2 fC, well below the 4 fC MIP signal, and exceeding the ECal requirement.

The overall mechanical structure of the ECal barrel has been designed for minimal uninstrumented gaps. Input power and signals are delivered with Kapton flex cables. The KPiX chip has an average power less than 20 mW, resulting in a total heat load that is managed with a cold plate and water pipes routed into the calorimeter.

A first SiD ECal prototype stack of nine (of thirty) layers has been constructed and was exposed to a 12.1 GeV electron beam at the SLAC End Station Test Beam Facility. This data collection demonstrated good measurements of multiple particle overlap and reconstruction of overlapping showers [127]. Comparison of the deposited energy distribution in each of the nine layers also agrees well with simulations. An algorithm developed to count the number of incident electrons in each event was used to assess the ability of the calorimeter to separate two showers as a function of the separation of the showers, achieving 100% for separations of  $>10$  mm.

The hadronic calorimeter has a depth of 4.5 nuclear interaction lengths, consisting of alternating steel plates and active layers. The baseline choice for the active layers is scintillator tiles read out via

silicon photomultipliers. For this approach SiD is closely following the analog hadron calorimeter developments within the CALICE collaboration. In this context, the simulated HCAL energy resolution has been shown to reproduce well the results from the CALICE AHCAL prototype module exposed to pion beams.

### Forward calorimeters

Two special calorimeters are foreseen in the very forward region: LumiCal for a precise luminosity measurement, and BeamCal for the fast estimation of the collision parameters and tagging of forward-scattered beam particles. LumiCal and BeamCal are both compact cylindrical electromagnetic calorimeters centered on the outgoing beam, making use of semiconductor-tungsten technology. BeamCal is placed just in front of the final focus quadrupole and LumiCal is aligned with the electromagnetic calorimeter endcap.

LumiCal makes use of conventional silicon diode sensor readout. It is a precision device with challenging requirements on the mechanics and position control, and must achieve a small Moliere radius to reach its precision targets. Substantial work has been done to thin the silicon sensor readout planes within the silicon-tungsten assembly. Dedicated electronics with an appropriately large dynamic range is under development.

BeamCal is exposed to a large flux of low-energy electron-positron pairs originating from beamstrahlung. These depositions, useful for a bunch-by-bunch luminosity estimate and the determination of beam parameters, require radiation hard sensors. The BeamCal has to cope with 100% occupancies, requiring dedicated front-end electronics. A challenge for BeamCal is to identify sensors that will tolerate over one MGy of ionizing radiation per year. Sensor technologies under consideration include polycrystalline chemical vapor deposition (CVD) diamond (too expensive to be used for the full coverage), GaAs, SiC, Sapphire, and conventional silicon diode sensors. The radiation tolerance of all of these sensor technologies has been studied in a high-intensity electron beam.

For SiD, the main activities are the study of these radiation-hard sensors, development of the first version of the so-called Beam readout chip, and the simulation of BeamCal tagging for physics studies. SiD coordinates these activities through its participation in the FCAL R&D Collaboration.

### Magnet coil

The SiD superconducting solenoid is based on the CMS solenoid design philosophy and construction techniques, using a slightly modified CMS conductor as its baseline design. Superconducting strand count in the coextruded Rutherford cable was increased from 32 to 40 to accommodate the higher 5 T central field.

Many iron flux return configurations have been simulated in two dimensions so as to reduce the fringe field. An Opera 3D calculation with the Detector Integrated Dipole (DID) coil has been completed. Calculations of magnetic field with a 3D ANSYS program are in progress. These will have the capability to calculate forces and stress on the DID as well as run transient cases to check

the viability of using the DID as a quench propagator for the solenoid. Field and force calculations with an iron endcap HCAL were studied. The field homogeneity improvement was found to be insufficient to pursue this option.

Conceptual DID construction and assembly methods have been studied. The solenoid electrical power system, including a water-cooled dump resistor and grounding, was established. Significant work has been expended on examining different conductor stabiliser options and conductor fabrication methods. This work is pursued as a cost- and time-saving effort for solenoid construction.

### **Muon system**

The flux-return yoke is instrumented with position sensitive detectors to serve as both a muon filter and a tail catcher. The total area to be instrumented is very significant – several thousand square meters. Technologies that lend themselves to low-cost large-area detectors are therefore under investigation. Particles arriving at the muon system have seen large amounts of material in the calorimeters and encounter significant multiple scattering inside the iron. Spatial resolution of a few centimetres is therefore sufficient. Occupancies are low, so strip detectors are possible. The SiD baseline design uses scintillator technology, with RPCs as an alternative. The scintillator technology uses extruded scintillator readout with wavelength shifting fibre and SiPMs, and has been successfully demonstrated. Simulation studies have shown that nine or more layers of sensitive detectors yield adequate energy measurements and good muon detection efficiency and purity. The flux-return yoke itself has been optimised with respect to the uniformity of the central solenoidal field, the external fringe field, and ease of the iron assembly. This was achieved by separating the barrel and end sections of the yoke along a 30 degree line.

### **The machine-detector interface**

A time-efficient implementation of the push-pull model of operation sets specific requirements and challenges for many detector and machine systems, in particular the interaction region (IR) magnets, the cryogenics, the alignment system, the beamline shielding, the detector design and the overall integration. The minimal functional requirements and interface specifications for the push-pull IR have been successfully developed and published [128, 129]. All further IR design work on both the detectors and machine sides are constrained by these specifications.

#### **6.3.2 R&D issues for the SiD design**

## **6.4 New Technologies for ILC Detectors**

(We hope that any group developing a new technology potentially useful at ILC will contribute to the appropriate subsection below. Please send a summary of your work (hopefully citing a Snowmass contributed paper) to the corresponding editors of this chapter.)

[10 pages]

**6.4.1 Tracking**

**6.4.2 Calorimetry**

**6.4.3 Vertex Detector**

**6.4.4 Forward Detectors**

**6.4.5 Muon System**

**6.4.6 Timing Elements**

# Chapter 7

## ILC Detector Simulation

[5 pages; corresponding editor: Frank Gaede (frank.gaede@desy.de)]

### 7.1 ILC Fast Simulation Frameworks

(This section will describe the ILC fast simulation frameworks used for SiD, ILC, and Snowmass projects; see [8].)

### 7.2 ILCSOFT Framework

(This section will describe the ILCSOFT Framework used for full-simulation studies of ILC experiments.)

### 7.3 ILC SM Background Samples

(This section will describe the method of generation of SM event samples for ILC studies.)



## Chapter 8

# ILC Physics Measurements at 250 GeV

[15 pages; general corresponding editors: Daniel Jeans (daniel.jeans@kek.jp), Jenny List (jenny.list@desy.de), Michael Peskin (mpeskin@slac.stanford.edu)]

(This chapter will review experimental studies of the various ILC reactions available at 250 GeV. The ILD group is now preparing a new high-statistics sample of 250 GeV events. Thus, we expect new analyses of many of these processes to be ready for Snowmass, in particular, a new analysis of  $e^+e^- \rightarrow W^+W^-$  at 250 GeV.)

### 8.1 Higgs – Conventional Decays

[corresponding editor: Daniel Jeans (daniel.jeans@kek.jp)]

#### 8.1.1 Hadronic decays

flavor tagging: b, c, s?, gluon.

#### 8.1.2 Leptonic decays

taus & muons.

#### 8.1.3 EW-bosonic decays

WW, ZZ, Z-gamma, gamma-gamma

## 8.2 Higgs – Exotic Decays

[corresponding editor: Zhen Liu (zliuphys@umd.edu)]

Higgs exotic decays provide unique opportunities to probe a broad class of new physics models [130]. Studying the Higgs exotic decay precision would help reveal new physics, especially hidden sector dynamics through this generic Higgs portal. The physics we can learn from the Higgs exotic decay program is also complementary to the Higgs coupling precision measurements. An survey of lepton collider sensitivities to Higgs exotic decays into final states that are challenging at hadron colliders has been initially carried out in Ref. [131], showing the promising sensitivities at lepton colliders. Many new and interesting channels remain open for assessment. In the following, we discuss a few channels that can be studied within the timeline of the Snowmass process and also merit journal publications.

- Higgs exotic decays of  $H \rightarrow XX \rightarrow 4f$  where the intermediate resonant particle  $X$  mass is below 10 GeV. This scenario is particularly motivated by recent discussion about Higgs exotic decay connections to strongly first order electroweak phase transition [132, 133]. In this region, the particle  $X$  can also be easily long-lived, we can consider to extend the study into long-lived particle regime [134].
- Higgs decay into dark shower, where the showered hidden mesons<sup>1</sup> can either decay promptly or long-lived, and their decay channel back to the SM can be either hadronic or leptonic. The phenomenological study for this class of models are basically widely open due to the challenges of trigger and background at the LHC. The process is motivated by generic considerations of hidden sector strong dynamics. A more familiar example is the discussion of neutral naturalness [136], but on the other hand, the current studies have been focusing on the Higgs decays into a pair of twin glueballs [137, 138, 134, 139], which is only a subclass of the generic Higgs decays into these final states. Furthermore, this dark shower channel is also motivated by variance of the class of models with large number of light scalar embedded, e.g., NNaturalness [140], EW scale as a trigger [141], electroweak symmetry delayed- or non-restoration [142, 143, 144, 145], etc.

## 8.3 $W$ Boson

[corresponding editor: Jenny List (jenny.list@desy.de)]

## 8.4 4-Fermion Processes

[corresponding editor: Taikan Suehara (suehara@phys.kyushu-u.ac.jp)]

---

<sup>1</sup>It can also be fermions, for instance, composite neutrinos [135].



## 8.5 Precision QCD

[corresponding editor: Ian Moulton (imoulton@slac.stanford.edu)]

(This section will describe not only the precision measurement of  $\alpha_s$  from jets at ILC, but also new observables sensitive to jet substructure and other detailed features of QCD. See, for example, [146, 147],)

## 8.6 Dark Sector

[corresponding editor: Maxim Perelstein (m.perelstein@cornell.edu)]

(This section will describe dark sector searches in  $e^+e^- \rightarrow \gamma + X$  and related processes at 250 GeV. More dark sector material appears in Sec. 8.2 above and in Chap. 10 and 11.)



## Chapter 9

# ILC Precision Electroweak Measurements

[5 pages; corresponding editors: Graham Wilson (gwwilson@ku.edu), Roman Pöschl (poeschl@lal.in2p3.fr)]

### 9.1 Radiative Return to the $Z$

### 9.2 $Z$ Pole Program

### 9.3 $W$ and $Z$ Boson Masses



## Chapter 10

# ILC Physics Measurements at 350, 500, and 1000 GeV

[15 pages; general corresponding editors: Daniel Jeans (daniel.jeans@kek.jp), Jenny List (jenny.list@desy.de), Michael Peskin (mpeskin@slac.stanford.edu)]

### 10.1 Top Quark

[corresponding editors: Roman Pöschl (poeschl@lal.in2p3.fr), Frank Simon (fsimon@mpp.mpg.de), Marcel Vos (vos@ific.uv.es)]

#### 10.1.1 Top Quark Mass

The top quark mass is one of the fundamental parameters of the Standard Model that must be determined experimentally.

**Brief intro of interpretation**

### **10.1.2 Current state of the art and (HL-) LHC prospects**

**Threshold scan**

**Direct measurement**

**Radiative events at  $\sqrt{s} = 500\text{-}600$  GeV**

### **10.1.3 Top Quark Electroweak Couplings**

**Relevance of EW couplings**

**State of the art and HL-LHC prospects**

**ILC prospects for top EW couplings**

**EFT - Hand over to section 13.5**

## **10.2 Higgs**

### **10.2.1 WW fusion**

[corresponding editor: Daniel Jeans (daniel.jeans@kek.jp)]

The WW fusion process becomes the dominant source of Higgs production at energies about around 400 GeV. It thereby provides higher-precision measurements of Higgs properties, even if the "recoil" methods used to analyse Higgs-strahlung are not applicable here.

Since the process involves the H-W-W coupling, it is particularly sensitive to potential non-SM properties of this vertex.

### **10.2.2 Higgs Self-Coupling**

[corresponding editor: Jenny List (jenny.list@desy.de) ]

### **10.2.3 Top Quark Yukawa Coupling**

[corresponding editor: Marcel Vos (vos@ific.uv.es) ]

**Brief discussion of relevance, state of the art, and HL-LHC prospects**

**Potential of the ILC, direct vs. indirect**

**Optimization of the high-energy operating scenario**

### **10.3 *W* Boson**

[corresponding editor: Jenny List (jenny.list@desy.de)]

### **10.4 4-Fermion Processes**

[corresponding editor: Taikan Suehara (suehara@phys.kyushu-u.ac.jp) ]

### **10.5 New Particle Searches – TeV Scale**

[corresponding editor: Mikael Berggren (mikael.berggren@desy.de)]

### **10.6 New Particle Searches – Dark Sector**

[corresponding editor: Maxim Perelstein (m.perelstein@cornell.edu)]





# Chapter 11

## ILC Fixed-Target Program

[7 pages; corresponding editor: Stefania Gori (sgori@ucsc.edu)]

In addition to its central collider, the ILC accelerator can host a number of additional detectors, including detectors for fixed-target experiments and beam dump experiments and remote detectors observing collider events. These can provide the setting for a multi-faceted program. The main purpose of these experiments will be to search for dark sector particles interacting only feebly with the Standard Model, as motivated by many dark matter models, as well as by models addressing the baryon-anti baryon asymmetry problem, the strong CP problem, and the hierarchy problem. The intense and high-energy electron and positron beams that the ILC makes available also have uses in nuclear and hadron physics and in studies of strong-field QED. They can also provide resources for developing advanced electron and positron accelerators.

Dark sector particles could communicate with the SM in a number of ways, via a dark photon  $A'_\mu$  interacting through the gauge portal  $\epsilon A'_{\mu\nu} F^{\mu\nu}$ , via a dark scalar interacting through the Higgs portal  $\kappa |S|^2 |H|^2$ , through a dark fermion interaction through the neutrino portal,  $yNLH$ , or through a pseudo-Goldstone boson interacting through the axion portal  $(a\Lambda)F_{\mu\nu}\tilde{F}^{\mu\nu}$ . We have already described ILC probes of these interactions in Chapter 8 and 10. But all of the portals can also be explored powerfully in the fixed-target program, using a variety of different experimental approaches.

In this chapter, we will present the variety of fixed-target and remote experiments that could be mounted at the ILC site and estimate their potential both for dark sector searches and for other issues.

### 11.1 ILC Facilities for Fixed-Target Experiments

A tour of the ILC design, with possible locations of fixed-target and remote detectors, was given by Kaoru Yokoya at the LCWS 2021 [<https://indico.cern.ch/event/995633/>]. A fully developed plan will be given in this section.

## 11.2 Beam-Dump Experiments

Dark sector particles could be produced from the interactions of either the  $e^-$  or the  $e^+$  beam with the corresponding beam dump. These particles could be long-lived enough to decay back to SM particles after the beam dump. They could be probed by detectors located 50–100 m away from the beam dump and behind the muon shield, searching for visible decay products (e.g. signatures involving two or more leptons, or two or more photons). In this section, we will compare the discovery prospects of dark particles either at a  $e^-$  or at a  $e^+$  ILC beam dump experiment.

Dark sector particles could also be produced from Higgs exotic decays. In fact, the combination of the very narrow width of the SM Higgs boson, and the facility of the Higgs to couple to New Physics makes Higgs exotic decays one of the best ways to test dark sector particles. If long-lived enough, the dark particle could be detected at a detector searching for decays of LLPs produced at the interaction point (IP) placed 50-200 m from the IP. In this section, we will discuss the corresponding discovery prospects and compare them to the detection prospects at other experiments, including the main ILC experiments.

## 11.3 Dedicated Secondary-Beam Experiments

It is feasible to extract the electron beam upstream of the IP at times outside of the collider program. This could provide, for example, an electron beam of more than double the energy and about  $10^3$  higher intensity compared to the SLAC experiments of the 1990's. There are many interesting applications for such a beam, which we will explore in this section and the next. At a lower intensity, this beam could also provide, a missing-momentum experiment a la LDMX. In this setup, the electron beam is passed through a thin target, which is surrounded on both sides by tracking material. The energy and momentum of individual beam particles are measured on both sides of the target, unveiling the possible production of an invisible dark particle.

## 11.4 Nuclear and Hadron Physics with Electron and Positron Beams

## 11.5 ILC as an Accelerator Test-Bed

[corresponding editor: Kaoru Yokoya (kaoru.yokoya@kek.jp)]

# Chapter 12

## Precision Tests of the Standard Model

[12 pages; corresponding editors: Junping Tian (tian@icepp.s.u-tokyo.ac.jp), Christophe Grojean (christophe.grojean@desy.de), Michael Peskin (mpeskin@slac.stanford.edu)]

### 12.1 Precision Standard Model Theory for ILC

[corresponding editor: Ayres Freitas (afreitas@pitt.edu)]

To achieve the goals described in sections 8 and 9, precise predictions for the Standard Model (SM) expectations of the relevant observables are needed. A detailed discussion of the required theory work for studies at  $\sqrt{s} \approx 91$  GeV, 160 GeV and 250 GeV can be found in Ref. [148] and references therein. The necessary improvement can be split into three categories:

- Fixed-order calculations: For the  $Z$ -pole program, electroweak N<sup>3</sup>LO corrections as well as leading N<sup>4</sup>LO corrections for the effective  $Z$ -fermion vertices are needed. Here “leading” refers to corrections enhanced by powers of the top Yukawa coupling and/or QCD strong coupling. For the 250-GeV program and physics at the  $WW$  threshold, NNLO electroweak corrections for  $2 \rightarrow 2$  scattering processes are mandatory. In addition, calculations of Higgs decay amplitudes must be completed to NNLO order, in particular, for the Higgs decay  $H \rightarrow 4f$ . Higher-order QCD corrections to  $H \rightarrow gg$  and  $H \rightarrow b\bar{b}$  are also needed.
- To study effects of detector acceptance and background subtraction, Monte-Carlo tools need to be created with the precision of the expected measurements. This requires an accurate treatment of multi-photon initial state radiation and awareness of beam polarization. Furthermore, the Monte-Carlo programs must be matched to the fixed-order calculations discussed in the previous bullet point. Beyond the leading order QCD and electroweak corrections must be merged in an appropriate way. For a more detailed discussion of QED effects, see Ref. [149].
- Theoretical predictions for the precision observables within the SM also require a range of SM parameters as inputs, most notably the top and bottom quark mass,  $m_{t,b}$ , the strong

coupling  $\alpha_s$ , and the running electromagnetic coupling at the weak scale,  $\alpha(M_Z)$ .  $m_t$  can be measured with high precision at the ILC, but its extraction from the data required resummed higher-order QCD corrections computed in an effective field theory framework. More precise determinations of  $m_b$ ,  $\alpha_s$  and  $\alpha(M_Z)$  may be possible with improved lattice QCD calculations.

Instead of running on the  $Z$ -pole, ILC can also produce high-precision measurements of  $Z$ -boson properties by using the radiative return method at  $\sqrt{s} = 250$  GeV, as described in section 9.1. A detailed study of the theoretical needs for this program is still lacking. It will require the evaluation of multiple emissions of collinear initial state photons, see e.g. Ref. [150], as well as full SM corrections to the process  $e^+e^- \rightarrow \gamma Z$ . A closer look at the required theory calculations and tools within the Snowmass process would be highly desirable.

## 12.2 Frameworks for Effective Field Theory

(This section will discuss the theoretical issues for the interpretation of ILC measurements using Effective Field Theory. In the ILC literature, global fits are done using SMEFT with dimension-6 operators only. There are alternative frameworks. What model-dependence does this choice bring in? Can invisible and exotic Higgs decays be included in these global fits? These issues will be discussed in some detail at Snowmass, and we hope to incorporate insights from that discussion.)

## 12.3 Expectations from a Unified SMEFT Analysis

(This section will apply various SMEFT frameworks to the LHC+ILC data set, explain how the SMEFT coefficients are determined, and discuss the difference between these approaches.)

## 12.4 Expectations for CP-Violating Operators

(This section will include the inclusion of CP-violating operators within the context of SMEFT. What processes constrain the coefficients of these operators. How much redundancy is there in the ILC determinations?)

## 12.5 Expectations for Heavy-Quark Operators

(The list of dimension-6 SMEFT operators expands greatly when operators that specifically involve heavy-quark fields are included. This section will discuss the relation more standard form-factor descriptions of BSM corrections to top quark properties to a full SMEFT analysis. What experiments are required to resolve all of the ambiguities?)

## Chapter 13

# Big Physics Questions Addressed by ILC

[10 pages; corresponding editors: Nathaniel Craig (ncraig@physics.ucsb.edu), Mihoko Nojiri (mihoko.nojiri@kek.jp), Maxim Perelstein (m.perelstein@cornell.edu), Michael Peskin (mpeskin@slac.stanford.edu)]

The discovery of the 125 GeV Higgs boson poses even more questions that it answers. Within the SM, the Higgs boson explains the the origin of all particle masses through the Higgs mechanism. The 125 GeV boson seems to fulfill this role, but still there remain many questions both about this boson and about the SM itself. Is this boson solely responsible for the breaking of electroweak symmetry and the generation of mass? Is it a singleton, or is it merely the first of several Higgs bosons? What sets the mass parameter for this boson? Can we explain electroweak symmetry breaking in physical terms, with a theory in which that mass is computable? If the SM is correct up to very high scales and the its parameters are equal to the current central values, the vacuum we see is unstable. Is this the true situation, and, either way, what is the true behavior of the vacuum of the universe far in the future? In addition, the discovery of the Higgs boson sharpens questions that have been asked since the SM was first formulated. What is the origin of flavor and the fermion generations? Why is there more matter than antimatter? What is the nature of dark matter? What other types of new matter exist in nature?

Through its comprehensive set of precision measurements of the couplings of the 125 GeV Higgs boson, and through its larger program of measurements of electroweak reactions at the weak-interaction scale, the ILC has the power to give insight into all of these questions. In this chapter, we will outline these questions in more detail and describe their relation to ILC measurements. In the next chapter, we will illustrate the insights from the ILC in a complementary way, through quantitative comparison of the ILC projected measurements with the predictions of models of physics beyond the SM.

### 13.1 Can the Standard Model be exact to very high energies?

At TeV energies, the Higgs field quartic coupling increases with energy due to renormalization-group running. However, it is prediction of the SM that this coupling turns over and begins to decrease at very high energies. For the current central values of SM parameters, the Higgs quartic coupling becomes negative at about  $10^{11}$  GeV, leading to a vacuum instability, assuming that the SM is still exact at those energies. Within the SM, the outcome depends sensitively on the values of the Higgs boson mass and the top quark mass, to a degree that we do not know today what the SM actually predicts for our universe. Precision measurements of these two quantities to the accuracies projected for the ILC will resolve this. If the SM is modified, our vacuum state can still be stable or unstable, depending on details of the model that we hope to learn.

- Stability diagram in the plane of self-coupling and top yukawa
- Implications of ILC measurements in the stability diagram. **To Do:** Update with the latest ILC projections available
- Impact of new physics at intermediate scales, relation to ILC measurements? **To Do:** Would be interesting to find an explicit example of new physics, invisible at the LHC but visible at the ILC, that changes Higgs quartic running enough to flip stable/unstable. An SM-singlet at a few hundred GeV with  $O(1)$  coupling to Higgs?
- Supersymmetry dramatically changes the running of the Higgs self-coupling and the physics of vacuum stability. Some aspects of this are probed by the Higgs coupling to  $b\bar{b}$ . Maybe we can say "Even more interestingly, the vacuum maybe stabilized by symmetry. " On the other hand, supersymmetry can also de-stabilize the vacuum.

### 13.2 Why is there more matter than antimatter?

The origin of matter is no less compelling a mystery than the origin of mass. Assuming inflationary cosmology, the universe began in a state with equal amounts of matter and antimatter. From this starting point, the abundance of matter over anti-matter can be explained starting from symmetric initial conditions if some epoch in the early universe satisfies the Sakharov conditions— $B$  violation,  $C$  and  $CP$  violation, and loss of thermal equilibrium. These ingredients seem suggestively present in the quark sector of the Standard Model itself, but, quantitatively, too small an asymmetry is generated. It is possible to generate the observed baryon asymmetry in simple extensions of the Standard Model. These must include new sources of  $CP$  violation and dynamics that takes the universe out of thermal equilibrium such as a first-order phase transition or late-decaying particles. Models in which the out-of-equilibrium events take place below the TeV scale can be directly tested at the ILC. A prominent class of models is that in which the electroweak transition itself becomes first-order due to the coupling of the Higgs boson to other new particles. Another interesting class of model involves dark sector particles or heavy neutrinos that would be revealed at the ILC.

- Electroweak baryogenesis and Higgs coupling deviations. Use Higgs+singlet model as an example of ILC capabilities beyond LHC. **To Do:** Make a plot:  $hZZ$  and  $h^3$  coupling deviations needed for first-order PT vs. ILC sensitivity. MN: should we focus on  $\sqrt{s} = 250$  GeV or as large as 1TeV?
- CPV in Higgs couplings MN:  $h \rightarrow \tau^+\tau^-$  any update from D. Jeans LCWS 2016?  $hVV$  T Ogawa EPS 2017. Ge et al 2012.13922. Not much collider study but 2003.00099 Fuchs for b, t CP violation as well. ask plot from them?
- WIMPy baryogenesis and direct searches?
- MN: Leptogenesis? Collider implications of leptogenesis with 5-50 GeV heavy neutrinos is studied in 1710.03744

### 13.3 What is the dark matter of the universe?

Perhaps the most compelling evidence for physics beyond the Standard Model comes from the sky, with a host of concordant observations indicating that baryons comprise only a fraction of the matter in the universe. Although viable dark matter candidates span many decades in mass, the near-coincidence of dark matter and baryon abundances suggests a non-gravitational mechanism to connect the two. This singles out dark matter candidates at or below the weak scale that interact with the Standard Model through one of several possible portals. We have discussed in Chapters 8, 10, and 11 that these models often have special difficulties for the discovery of new particles at hadron colliders, difficulties that can be overcome at the ILC.

- Minimal (electroweak) dark matter. **To Do:** Use plots from Jenny and Co for the ILC. Update direct detection comparisons, include new DM-electron scattering searches such as SENSEI which are sensitive to the same operator.
- Higgs portal dark matter. **To Do:** (1) Higgs invisible decay constraints on HPDM assuming direct  $H \rightarrow 2$  DM decay. (2) Rare Higgs decays, e.g.  $H \rightarrow 4b$ , in dark sector models connected to asymmetric DM. Need ILC studies of rare Higgs decays. MN:  $H \rightarrow 4b$  is also studied in the context of EWPT context by Kozacuk et al., 1911.10210 .
- Dark photons. **To Do:** Make ILC reach plots for visibly and invisibly decaying dark photons. **MN: a lesson is that we may need to discuss particular process in next section because a single channel can have different implication.**

### 13.4 What is the energy scale of new physics?

The Higgs boson is an exquisitely sensitive barometer for new physics, with any deviation in its properties providing a smoking gun indication of new physics. (MN: Actually, the quantities constrained by gauge symmetry is, but for the case of Higgs boson, such constraints does not exist

at low energy side. We can say the Higgs sector is not yet constrained and we can have new physics there. Is this what you mean by "exquisitely"? ) If new physics enters at or above the weak scale, these deviations can be systematically captured in effective field theory extensions of the Standard Model that encode the energy scale of new physics. In this section we interpret the EFT projections of section 12 in terms of motivated scenarios for new physics, translating ILC precision into qualitative lessons about the nature of the Higgs boson, its potential, and its coupling to other Standard Model particles. (MN: So precision test of the SM comes before this section.... ) We further explore the broad lessons that may be extracted from potential Higgs coupling deviations in different EFT frameworks, including tests of the bedrock principles of quantum field theory via positivity constraints and the implications of deviations that are poorly fit by SMEFT.

- Interpretation of SMEFT parameters and fit.
- Complementarity with / relation to flavor constraints.
- Tests of bedrock principles of QFT (analyticity, unitarity) through positivity bounds at the ILC. (not sure about this....)
- HEFT vs. SMEFT? Scenarios in which ILC data must necessarily be interpreted in terms of HEFT rather than SMEFT. (MN: ref. arXiv:2008.08597. there is a toy model but not sure aif aany full model exists. )

### 13.5 Why is electroweak symmetry broken?

The mass of the Higgs doublet is the unique dimensionful parameter of the Standard Model Lagrangian and sets the value of the weak scale. The sensitivity of the Higgs mass parameter to short-distance physics raises the question of why this scale is so widely separated from the apparent scale of quantum gravity, a puzzle often referred to as the hierarchy problem. More immediately, the sign of the Higgs mass parameter is unfixed in the Standard Model, leaving the mystery of why electroweak symmetry is broken in the first place. These questions can be addressed in extensions of the Standard Model that reduce the ultraviolet sensitivity of the Higgs mass parameter and potentially explain the sign of the mass-squared as a consequence of universal phenomena. Such extensions predict the appearance of new particles near the weak scale that can be directly produced at the ILC or sensed indirectly through their impact on the properties of the Higgs. Weakly-coupled examples, such as supersymmetry, allow a precise mapping between the Higgs mass, its couplings, and the spectrum of new particles.

Alternately, the lightness of the Higgs boson may be explained by strong coupling, in analogy with confinement in QCD. The separation in scale between the Higgs and additional composite states can be understood if the Higgs doublet is itself a goldstone of a spontaneously broken global symmetry, much like the pions and kaons of QCD. Such Composite Higgs models (both in four dimensions and higher, holographically) predict significant deviations in Higgs couplings as well as new states potentially accessible at the ILC. Even at strong coupling, these models give rise to distinctive correlations between the Higgs mass, its couplings, and the spectrum of new particles.



- Superpartner searches. **To Do:** Show an example where the ILC can discover a superpartner invisible at the LHC - Higgsinos? MN: arXiv: 1912.06643 Baer et al.
- Extended Higgs models, e.g. 2HDM, appear in many solutions of the hierarchy problem. **To Do:** Find a good plot to illustrate ILC capabilities for 2HDM.
- Little Higgs **To Do:** Ask Juergen for a plot showing ILC top/Higgs coupling measurement indirect sensitivity to LH. Highlight the importance of top coupling measurements!
- Composite Higgs
- Model Discrimination. If signs of new physics are found, high precision of ILC measurements allow to figure out the right model even if the relevant new particles are beyond the kinematic reach. **To Do:** Use an example from Michael and Co SMEFT fit papers.



## Chapter 14

# ILC Probes of the Big Questions

[8 pages; corresponding editors: Nathaniel Craig (ncraig@physics.ucsb.edu), Mihoko Nojiri (mihoko.nojiri@kek.jp), Maxim Perelstein (m.perelstein@cornell.edu), Michael Peskin (mpeskin@slac.stanford.edu)]

**14.1 Higgs boson: tests for violation of the Standard Model**

**14.2 Higgs boson: the Higgs Inverse Problem**

**14.3 Electroweak sector**

**14.4 Top Quark**



## Chapter 15

# Long-Term Future of the ILC Laboratory

[general corresponding editor: Michael Peskin (mpeskin@slac.stanford.edu)]

### 15.1 Future Accelerators in the ILC Tunnel

#### 15.1.1 Very High Gradient Superconducting RF

[5 pages; corresponding editor: Hasan Padamsee (hsp3@cornell.edu)]

[ maybe a couple of pages of reminder are needed, depending on the content of section 4.3]

#### 15.1.2 Very High Gradient Copper Accelerators

[corresponding editor: Emilio Nanni (nanni@slac.stanford.edu)]

#### 15.1.3 Plasma, Laser, and Structure Wakefield Accelerators

[5 pages; corresponding editor: Spencer Gessner (sgess@slac.stanford.edu) ]

#### Beam-Driven Plasma Linear Collider

[1 page; corresponding author: Spencer Gessner (sgess@slac.stanford.edu) ]

## ILC Upgrade to multi-TeV using Laser Wakefield Accelerators

[1 page; corresponding authors: C. Schroeder, C. Geddes, E. Esarey (LBNL)]

Laser wakefield accelerators (LWFAs) [151] rely on an intense, ultrashort laser pulses to resonantly excite large amplitude electron plasma waves with relativistic phase velocities. The accelerating fields of the plasma wave, or wakefields, are 1-10 GV/m, orders of magnitude larger than conventional accelerating structures, enabling compact acceleration of charged particle beams. LWFA technology provides an opportunity to upgrade the ILC to higher beam energy using the planned ILC main linac tunnel, site power, and infrastructure. An LWFA-based linac arm would consist of multiple plasma stages, each stage yielding a few GeV/stage energy gain, driven by a multi-J, short pulse laser [152, 153]. Laser drivers are highly flexible, and plasma mirror technology enables compact coupling of the laser driver into the plasma accelerating cells. The multi-Joule-class laser systems, potentially based on fiber laser combination, occupy an area of a few m<sup>2</sup> and both the drive lasers and plasma accelerating stages may be placed in the ILC Main Linac tunnel. LWFAs accelerate short bunches, of order 10 micron, and the resulting beamstrahlung reduction at the IP yields significant power savings for a given target luminosity. To reach  $E_{CM} = 1$  TeV, an LWFA-based linac requires potentially only 0.2 km in each linac arm, and 100 MW of power for both beams to reach a luminosity of  $10^{34}$  cm<sup>-2</sup>s<sup>-1</sup>. This could be upgraded to  $E_{CM} = 3$  TeV with luminosity of  $10^{35}$  cm<sup>-2</sup>s<sup>-1</sup>, requiring a 0.65 km LWFA linac in each linac arm and 300 MW of power for both beams. The LWFA beam power for 1 TeV and 3 TeV would be 4 MW and 12 MW, respectively, and are within the power rating of the planned ILC beam dump. The unused main linac tunnel length could be employed to extend the BDS system to accommodate  $E_{CM} = 3$  TeV, as well as space for linear cooling sections to further reduce the beam emittance. The bunch structure employed is one bunch each 20  $\mu$ s, and additional bunch compressors would be required to achieve the short, 10-micron-scale, bunch length. Furthermore, achieving high beam energies ( $E_{CM} > 3$  TeV) is straightforward by adding additional LWFA stages, although the required increased luminosity would require site power beyond the planned ILC design. This provides a long-term upgrade path to continue realizing new physics reach in realistic stages using the infrastructure of a linear collider. Significant R&D is required to realize an LWFA-based linac, and, in particular, further development of high average power, short-pulse laser systems operating at tens of kHz repetition rates [154].

## Structure Wakefield Accelerators

John Power (ANL), Chunguang Jing (ANL, Euclid) and Philippe Piot (ANL, NIU):

Structure Wakefield Acceleration (SWFA) has been proposed as the backbone for a high-gradient and high-efficiency accelerator for a multi-TeV linear collider [155]. Two separate SWFA schemes, two-beam acceleration (TBA) and collinear wakefield acceleration (CWA) are under consideration. This contribution will explore the application of the relatively mature SWFA schemes (both in the TBA and CWA implementations) as a possible upgrade path to the ILC. The ILC beam format (a train of 3.2 nC single-bunch with an O(MHz) micropulse repetition rate) is comparable to the 182-GHz CWA-based XFEL design that is being pursued at Argonne. The challenge for the

CWA based linear collider would be to raise the overall efficiency due to its single pulse nature. Alternatively, the TBA technology currently under development at Argonne is a 26 GHz accelerator based on a high charge drive beam. Therefore, a TBA contribution to the ILC application would explore two avenues: either operating ILC with higher charge or raising the TBA operating frequency to operate at lower drive charge. Critical to both the TBA and CWA approaches would be continued development of the SWFA bunch control R&D program. This program develops the bunch shaping technology critical for the main and drive beams. For example, we will explore the possibility of shaping the ILC 3.2nC Gaussian bunch for the CWA scheme with a transformer ratio of 5 to produce a 5TeV LC in the ILC tunnel at high efficiency. Note that bunch control is critical to both beam-driven wakefield acceleration methods: SWFA and plasma wakefield acceleration (PWFA).

## 15.2 Physics Opportunities at Multi-TeV

[7 pages; corresponding editors: Zhen Liu (zliuphys@umd.edu), James Wells (jwells@umich.edu)]

(This section will review the program of BSM measurements laid out for CLIC [156] and new experiments in this energy region studied at Snowmass.)

## 15.3 Physics Opportunities at Multi-10 TeV

[5 pages; corresponding editors: Nathaniel Craig (ncraig@physics.ucsb.edu), Zhen Liu (zliuphys@umd.edu), Michael Peskin (mpeskin@slac.stanford.edu)]

(This section will review new work to be done for Snowmass on physics at very high energy  $e^+e^-$  and  $\gamma\gamma$  colliders.)





# Chapter 16

# Conclusions

[3 pages; corresponding editor: Michael Peskin (mpeskin@slac.stanford.edu)]

total page count: 186 pages + bibliography

## ACKNOWLEDGEMENTS

We are grateful to ...



# Bibliography

- [1] T. Behnke, J.E. Brau, B. Foster, J. Fuster, M. Harrison, J.M. Paterson et al., eds., *The International Linear Collider Technical Design Report - Volume 1: Executive Summary*, [1306.6327](#).
- [2] H. Baer et al., eds., *The International Linear Collider Technical Design Report - Volume 2: Physics*, [1306.6352](#).
- [3] C. Adolphsen et al., eds., *The International Linear Collider Technical Design Report - Volume 3.I: Accelerator  $\mathcal{E}$  in the Technical Design Phase*, [1306.6353](#).
- [4] C. Adolphsen et al., eds., *The International Linear Collider Technical Design Report - Volume 3.II: Accelerator Baseline Design*, [1306.6328](#).
- [5] H. Abramowicz et al., *The International Linear Collider Technical Design Report - Volume 4: Detectors*, [1306.6329](#).
- [6] P. Bambade et al., *The International Linear Collider: A Global Project*, [1903.01629](#).
- [7] LCC PHYSICS WORKING GROUP collaboration, *Tests of the Standard Model at the International Linear Collider*, [1908.11299](#).
- [8] K. Fujii et al., *ILC Study Questions for Snowmass 2021*, [2007.03650](#).
- [9] LINEAR COLLIDER COLLABORATION collaboration, *The International Linear Collider Machine Staging Report 2017*, [1711.00568](#).
- [10] M. Harrison, M. Ross and N. Walker, *Luminosity Upgrades for ILC*, [1308.3726](#).
- [11] JAHEP SUBCOMMITTEE ON FUTURE PROJECTS OF HIGH ENERGY PHYSICS collaboration, S. Asai et al., “The final report of the subcommittee on future projects of high energy physics.” [http://www.jahep.org/office/doc/201202\\_hecsubc\\_report.pdf](http://www.jahep.org/office/doc/201202_hecsubc_report.pdf), 2012.
- [12] Japan Association of High Energy Physicists (JAHEP), “A proposal for a phased execution of the international linear collider project.” [http://www.jahep.org/office/doc/201210\\_ILC\\_staging\\_e.pdf](http://www.jahep.org/office/doc/201210_ILC_staging_e.pdf), 2012.
- [13] T. Sanuki, “Overview of the topography and geology of the Kitakami site for the ILC.” Presentation at DESY, Feb. 14, 2017, 2017.

- [14] R.D. Heuer et al., “Parameters for the linear collider.” <https://icfa.fnal.gov/wp-content/uploads/para-Nov20-final.pdf>, 2006.
- [15] M. Dugan, G. and Harrison, B. List and N. Walker, “Implications of an energy-phased approach to the realization of the ILC.” <http://edmsdirect.desy.de/item/D00000001046475>, 2014.
- [16] G. White, “Change request ILC-CR-0002: Baseline optics to provide for a single  $L^*$ .” <http://edmsdirect.desy.de/item/D00000001119175>, 2014.
- [17] K. Buesser, “Change request ILC-CR-0003: Detector hall with vertical shaft access.” <http://edmsdirect.desy.de/item/D00000001084745>, 2014.
- [18] E. Paterson, V. Kuchler, N. Solyak and T. Sanami, “Change request ILC-CR-0012: Reduction of width of linac shield wall and tunnel cross-section.” <http://edmsdirect.desy.de/item/D00000001127835>, 2015.
- [19] K. Yokoya, B. List and E. Paterson, “Change request ILC-CR-0013: Update of the ILC beam dump specifications.” <http://edmsdirect.desy.de/item/D00000001145035>, 2016.
- [20] K. Yokoya, “Change request ILC-CR-0016: Luminosity improvement at 250 GeV.” <http://edmsdirect.desy.de/item/D00000001159725>, 2017.
- [21] Positron Working Group, “Report on the ILC positron source.” <http://edmsdirect.desy.de/item/D00000001165115>, 2018.
- [22] International Committee for Future Accelerators (ICFA), “ICFA statement on the ILC operating at 250 GeV as a Higgs boson factory.” <https://icfa.fnal.gov/wp-content/uploads/ICFA-Statement-Nov2017.pdf>, 2017.
- [23] “TESLA Technology Collaboration.” <http://tesla-new.desy.de/>.
- [24] S. Schreiber and B. Faatz, *The free-electron laser flash*, *High Power Laser Science and Engineering* **3** (2015) E20.
- [25] M. Vogt et al., *Status of the Superconducting Soft X-Ray Free-Electron Laser FLASH at DESY*, in *Proceedings, 9th International Particle Accelerator Conference (IPAC 2018), Vancouver, BC, Apr 29–May 4, 2018*, pp. 1481–1484 (TUPMF090), 2018, DOI.
- [26] “European XFEL.” <https://www.xfel.eu/>.
- [27] “LCLS-II: A world-class discovery machine.” <https://lcls.slac.stanford.edu/lcls-ii>.
- [28] Z. Zhao, D. Wang, Z.-H. Yang and L. Yin, *SCLF: An 8-GeV CW SCRF Linac-Based X-Ray FEL Facility in Shanghai*, in *Proceedings, 38th International Free Electron Laser Conference, FEL2017*, pp. 182–184 (MOP055), 2018, DOI.
- [29] R.-L. Geng et al., *New Results of Development on High Efficiency High Gradient Superconducting RF Cavities*, in *Proceedings, 6th International Particle Accelerator Conference (IPAC 2015): Richmond, VA, May 3–8, 2015*, p. WEPWI013, 2015, DOI.

- [30] C. Adolphsen, “Optimum ML cavity performance: gradient, Q0, and other ML parameters.” Presentation at 2011 Linear Collider Workshop of the Americas (ALCPG11), Eugene, OR, Mar 19–23, 2011, <https://agenda.linearcollider.org/event/4572/>, 2011.
- [31] G. Eremeev, R. Geng, H. Padamsee and V. Shemelin, *High Gradient Studies for ILC with Single Cell Re entrant Shape and Elliptical Shape Cavities made of Fine grain and Large grain Niobium*, *Conf. Proc. C* **070625** (2007) 2337.
- [32] H. Padamsee, J. Knobloch and T. Hays, *RF superconductivity for accelerators*, Wiley, 2nd ed. (2008).
- [33] A. Grassellino et al., *Accelerating fields up to 49 MV/m in TESLA-shape superconducting RF niobium cavities via 75C vacuum bake*, **1806.09824**.
- [34] A. Gurevich, *Theory of RF superconductivity for resonant cavities*, *Supercond. Sci. Technol.* **30** (2017) 034004.
- [35] T. Kubo, *The Next SRF Technologies*, **1703.05645**.
- [36] W. Singer et al., *Production of superconducting 1.3-GHz cavities for the European X-ray Free Electron Laser*, *Phys. Rev. Accel. Beams* **19** (2016) 092001.
- [37] D. Reschke et al., *Performance in the vertical test of the 832 nine-cell 1.3 GHz cavities for the European X-ray Free Electron Laser*, *Phys. Rev. Accel. Beams* **20** (2017) 042004.
- [38] N.J. Walker and D. Kostin, “The European XFEL – experience and lessons learned.” Presentation, International Workshop on Future Linear Colliders (LCWS2017), Strasbourg, France, Oct 22–27, 2017, <https://agenda.linearcollider.org/event/7645/>, 2017.
- [39] W. Kaabi et al., *Power couplers for XFEL*, in *Proceedings, 4th International Particle Accelerator Conference (IPAC 2013), Shanghai, China, May 12-17, 2013*, pp. 2310–2312 (WEPWO001), 2013, <http://JACoW.org/IPAC2013/papers/wepwo001.pdf>.
- [40] S. Sierra et al., *Status and lesson learned from manufacturing of FPC couplers for the XFEL program*, in *Proceedings, 28th International Linear Accelerator Conference (LINAC16), East Lansing, MI, Sep 25-30, 2016*, pp. 572–574 (TUPLR048), 2017, DOI.
- [41] D. Reschke, W. Decking, N. Walker and H. Weise, *The commissioning of the European XFEL Linac and its performance*, in *Proceedings, 18th International Conference on RF Superconductivity (SRF2017): Lanzhou, China, Jul 17-21, 2017*, pp. 1–5 (MOXA02), 2018, DOI.
- [42] S. Berry and O. Napoly, *Assembly of XFEL cryomodules: lessons and results*, in *Proceedings, 28th International Linear Accelerator Conference (LINAC16): East Lansing, Michigan, September 25-30, 2016*, pp. 646–650 (WE1A02), 2017, DOI.
- [43] T.J. Peterson et al., *A Survey of Pressure Vessel Code Compliance for Superconducting RF Cryomodules*, *AIP Conf. Proc.* **1434** (2011) 1575 [1209.2405].

- [44] H. Weise, *How To Produce 100 Superconducting Modules for the European XFEL in Collaboration and with Industry*, in *Proceedings, 5th International Particle Accelerator Conference (IPAC 2014): Dresden, Germany, Jun 15–20, 2014*, pp. 1923–1928 (WEIB03), 2014, DOI.
- [45] D. Kostin, W.-D. Moeller, A. Goessel and K. Jensch, *Superconducting accelerating module tests at DESY*, in *Proceedings, 14th International Conference on RF Superconductivity (SRF2009), Berlin, Sep 20–25, 2009*, pp. 180–184 (TUPPO005), 2009, <http://accelconf.web.cern.ch/AccelConf/SRF2009/papers/TUPPO005.PDF>.
- [46] D. Broemmelsiek et al., *Record High-Gradient SRF Beam Acceleration at Fermilab*, *New J. Phys.* **20** (2018) 113018 [1808.03208].
- [47] Y. Yamamoto et al., *Achievement of Stable Pulsed Operation at 36 MV/m in STF-2 Cryomodule at KEK*, in *Proceedings, 18th International Conference on RF Superconductivity (SRF2017), Lanzhou, China, Jul 17–21, 2017*, pp. 722–728 (THYA02), 2018, DOI.
- [48] K. Kasprzak et al., *Test Results of the European XFEL Serial-production Accelerator Modules*, in *Proceedings, 18th International Conference on RF Superconductivity (SRF2017), Lanzhou, China, July 17-21, 2017*, pp. 312–316 (MOPB106), 2018, DOI.
- [49] S1Global collaboration, “S1Global report.” <http://edmsdirect.desy.de/item/D00000001005135>, 2012.
- [50] M.A. Kemp et al., *Final design of the SLAC P2 Marx klystron modulator*, in *Proceedings, 18th IEEE International Pulsed Power Conference (PPC11), Chicago, IL, Jun 19-23, 2011*, pp. 1582–1589, 2011, DOI.
- [51] M.P.J. Gaudreau, N. Silverman, B. Simpson and J. Casey, *ILC-class Marx modulator at KEK*, in *Proceedings, 5th International Particle Accelerator Conference (IPAC 2014), Dresden, Germany, Jun 15-20, 2014*, pp. 562–563 (MOPME082), 2014, <http://jacow.org/IPAC2014/papers/mopme082.pdf>.
- [52] I. Syratchev, “Introduction to the High Efficiency International Klystron Activity HEIKA.” Presentation, CLIC workshop 2015, Geneva, Switzerland, Jan 26–30, 2015, <https://indico.cern.ch/event/336335/>, 2015.
- [53] F. Gerigk, *Status and future strategy for advanced high power microwave sources for accelerators*, in *Proceedings, 9th International Particle Accelerator Conference (IPAC 2018), Vancouver, BC, Canada, Apr 29–May 4, 2018*, pp. 12–17 (MOYGB1), 2018, DOI.
- [54] I.A. Guzilov, *Bac method of increasing the efficiency in klystrons*, in *Proceedings, 10th International Vacuum Electron Sources Conference (IVESC), Jun 30–Jul 4, 2014*, p. 6891996, 2013, DOI.
- [55] D. Constable et al., *High efficiency klystron development for particle accelerators*, in *Proceedings, 58th ICFA Advanced Beam Dynamics Workshop on High Luminosity Circular  $e^+e^-$  Colliders (eeFACT2016), Daresbury, UK, Oct 24–27, 2016*, pp. 185–187 (WET3AH2), 2017, DOI.

- [56] A.Y. Baikov, C. Marrelli and I. Syratchev, *Toward high-power klystrons with RF power conversion efficiency on the order of 90 %*, *IEEE Trans. Electron. Dev.* **62** (2015) 3406.
- [57] E. Jensen, “Recent developments towards very high efficiency klystrons.” Presentation, 9th CW and high average RF power workshop, Grenoble, France, Jun 20–24, 2016, <https://indico.cern.ch/event/472685/>, 2016.
- [58] H. Nakai, “Change request ILC-CR-0014: Cryogenic layout.” <http://edmsdirect.desy.de/item/D00000001146525>, 2016.
- [59] R. Alley et al., *The Stanford Linear Accelerator polarized electron source*, *Nucl. Instrum. Meth.* **A365** (1995) 1.
- [60] G. Alexander et al., *Undulator-based production of polarized positrons*, *Nucl. Instrum. Meth.* **A610** (2009) 451 [0905.3066].
- [61] K. Moffeit et al., “Spin rotation schemes at the ILC for two interaction regions and positron polarization with both helicities.” SLAC-TN-05-045, 2005.
- [62] L.I. Malysheva et al., *Design of Pre-Dumping Ring Spin Rotator with a Possibility of Helicity Switching for Polarized Positrons at the ILC*, **1602.09050**.
- [63] M.G. Billing et al., *Status of Low Emittance Tuning at CesrTA*, in *Proceedings, 24th Particle accelerator Conference (PAC’11), New York, NY, Mar 28–Apr 1, 2011*, pp. 1540–1542 (WEP022), 2011, <http://accelconf.web.cern.ch/AccelConf/PAC2011/papers/WEP022.PDF>.
- [64] J.V. Conway, Y. Li and M.A. Palmer, *The conceptual design of a vacuum system for the ilc damping rings incorporating electron cloud mitigation techniques*, in *Proceedings, 3rd International Conference on Particle accelerator (IPAC 2012), New Orleans, LA, May 2-25, 2012*, pp. 1960–1962 (TUPPR062), 2012, <http://accelconf.web.cern.ch/AccelConf/IPAC2012/papers/TUPPR062.PDF>.
- [65] T. Naito et al., *Multi-bunch beam extraction using strip-line kicker at KEK-ATF*, in *Proceedings, 1st International Particle Accelerator Conference (IPAC’10), Kyoto, Japan, May 23–28, 2010*, pp. 2386–2388 (WEOBMH02), 2010, <http://accelconf.web.cern.ch/AccelConf/IPAC10/papers/weobmh02.pdf>.
- [66] P. Emma, T. Raubenheimer and F. Zimmermann, *A bunch compressor for the next linear collider*, in *Proceedings, 16th Particle Accelerator Conference and International Conference on High-Energy Accelerators, (HEACC 1995), Dallas, TX, May 1-5, 1995*, pp. 704–706 (RPC03), 1996, <http://accelconf.web.cern.ch/AccelConf/p95/ARTICLES/RPC/RPC03.PDF>.
- [67] N. Walker, “Change request ILC-CR-0010: Proposal to include bunch compressor sections into main linac accelerator system.” <http://edmsdirect.desy.de/item/D00000001119175>, 2015.
- [68] P. Raimondi and A. Seryi, *A Novel final focus design for future linear colliders*, *Phys. Rev. Lett.* **86** (2001) 3779.

- [69] ATF2 collaboration, B.I. Grishanov et al., “ATF2 Proposal.” SLAC-R-771, CERN-AB-2005-035, DESY-05-148, KEK-REPORT-2005-2, 2005.
- [70] B.I. Grishanov et al., *ATF2 proposal, Vol. 2*, [physics/0606194](#).
- [71] T. Okugi, *Achievement of small beam size at ATF2 beamline*, in *Proceedings, 28th International Linear Accelerator Conference (LINAC16), East Lansing, MI, Sep 25-30, 2016*, pp. 27–31 (MO3A02), 2017, [DOI](#).
- [72] ATF2 collaboration, *Experimental validation of a novel compact focusing scheme for future energy-frontier linear lepton colliders*, *Phys. Rev. Lett.* **112** (2014) 034802.
- [73] R.J. Apsimon et al., *Design and operation of a prototype interaction point beam collision feedback system for the International Linear Collider*, *Phys. Rev. Accel. Beams* **21** (2018) 122802 [[1812.08432](#)].
- [74] R. Ramjiawan et al., *Development of a Low-Latency, High-Precision, Beam-Based Feedback System Based on Cavity BPMs at the KEK ATF2*, in *Proceedings, 9th International Particle Accelerator Conference (IPAC 2018): Vancouver, BC, Ap 29–May 4, 2018*, pp. 2212–2215 (WEPAL025), 2018, [DOI](#).
- [75] A. Latina and A. Faus-Golfe, “ATF2.” Input paper for European Strategy for Particle Physics Update, 2018.
- [76] D.R. Walz, L.R. Lucas, H.A. Weidner, R.J. Vetterlein and E.J. Seppi, *Beam Dumps, Energy Slits and Collimators at SLAC - - Their Final Versions and First Performance Data*, *IEEE Trans. Nucl. Sci.* **14** (1967) 923.
- [77] S. Boogert et al., *Polarimeters and Energy Spectrometers for the ILC Beam Delivery System*, *JINST* **4** (2009) P10015 [[0904.0122](#)].
- [78] B. Vormwald, J. List and A. Vauth, *A calibration system for Compton polarimetry at  $e^+e^-$  linear colliders*, *JINST* **11** (2016) P01014 [[1509.03178](#)].
- [79] T. Sanuki, “Tunnel floor vibration issues.” Presentation, Asian Linear Collider Workshop (ALCW2018), Fukuoka, Japan, May 28–Jun 2, 2018. <https://agenda.linearcollider.org/event/7826/>, 2018.
- [80] M. Harrison, M. Ross and N. Walker, *Luminosity Upgrades for ILC*, in *Community Summer Study 2013: Snowmass on the Mississippi*, 8, 2013 [[1308.3726](#)].
- [81] ILC Strategy Council, “Announcement of the results of the ILC candidate site evaluation in Japan.” Press release 28.8.2014, <http://ilc-str.jp/topics/2013/08281826/>, 2014.
- [82] B. Warmbein, “The road to Kitakami.” ILC Newsline Feb. 20, 2014, <http://newsline.linearcollider.org/2014/02/20/the-road-to-kitakami/>, 2014.
- [83] T. Sanuki, “New developments at the Kitakami site.” Presentation at Linear Collider Workshop 2015 (LCWS15), Whistler, BC, Canada, Nov 1–7, 2015, <https://agenda.linearcollider.org/event/6662/>, 2015.



- [84] T. Sanuki and I. Sekine, “Seismic base isolation for detectors and accelerator.” Presentation at International Workshop on Future Linear Colliders, LCWS2018, Arlington, TX, Oct 22-26, 2018, <https://agenda.linearcollider.org/event/7889/>, 2018.
- [85] T. Sanuki, “Tunnel floor vibration issue.” Presentation at Asian Linear Collider Workshop (ALCW 2018), Fukuoka, Japan, May 28–Jun 2, 2018, <https://agenda.linearcollider.org/event/7826/>, 2018.
- [86] OECD, “Prices and purchasing power parities (PPP).” <http://www.oecd.org/sdd/prices-ppp/>, 2018.
- [87] Eurostat, *Eurostat-OECD methodological manual on Purchasing Power Parities*, Luxembourg: Publications Office of the European Union, 2012 ed. (2012).
- [88] ILC Advisory Panel, “Summary of the ILC advisory panel’s discussions to date after revision.” Report, Jul 4, 2018, [http://www.mext.go.jp/component/b\\_menu/shingi/toushin/\\_icsFiles/afieldfile/2018/09/20/1409220\\_2\\_1.pdf](http://www.mext.go.jp/component/b_menu/shingi/toushin/_icsFiles/afieldfile/2018/09/20/1409220_2_1.pdf), 2018.
- [89] A. Yamamoto in *ESPP Symposium 2019*, 2019.
- [90] M. Pekeler, *Superconducting RF Cavity System Production for Particle Accelerators in Scientific and Industrial Applications*, in *Proceedings of ICHEP 2016*, 2016.
- [91] W. Singer et al., *Development of large grain cavities*, *Phys. Rev. ST Accel. Beams* **16** (2013) 012003.
- [92] A. Grassellino, *N Doping: Progress in Development and Understanding*, in *17th International Conference on RF Superconductivity*, p. MOBA06, 2015, DOI.
- [93] A. Romanenko and C. Edwardson, *The effect of vacancies on the microwave surface resistance of niobium revealed by positron annihilation spectroscopy*, *Appl. Phys. Lett.* **102** (2013) 232601.
- [94] S. Posen, A. Romanenko, A. Grassellino, O. Melnychuk and D. Sergatskov, *Ultralow Surface Resistance via Vacuum Heat Treatment of Superconducting Radio-Frequency Cavities*, *Phys. Rev. Applied* **13** (2020) 014024 [1907.00147].
- [95] e. He, F., *Medium-temperature furnace bake of Superconducting Radio-Frequency cavities at IHEP*, 2012.04817.
- [96] A. Grassellino et al., *Unprecedented quality factors at accelerating gradients up to 45 MV/m in niobium superconducting resonators via low temperature nitrogen infusion*, *Supercond. Sci. Technol.* **30** (2017) 094004 [1701.06077].
- [97] P. Dhakal, *Nitrogen Doping and Infusion in SRF Cavities: A Review*, *Phys. Open* **5** (2020) 100034 [2005.03149].
- [98] K. Umemori, E. Kako, T. Konomi, S. Michizono, T. Okada, H. Sakai et al., *Study on Nitrogen Infusion using KEK New Furnace*, in *19th International Conference on RF Superconductivity (SRF 2019)*, p. MOP027, 2019, DOI.

- [99] M. Wenskat, C. Bate, A. Jeromin, T. Keller, J. Knobloch, F. Kramer et al., *Cavity Cut-out Studies of a 1.3 GHz Single-cell Cavity After a Failed Nitrogen Infusion Process*, in *19th International Conference on RF Superconductivity (SRF 2019)*, p. MOP025, 2019, DOI.
- [100] V. Shemelin and H. Padamsee, *The optimal shape of cells of a superconducting accelerating section*, .
- [101] V. Shemelin, H. Padamsee and R. Geng, *Optimal cells for TESLA accelerating structure*, *Nucl. Instrum. Meth. A* **496** (2003) 1.
- [102] J.e. Sekutowicz, *Low Loss Cavity for the 12 GeV CEBAF Upgrade*, .
- [103] K. Saito, “*Strategy for 50 MV/m*”, .
- [104] Z. Li and C. Adolphsen, *A New SRF Cavity Shape with Minimized Surface Electric and Magnetic Fields for the ILC*, .
- [105] F. Furuta et al., *Experimental comparison at KEK of high gradient performance of different single cell superconducting cavity designs*, *Conf. Proc. C* **060626** (2006) 750.
- [106] R. Geng, A. Seaman, V. Shemelin and H. Padamsee, *World record accelerating gradient achieved in a superconducting niobium RF cavity*, *Conf. Proc. C* **0505161** (2005) 653.
- [107] C.E. Reece and G. Ciovati, *Superconducting Radio-Frequency Technology R & D for Future Accelerator Applications*, *Rev. Accel. Sci. Tech.* **5** (2012) 285 [1208.1978].
- [108] R.L.e. Geng, *LSF Shape Cavity Development: Recent Results and Future Plan*, in *LCWS 2018*, 2018.
- [109] T. Peterson and J. Weisend II, *TESLA & ILC Cryomodules*, in *Cryostat Design*, pp. 117–145 (2016), DOI.
- [110] A. Avrakhov, P. Kanareykin and N. Solyak, *Traveling wave accelerating structure for a superconducting accelerator*, *Conf. Proc. C* **0505161** (2005) 4296.
- [111] R. Kostin, P. Avrakhov, A. Kanareykin, N. Solyak, V. Yakovlev, S. Kazakov et al., *A high gradient test of a single-cell superconducting radio frequency cavity with a feedback waveguide*, *Supercond. Sci. Technol.* **28** (2015) 095007.
- [112] V. Shemelin *PRSTAB*, to be submitted (2021) .
- [113] S. Posen and D. Hall, *Nb<sub>3</sub>Sn superconducting radiofrequency cavities: fabrication, results, properties, and prospects*, *Supercond. Sci. Technol.* **30** (2017) 033004.
- [114] S. Posen, J. Lee, O. Melnychuk, Y. Pischalnikov, D. Seidman, D. Sergatskov et al., *Nb<sub>3</sub>Sn at Fermilab: Exploring Performance*, in *19th International Conference on RF Superconductivity (SRF 2019)*, p. THFUB1, 2019, DOI.
- [115] S. Posen in *TTC2019*, 2019.
- [116] e. Godeke, *A. Supercond. Sci. Technol.* **19** (2006) R68.

- [117] e. Becker, *C. Appl. Phys. Lett.* **106** (2015) 082602.
- [118] R. Hori.
- [119] F. Furuta, D. Bice, A.C. Crawford and T. Ring, *Fermilab EP Facility Improvement*, in *19th International Conference on RF Superconductivity (SRF 2019)*, pp. 453–455, 2019, DOI.
- [120] Y. Pischalnikov, B. Hartman, J. Holzbauer, W. Schappert, S. Smith and J.-C. Yun, *Reliability of the LCLS II SRF Cavity Tuner*, in *17th International Conference on RF Superconductivity*, p. THPB065, 2015, DOI.
- [121] V. Kashikhin, S. Cheban, J. DiMarco, E. Harms, A. Makarov, T. Strauss et al., *Superconducting Magnet Performance in LCLS-II Cryomodules*, in *9th International Particle Accelerator Conference*, p. WEPML009, 2018, DOI.
- [122] M. Doleans, *Ignition and monitoring technique for plasma processing of multicell superconducting radio-frequency cavities*, *J. Appl. Phys.* **120** (2016) 243301.
- [123] P. Berrutti, B. Giaccone, M. Martinello, A. Grassellino, T. Khabiboulline, M. Doleans et al., *Plasma ignition and detection for in-situ cleaning of 1.3 GHz 9-cell cavities*, *J. Appl. Phys.* **126** (2019) 023302 [1902.03172].
- [124] S. Posen, J. Lee, D. Seidman, A. Romanenko, B. Tennis, O. Melnychuk et al., *Advances in Nb<sub>3</sub>Sn superconducting radiofrequency cavities towards first practical accelerator applications*, 2008.00599.
- [125] N. Sinev, J. Brau, D. Strom, C. Baltay, W. Emmet and D. Rabinowitz, *Chronopixel project status*, *PoS VERTEX2015* (2015) 038.
- [126] J. Brau et al., *KPiX - A 1,024 Channel Readout ASIC for the ILC*, in *2012 IEEE Nuclear Science Symposium and Medical Imaging Conference and 19th Workshop on Room-Temperature Semiconductor X-ray and Gamma-ray Detectors*, pp. 1857–1860, 2012, DOI.
- [127] A. Steinhebel and J. Brau, *Studies of the Response of the SiD Silicon-Tungsten ECal*, in *International Workshop on Future Linear Colliders*, 3, 2017 [1703.08605].
- [128] B. Parker, A. Mikhailichenko, K. Buesser, J. Hauptman, T. Tauchi, P. Burrows et al., *Functional Requirements on the Design of the Detectors and the Interaction Region of an e<sup>+</sup>e<sup>-</sup> Linear Collider with a Push-Pull Arrangement of Detectors*, in *Particle Accelerator Conference (PAC 09)*, p. WE6PFP078, 2010.
- [129] K. Buesser, *ILD Machine-Detector Interface and Experimental Hall Issues*, in *International Workshop on Future Linear Colliders (LCWS11)*, 1, 2012 [1201.5807].
- [130] D. Curtin et al., *Exotic decays of the 125 GeV Higgs boson*, *Phys. Rev. D* **90** (2014) 075004 [1312.4992].
- [131] Z. Liu, L.-T. Wang and H. Zhang, *Exotic decays of the 125 GeV Higgs boson at future e<sup>+</sup>e<sup>-</sup> lepton colliders*, *Chin. Phys. C* **41** (2017) 063102 [1612.09284].

- [132] M. Carena, Z. Liu and Y. Wang, *Electroweak phase transition with spontaneous  $Z_2$ -breaking*, *JHEP* **08** (2020) 107 [[1911.10206](#)].
- [133] M.J. Ramsey-Musolf, *The electroweak phase transition: a collider target*, *JHEP* **09** (2020) 179 [[1912.07189](#)].
- [134] S. Alipour-Fard, N. Craig, S. Gori, S. Koren and D. Redigolo, *The second Higgs at the lifetime frontier*, *JHEP* **07** (2020) 029 [[1812.09315](#)].
- [135] Z. Chacko, P.J. Fox, R. Harnik and Z. Liu, *Neutrino Masses from Low Scale Partial Compositeness*, [2012.01443](#).
- [136] N. Craig, A. Katz, M. Strassler and R. Sundrum, *Naturalness in the Dark at the LHC*, *JHEP* **07** (2015) 105 [[1501.05310](#)].
- [137] D. Curtin and C.B. Verhaaren, *Discovering Uncolored Naturalness in Exotic Higgs Decays*, *JHEP* **12** (2015) 072 [[1506.06141](#)].
- [138] J. Liu, Z. Liu and L.-T. Wang, *Enhancing Long-Lived Particles Searches at the LHC with Precision Timing Information*, *Phys. Rev. Lett.* **122** (2019) 131801 [[1805.05957](#)].
- [139] J. Liu, Z. Liu, L.-T. Wang and X.-P. Wang, *Enhancing Sensitivities to Long-lived Particles with High Granularity Calorimeters at the LHC*, *JHEP* **11** (2020) 066 [[2005.10836](#)].
- [140] N. Arkani-Hamed, T. Cohen, R.T. D'Agnolo, A. Hook, H.D. Kim and D. Pinner, *Solving the Hierarchy Problem at Reheating with a Large Number of Degrees of Freedom*, *Phys. Rev. Lett.* **117** (2016) 251801 [[1607.06821](#)].
- [141] N. Arkani-Hamed, R. Tito D'agnolo and H.D. Kim, *The Weak Scale as a Trigger*, [2012.04652](#).
- [142] P. Meade and H. Ramani, *Unrestored Electroweak Symmetry*, *Phys. Rev. Lett.* **122** (2019) 041802 [[1807.07578](#)].
- [143] I. Baldes and G. Servant, *High scale electroweak phase transition: baryogenesis &  $\mathcal{E}$  symmetry non-restoration*, *JHEP* **10** (2018) 053 [[1807.08770](#)].
- [144] A. Glioti, R. Rattazzi and L. Vecchi, *Electroweak Baryogenesis above the Electroweak Scale*, *JHEP* **04** (2019) 027 [[1811.11740](#)].
- [145] O. Matsedonskyi and G. Servant, *High-Temperature Electroweak Symmetry Non-Restoration from New Fermions and Implications for Baryogenesis*, *JHEP* **09** (2020) 012 [[2002.05174](#)].
- [146] H. Chen, M.-X. Luo, I. Moulton, T.-Z. Yang, X. Zhang and H.X. Zhu, *Three point energy correlators in the collinear limit: symmetries, dualities and analytic results*, *JHEP* **08** (2020) 028 [[1912.11050](#)].
- [147] H. Chen, I. Moulton, X. Zhang and H.X. Zhu, *Rethinking jets with energy correlators: Tracks, resummation, and analytic continuation*, *Phys. Rev. D* **102** (2020) 054012 [[2004.11381](#)].

- [148] A. Freitas et al., *Theoretical uncertainties for electroweak and Higgs-boson precision measurements at FCC-ee*, [1906.05379](#).
- [149] S. Jadach and M. Skrzypek, *QED challenges at FCC-ee precision measurements*, *Eur. Phys. J. C* **79** (2019) 756 [[1903.09895](#)].
- [150] J. Ablinger, J. Blümlein, A. De Freitas and K. Schönwald, *Subleading Logarithmic QED Initial State Corrections to  $e^+e^- \rightarrow \gamma^*/Z^{0*}$  to  $O(\alpha^6 L^5)$* , *Nucl. Phys. B* **955** (2020) 115045 [[2004.04287](#)].
- [151] E. Esarey, C.B. Schroeder and W.P. Leemans, *Physics of laser-driven plasma-based electron accelerators*, *Rev. Mod. Phys.* **81** (2009) 1229.
- [152] C.B. Schroeder, E. Esarey, C.G.R. Geddes, C. Benedetti and W.P. Leemans, *Physics considerations for laser-plasma linear colliders*, *Phys. Rev. ST Accel. Beams* **13** (2010) 101301.
- [153] C.B. Schroeder, C. Benedetti, E. Esarey and W.P. Leemans, *Laser-plasma-based linear collider using hollow plasma channels*, *Nucl. Instrum. Meth. A* **829** (2016) 113.
- [154] W. Leemans, ed., *Report of the Workshop on Laser Technology for k-BELLA and Beyond*, .
- [155] W. Gai, J.G. Power and C. Jing, *Short-pulse dielectric two-beam acceleration*, *J. Plasma Phys.* **78** (2012) 339.
- [156] R. Franceschini et al., *The CLIC Potential for New Physics*, [1812.02093](#).